Kinematic Analysis and Synthesis of Kinematically Redundant Hybrid Parallel Robots

Thèse

Kefei Wen

Doctorat en génie mécanique
Philosophiæ doctor (Ph. D.)

Québec, Canada

Résumé

L'architecture mécanique, l'actionnement, la détection directe ou indirecte des efforts ainsi que la conception de contrôleurs en impédance ou en admittance sont les aspects fondamentaux et importants à considérer pour le développement d'un robot permettant une interaction physique humain-robot (IPHR) sécuritaire. Cette thèse est consacrée au développement de nouvelles architectures de robots pour l'IPHR qui ont une structure simple, peu ou pas de singularités, qui sont légers et à faible impédance mécanique.

Un nouveau robot parallèle hybride cinématiquement redondant (RPHCR) sans singularité dans l'espace de travail et ayant une faible inertie mobile est d'abord proposé. Le concept de la redondance cinématique des membrures et l'agencement d'assemblage de la plate-forme mobile de ce robot sont ensuite généralisés et développés en une méthodologie pour la synthèse de nouveaux RPHCRs. Plusieurs exemples d'architectures sont présentés et une solution analytique du problème géométrique inverse est obtenue.

Le problème géométrique direct des RPHCRs doit être résolu afin de déterminer la position et l'orientation de la plate-forme mobile pour des coordonnées articulaires données. Différentes approches pour résoudre le problème géométrique direct sont alors proposées. Il est montré que le problème géométrique direct des RPHCRs proposés dans la thèse est beaucoup plus simple que celui associé aux robots non redondants ou à de nombreux autres robots parallèles cinématiquement redondants. L'agrandissement de l'espace de travail et l'optimisation des trajectoires articulaires des RPHCRs sont réalisés en déterminant les valeurs optimales des coordonnées redondantes.

Enfin, la redondance est en outre utilisée pour opérer un préhenseur monté sur la plateforme mobile à partir des actionneurs fixés à la base du robot ou près de celle-ci. Un contrôleur combiné en position et force de préhension est proposé pour le contrôle de la force de préhension.

Abstract

Robot architecture, actuation, indirect/direct force sensing, and impedance/admittance controller design are the fundamental and important aspects to be considered in order to achieve safe physical human-robot interaction (pHRI). This thesis is devoted to the development of novel robot architectures for pHRI that have a simple structure, few or no singularities, lightweight, and low-impedance.

A novel kinematically redundant hybrid parallel robot (KRHPR) that is singularity-free throughout the workspace and has low moving inertia is firstly proposed. The concept of the redundant links and moving platform assembly arrangement of this robot is further generalised and developed into a methodology for the synthesis of novel KRHPRs. Several example architectures are presented and an analytical inverse kinematic solution is derived.

The forward kinematics of the KRHPRs must be solved to determine the position and orientation of the moving platform for given joint coordinates. Different approaches for solving the forward kinematic problem are then proposed. It is shown that the forward kinematics of the KRHPRs proposed in the thesis is much simpler than that of their non-redundant counterparts or that of many other kinematically redundant parallel robots. Workspace enlargement and joint trajectory optimisation of the KRHPRs are pursued by determining the optimal values of the redundant coordinates.

Finally, the redundancy is further utilised to operate a gripper on the moving platform from the base actuators. A combined position and grasping force controller is proposed for the control of the grasping force.

Contents

List of Figures

Acknowledgements

I am indebted to professor Clément Gosselin, my research supervisor, for his invaluable suggestions, unrelenting support and profound belief in my work. This thesis has benefitted from his extensive knowledge in robotics and constructive criticism.

I also wish to express my appreciation to all my colleagues in the Robotics Laboratory who have extended a great amount of assistance and cooperation. Special thanks to David Harton, graduate student, for drawing the CAD models, to Tan Sy Nguyen, graduate student, for many enriching discussions on control theory, to Simon Foucault and Thierry Laliberté, research associates, for prototyping and creating most of the software to control the robots.

Furthermore, I am very grateful to my wife, Pengxiao Guo, for her understanding and support in my research, and to my daughter, Gabrielle Wen, her birth has greatly encouraged me to complete this work.

Finally, the financial support of the Natural Sciences and Engineering Research Council of Canada (NSERC) and of the Canada Research Chair program is gratefully acknowledged.

List of Publications

A list of publications that arose from this thesis is given as follows:

1. Kefei Wen and Clément Gosselin, "Static model based grasping force control of parallel grasping robots with partial Cartesian force measurement," *IEEE/ASME Transactions on Mechatronics*. Under review.

2. Kefei Wen, Tan Sy Nguyen, David Harton, Thierry Laliberté and Clément Gosselin, "A backdrivable kinematically redundant (6+3)-dof hybrid parallel robot for intuitive sensorless physical human-robot interaction," *IEEE Transactions on Robotics*, 2020. Accepted.

3. Kefei Wen and Clément Gosselin, "Workspace enlargement and joint trajectory optimisation of a (6+3)-dof kinematically redundant hybrid robot," *Parallel 2020: The 4th International Workshop on Fundamental Issues, Applications and Future Research Directions for Parallel Mechanisms / Manipulators / Machines*, 2020.

4. Kefei Wen and Clément Gosselin, "Forward kinematic analysis of kinematically redundant hybrid parallel robots," *ASME Journal of Mechanisms and Robotics*, 12 (6) (2020), 061008.

5. Kefei Wen and Clément Gosselin, "Kinematically redundant hybrid robots with simple singularity conditions and analytical inverse kinematic solutions," *IEEE Robotics and Automation Letters*, 4 (4) (2019), 3828–3835.

6. Kefei Wen, David Harton, Thierry Laliberté and Clément Gosselin, "Kinematically redundant (6+3)-dof hybrid parallel robot with large orientational workspace and remotely operated gripper," Proceedings of the *IEEE International Conference on Robotics and Automation (ICRA)*, 2019.

Introduction

Robots that physically interact with humans are making their way into people's daily lives. It is anticipated that many applications will arise in the future like in manufacturing, in healthcare, in the care for the elderly and in robotics in the home.

One of the key requirements of physical human-robot interaction (pHRI) is to keep the human user safe. To achieve this, the controller of interaction should be designed carefully. In turn, the performance of the controller highly depends on whether the robot's structure is compact (e.g., low inertia) and easy to model. Robots that are currently used as pHRI interfaces are mainly serial manipulators (Loughlin et al., 2007; Ajoudani et al., 2018). However, in most cases, such robots have relatively large inertia due to the moving motors (see Fig. 0.1). In (Rooks, 2006), although some of the motors of the whole arm manipulator (WAM) are mounted in the base and at shoulder height to achieve low inertia, additional cable transmission is required, which leads to mechanical complexity (see Fig. 0.2[1]).

Figure 0.1 – The DLR lightweight robot arm (Loughlin et al., 2007).

[1] http://www.me.unm.edu/~starr/research/WAM_UsersGuide_AE-00.pdf

Figure 0.2 – The WAM arm.

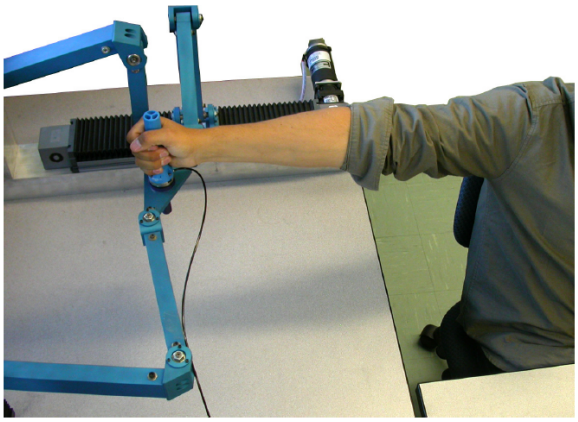

Figure 0.3 – The 3-dof positioning parallel robot for pHRI (Duchaine and Gosselin, 2008).

Many parallel robots are excellent candidates for pHRI applications. The parallel structure, in which the moving platform is connected to the base through several legs, allows to arrange the actuators to the joints on or close to the base, thereby ensuring low inertia of the moving part. For example, a 3-degree-of-freedom (3-dof) positioning parallel robot is implemented in validating a new variable admittance control scheme that guarantees the stability of the robot during pHRI (Duchaine and Gosselin, 2008, 2009) (see Fig. 0.3). A variant of this 3-dof parallel robot is used as the interface of pHRI in a macro-mini system, where the mini high-bandwidth low-impedance passive mechanism (the 3-dof parallel robot) is exploited to effortlessly and intuitively control a low-bandwidth high-impedance active macro gantry manipulator (Badeau et al., 2018) (see Fig. 0.4).

Nevertheless, the above mentioned parallel robots have only three translational degrees of freedom. In many cases, the rotational degrees of freedom are also required to complete

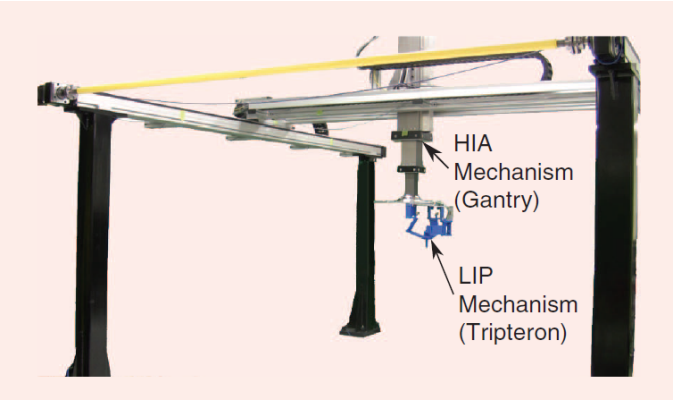

Figure 0.4 – A mini low-impedance passive (LIP) 3-dof positioning parallel robot is mounted on the end-effector of a macro high-impedance active (HIA) gantry manipulator for pHRI (Badeau et al., 2018).

more complex tasks. A possible approach for producing the rotational degrees of freedom is to mount a 3-dof serial wrist with intersecting axes on the moving platform of a 3-dof translational parallel robot (Tobergte et al., 2011) (see Fig. 0.5[2]). But motors far away from the base of the parallel robot are required to drive the serial wrist, thereby increasing the inertia of the moving part. A straightforward way to overcome these problems is to use 6-dof parallel robots. However, the orientational workspace of such robots is limited to relatively small rotations due to the type II (or parallel) singularities (Gosselin and Angeles, 1990). In order to avoid the type II singular configurations, researchers have proposed to use actuation (Saafi et al., 2015) or kinematic redundancy (Wang and Gosselin, 2004; Ebrahimi et al., 2007; Kong et al., 2013; Gosselin et al., 2016; Schreiber and Gosselin, 2018). In this thesis, we are particularly interested in and devoted to developing robots using the latter kind of redundancy, because antagonistic forces could be generated in a redundantly actuated robot.

In Chapter 1, a novel 3-[$\underline{\text{R}}$($\underline{\text{R}}$R-$\underline{\text{R}}$RR)SR] $(6+3)$-dof spatial kinematically redundant hybrid parallel robot (KRHPR) with revolute actuators is proposed for low-impedance pHRI, where $\underline{\text{R}}$ and R denote respectively actuated and passive revolute joints, S denotes a passive spherical joint. Each leg of the KRHPR consists of an actuated 3-dof positioning linkage and a spherical-revolute kinematically redundant link. The kinematic model is developed based on the constraint conditions of the robot. It is shown that the type II singularities can be completely avoided, thereby yielding a very large translational and orientational workspace, which is visualised through the workspace analysis. The proposed analytical inverse kinematic solution is implemented in avoiding the singularities and a workspace analysis is performed. An example is given to demonstrate the excellent rotational ability of the robot, in which a novel Jacobian is developed for the dexterity analysis of the robot.

In Chapter 2, inspired by the structure of the spherical-revolute kinematically redundant

[2] https://forcedimension.com/products/sigma

Figure 0.5 – The sigma.7 haptic device from Force Dimension.

link, we propose two different types of redundant links and three different platform assembly arrangements. Based on this, an approach is developed to synthesize three-legged planar $(3+n)$- and spatial $(6+n)$-dof KRHPRs with very simple — or vanishing — type II singularity conditions. Here n denotes the number of redundancies. Similarly to the 3-[R(RR-RRR)SR] architecture, the inverse kinematic problem of the KRHPRs proposed in this chapter can be solved analytically. Examples of several synthesized KRHPRs are enumerated and the velocity equations of these architectures are derived. Different types of platform arrangements are proposed.

Chapter 3 is devoted to the forward kinematic analysis of the spatial $(6+3)$-dof KRHPRs proposed in Chapter 2. The control of the robot during pHRI requires the solution of the forward kinematic problem using the actuator encoder data as inputs. Seven different approaches of solving the forward kinematic problem of a spatial 3-RRRSR KRHPR with a given platform assembly arrangement based on different numbers of extra encoders are developed. It is revealed that five of these methods can produce a unique solution analytically or numerically. An example is given to validate the feasibility of these approaches. One of the provided approaches is applied to the real-time control of a prototype of the robot. All of the seven approaches can be applied to the others KRHPRs proposed in Chapter 2 with the first platform assembly arrangement, while the forward kinematic problem of the proposed KRHPRs with the other two platform assembly arrangements proposed in Chapter 2 can be solved using five of the seven approaches.

The analytical inverse kinematic solution of the KRHPRs makes it possible to control the redundant coordinates actively, which can be exploited to optimise the workspace and joint trajectory. A case study using the 3-RRRSR $(6+3)$-dof KRHPR is pursued in Chapter 4.

This KRHPR can produce the same workspace as the 3-[R(RR-RRR)SR] architecture if they have equivalent dimensions. Some portions of the translational and orientational workspaces are evaluated, in which the enlargement of the workspace is visualised by comparing to those of the 3-[R(RR-RRR)SR] architecture provided in Chapter 1. An approach is developed to determine the optimal actuated joint and redundant coordinates so that a performance index can be minimised approximately when the robot is following a prescribed Cartesian trajectory.

As an extra benefit of the proposed KRHPRs, the redundancy of the robots can be further exploited to operate a gripper from the base motors, similarly to what was proposed in (Gosselin et al., 2015) for a planar 4-dof kinematically redundant parallel robot with PRR legs, where P denotes a actuated prismatic joint. These robots are also considered to be non-redundant if every redundant dof is taken as an additional Cartesian coordinate. Furthermore, if the object grasped by the robot gripper is rigid, the kinematic redundancy vanishes and the type of redundancy of these robots — in addition to the two types mentioned above — can be regarded as redundantly actuated because the number of actuators is larger than the number of independent Cartesian coordinates. Three different static models of the robots can be established with respect to each of the types of redundancy. The feasibility of these static models for performing grasping force control is analysed in Chapter 5 based on two proposed architectures. It is shown that only one of the static models is reasonable for this purpose, which is verified by an experiment using a combined position and grasping force control scheme.

Finally, conclusion and future research are addressed.

Chapter 1

A Novel Low-Impedance (6+3)-dof Spatial KRHPR for Physical Human-Robot Interaction

1.1 Introduction

Applications of six-degree-of-freedom (6-dof) spatial parallel mechanisms (SPMs) can be found in many areas such as robotics, motion simulators and high-precision positioning devices due to their properties of high payload capability and positioning accuracy. However, the performances of such mechanisms are limited by singularities within their workspace, especially parallel (type II) singularities (Gosselin and Angeles, 1990; Zlatanov et al., 1995, 2002; Conconi and Carricato, 2009).

Numerous research initiatives regarding the singularity analysis of SPMs have been reported (see for instance (St-Onge and Gosselin, 2000; Kong and Gosselin, 2001, 2002; Ebert-Uphoff et al., 2002; Angeles et al., 2003; Yu et al., 2012)). Among other proposed techniques, the use of Grassmann's line geometry (GLG) (Merlet, 1989; Monsarrat and Gosselin, 2001; Tale Masouleh and Gosselin, 2009) and Grassmann-Cayley Algebra (Ben-Horin and Shoham, 2006a,b, 2009; Kanaan et al., 2009; Caro et al., 2010; Amine et al., 2012) are very useful because they provide geometric insight and they do not require the explicit computation of the determinant of the Jacobian matrix. GLG is used in this work.

Although the approaches of singularity analysis mentioned above are helpful for trajectory planning, the workspace of parallel mechanisms is nevertheless limited by such singularities. As a means of alleviating these shortcomings, the use of redundancy was proposed by some researchers. Pierrot (Pierrot, 2002) distinguishes three types of redundancies, namely: kinematic, actuation and measurement redundancy. When the mobility of at least one of the legs is greater than the required dof, the mechanism is said to be kinematically redundant. This

can be used for singularity avoidance and workspace enlargement (Wang and Gosselin, 2004; Kotlarski et al., 2011; Gosselin et al., 2015; Gosselin and Schreiber, 2016). If extra legs are added to the mechanism or if some of the passive joints are actuated, the mechanism is said to be redundantly actuated (Luces et al., 2017). Such type of redundancy may help to avoid singularities and increase stiffness (Zhao and Gao, 2009). However, redundantly actuated mechanisms may also generate internal forces, which lead to control and calibration complexities (Cheng et al., 2003; il Jeong et al., 2004). Measurement redundancy can be achieved by using more sensors than the number of actuated joints and is introduced to improve the accuracy of the mechanism and to simplify the solution of the direct kinematic problem(Marquet et al., 2002). However, it does not help to avoid singularities. It can therefore be argued that kinematic redundancy is a very attractive way to avoid singularities. A detailed analysis of SPMs with several different kinematically redundant legs can be found in (Gosselin and Schreiber, 2018).

Kinematic redundancy has been applied to some recently proposed new architectures (see, for instance, (Gosselin et al., 2015) and (Gosselin and Schreiber, 2016)), where the authors focused on the enlargement of the orientational workspace, which is an important benefit of using kinematic redundancy. In (Gosselin et al., 2015), the kinematic redundancy is achieved by an additional revolute-revolute redundant link connecting a pair of legs to the platform of a 3-dof planar mechanism. With such an arrangement, the robot can avoid all singularities throughout the workspace, which makes it possible to produce an unlimited rotational motion of the platform. In (Gosselin and Schreiber, 2016), some legs of a conventional 6-dof spatial Gough-Stewart platform are replaced by redundant legs consisting of a revolute-spherical redundant link connecting a pair of legs to the platform while preserving the tension-compression loading of the legs. It is shown that by introducing at least three redundant legs, any Cartesian posture of the platform can be reached with a non-singular configuration of the mechanism, thereby the orientational workspace of the composed (6+3)-dof kinematically redundant robot is considerably extended compared to that of the conventional Gough-Stewart platform. In (Schreiber and Gosselin, 2019), the redundancy resolution of the robot proposed in (Gosselin and Schreiber, 2016) is presented. Algorithms are developed in order to resolve the redundancy while avoiding singularities. Although the effectiveness of the numerical algorithms is successfully demonstrated, the singularity avoidance cannot be expressed in closed-form and included as such in the solution of the inverse kinematic problem.

In this chapter, we propose a three-legged revolute joint actuated (6+3)-dof kinematically redundant hybrid parallel robot (KRHPR) that can be regarded as the redundant counterpart of the 3-[R($\underline{\text{R}}$R-$\underline{\text{R}}$RR)S] platform studied in (Monsarrat and Gosselin, 2001) and (Monsarrat and Gosselin, 2003). Using only three legs can help to avoid leg interferences and interferences with the environment, which is an important feature in the context of physical human-robot interaction. The mechanism is driven by nine motors: three per leg. Each of the legs is

then connected to the moving platform via a redundant link. The axes of the revolute joints connecting the redundant links to the platform are parallel. Using this arrangement, it is shown that type II singularities can be completely avoided. Moreover, the singularity analysis — which is readily conducted using GLG — yields very simple conditions. Consequently, a closed-form solution of the inverse kinematics, including the avoidance of singularities, can be obtained without having to resort to numerical algorithms, which greatly simplifies the trajectory planning of the robot.

This chapter is structured as follows. A description of the architecture of the proposed robot is given in Section 1.2, followed by the development of the kinematic model in Section 1.3. Then, GLG is applied in Section 1.4 to analyse the type II singular conditions of the robot. It is shown that type II singularities are easily avoidable without requiring special trajectory planning. Sections 1.5 and 1.6 respectively address the inverse kinematics and the forward kinematics of the robot. Then, in Section 1.7, it is shown that the proposed robot has a very large singularity-exempt rotational and translational range of motion. In Section 1.8, the excellent rotation behaviour of the robot is demonstrated through an example trajectory. Finally, conclusions are drawn in Section 1.9.

1.2 Robot Architecture

The architecture of the proposed robot consists of a moving platform connected to the base by three identical kinematically redundant $\underline{\mathrm{R}}(\underline{\mathrm{R}}\mathrm{R}\text{-}\underline{\mathrm{R}}\mathrm{RR})\mathrm{SR}$ legs. A CAD model of the robot is shown in Fig. 1.1, while a prototype is shown in Fig. 1.2. Here, $\underline{\mathrm{R}}$ stands for an actuated revolute joint, R stands for a passive revolute joint and S stands for a passive spherical joint. In each of the legs, a first actuated revolute joint is mounted at the base. Then, two actuated revolute joints with collinear axes are mounted on the first moving link and are used to actuate two bars of a planar 5-bar linkage (see Fig. 1.3). The combination of these three actuated joints is used to position the spherical joint of the ith leg (point S_i) in space, as illustrated in Fig. 1.3. The spherical joint at point S_i is then connected to a link that is in turn connected to the moving platform using a revolute joint. In the final design, this redundant SR link is replaced by a parallelogram (see Fig. 1.1). A direct drive transmission is exploited to ensure the robot is backdrivable, which makes the physical human-robot interaction (pHRI) effortless and safe.

A description of the geometric parameters used to model the kinematics of the robot is given in Fig. 1.3. In the model, l_{ij}, $(i = 1, 2, 3; j = 1, \ldots, 7)$ denotes the length of the jth link of the ith leg. The axes of all the joints in the planar 5-bar linkage are parallel to each other and perpendicular to the axis of the first joint of the leg. Also, the axis of the revolute joint attached to the platform is perpendicular to the plane of the platform, formed by the three attachment points of the legs. The actuated joints $i2$ and $i3$ at the base of the planar 5-bar

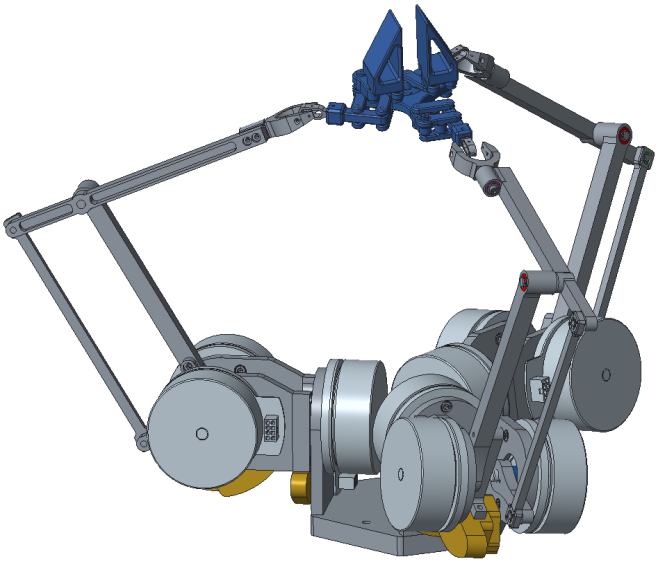

Figure 1.1 – CAD model of the 3-[R(RR-RRR)SR] architecture (Wen et al., 2019).

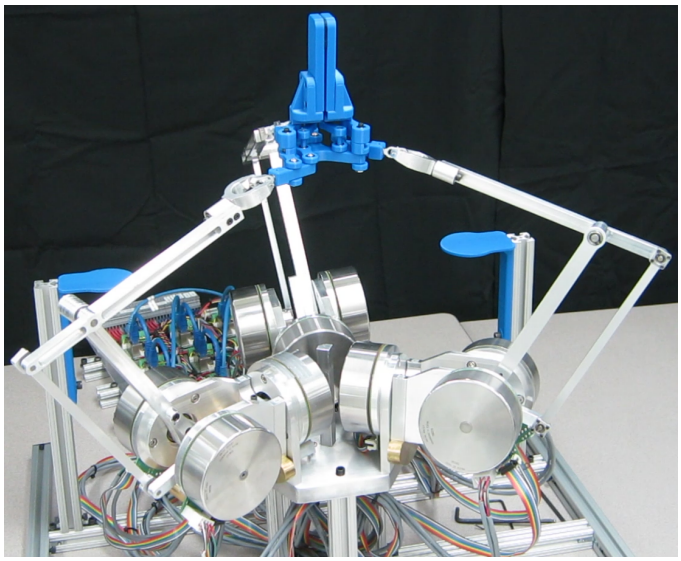

Figure 1.2 – Prototype of the 3-[R(RR-RRR)SR] architecture.

linkage are associated with unit vectors $\mathbf{e}_{i2}$ and $\mathbf{e}_{i3}$. In order to keep away from type I (serial) singularities, which occur when the centre of joint S_i is located on the axis of the first actuated joint of the leg — associated with unit vector $\mathbf{e}_{i1}$ —, links $i1$ are designed to make an obtuse angle with respect to the base which is the angle described as α in Fig. 1.3. In the final design, angle α is selected to be equal to π. This is the optimal selection to prevent type I singularities if the base of the robot is considered as the lower limit of the workspace. Indeed, in this case, the singular configurations are located outside of the workspace of the robot. In order to reduce the effect of the inertia of motors $i2$ and $i3$, they are placed as close as possible to the axis of the first actuator, as illustrated in Fig. 1.3. These motors drive respectively links

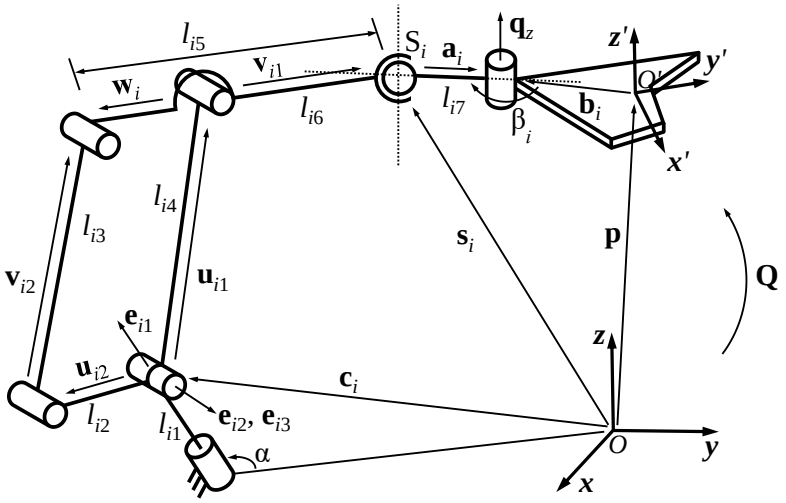

Figure 1.3 – Geometric description of one leg.

$i4$ and $i2$ of the planar 5-bar linkage. As opposed to many other SPMs in which the S joints are directly attached to the platform (for instance in (Monsarrat and Gosselin, 2001)), in the present robot they are located between links $i6$ and $i7$. Such an arrangement, along with the particular direction of the axis of the R joint attached to the platform — which is orthogonal to the plane of the platform — yields advantages for the singularity and inverse kinematic analysis, as shown in the upcoming sections of the chapter. It should also be pointed out that, because of the extra link between the S joints and the platform, the mechanism has 9 degrees of freedom and 9 actuators (3 in each leg) which means that the redundancy is purely kinematic. Therefore, there is no actuation redundancy and no antagonistic forces are generated by the actuators.

1.3 Kinematic Modelling

A base frame and a moving frame are respectively attached to the centroid of the base and moving platforms, which are noted as $Oxyz$ and $O'x'y'z'$ (see Fig. 1.3). Vector $\mathbf{p}$ represents the position of O' with respect to O and matrix $\mathbf{Q}$ represents the orientation of the moving platform with respect to the base. Vector $\mathbf{s}_i$ denotes the position of S_i. Vector $\mathbf{q}_z$ is the unit vector along the axis of the revolute joint attached to the platform and $\mathbf{b}_i$ is the position vector of the centre of the revolute joint that is attached to the platform, which is expressed in the moving frame. Except for $\mathbf{b}_i$, all vectors are expressed in the base frame. The constraint equations of the robot, which are used to derive the kinematics, can be written as follows. Firstly, the constraint on the length of the seventh link is written as

$$(\mathbf{p} + \mathbf{Q}\mathbf{b}_i - \mathbf{s}_i)^T (\mathbf{p} + \mathbf{Q}\mathbf{b}_i - \mathbf{s}_i) = l_{i7}^2, \qquad i = 1, 2, 3. \tag{1.1}$$

Also, the seventh link must be orthogonal to the axis of the R joint attached to the platform, which yields,

$$\mathbf{q}_z^T \left(\mathbf{p} + \mathbf{Q}\mathbf{b}_i - \mathbf{s}_i\right) = 0. \tag{1.2}$$

Equations (1.1) and (1.2) are the geometric constraints of the robot. Equation (1.1) is first considered. The time derivative of (1.1) yields

$$\mathbf{a}_i^T \dot{\mathbf{p}} + \mathbf{a}_i^T \dot{\mathbf{Q}}\mathbf{b}_i = \mathbf{a}_i^T \dot{\mathbf{s}}_i \tag{1.3}$$

where

$$\mathbf{a}_i = \mathbf{p} + \mathbf{Q}\mathbf{b}_i - \mathbf{s}_i. \tag{1.4}$$

The second term on the left-hand side of (1.3) can be written as

$$\mathbf{a}_i^T \dot{\mathbf{Q}}\mathbf{b}_i = \mathbf{a}_i^T \boldsymbol{\Omega}\mathbf{Q}\mathbf{b}_i = \mathbf{a}_i^T [\boldsymbol{\omega} \times (\mathbf{Q}\mathbf{b}_i)] = [(\mathbf{Q}\mathbf{b}_i) \times \mathbf{a}_i]^T \boldsymbol{\omega} \tag{1.5}$$

where $\boldsymbol{\omega}$ is the angular velocity vector of the platform and $\boldsymbol{\Omega}$ is the angular velocity tensor, i.e.,

$$\dot{\mathbf{Q}} = \boldsymbol{\Omega}\mathbf{Q}. \tag{1.6}$$

Also the right-hand side of (1.3) can be written as

$$\mathbf{a}_i^T \dot{\mathbf{s}}_i = \mathbf{a}_i^T (\mathbf{M}_i \dot{\boldsymbol{\theta}}_i) = \mathbf{k}_i^T \dot{\boldsymbol{\theta}}_i \tag{1.7}$$

where $\dot{\boldsymbol{\theta}}_i = [\dot{\theta}_{i1}\ \dot{\theta}_{i2}\ \dot{\theta}_{i3}]^T$ is the vector of actuated joint velocities of the ith leg, while

$$\mathbf{k}_i^T = \mathbf{a}_i^T \mathbf{M}_i, \qquad i = 1, 2, 3 \tag{1.8}$$

is a 1×3 line vector, and $\mathbf{M}_i$ is the Jacobian matrix of the ith leg when considered as a 3-dof robot that is used to position point S_i. This matrix is readily obtained by considering the kinematics of the leg, as shown in Fig. 1.3. The detailed derivation is given in Appendix A. One obtains

$$\mathbf{A}_i \dot{\mathbf{s}}_i = \mathbf{B}_i \dot{\boldsymbol{\theta}}_i, \qquad i = 1, 2, 3 \tag{1.9}$$

where

$$\mathbf{A}_i = \begin{bmatrix} \mathbf{e}_{i2}^T \\ \mathbf{v}_{i1}^T \\ 1 - \frac{l_{i5}}{l_{i6}} \mathbf{v}_{i2}^T \end{bmatrix}, \quad i = 1, 2, 3 \tag{1.10}$$

and

$$\mathbf{B}_i = \begin{bmatrix} b_{i11} & 0 & 0 \\ 0 & \mathbf{v}_{i1}^T (\mathbf{e}_{i2} \times \mathbf{u}_{i1}) & 0 \\ 0 & b_{i32} & \mathbf{v}_{i2}^T (\mathbf{e}_{i3} \times \mathbf{u}_{i2}) \end{bmatrix} \tag{1.11}$$

with

$$b_{i11} \quad = \quad (\mathbf{s}_i - \mathbf{c}_i)^T (\mathbf{e}_{i2} \times \mathbf{e}_{i1}) \tag{1.12}$$

$$b_{i32} = \frac{l_{i5}}{l_{i6}} \mathbf{v}_{i2}^T (\mathbf{u}_{i1} \times \mathbf{e}_{i2}) \tag{1.13}$$

$$\mathbf{v}_{i1} = \mathbf{s}_i - \mathbf{c}_i - \mathbf{u}_{i1} \tag{1.14}$$

$$\mathbf{v}_{i2} = \mathbf{u}_{i1} + \mathbf{w}_i - \mathbf{u}_{i2}. \tag{1.15}$$

Finally, matrix $\mathbf{M}_i$ can be written as

$$\mathbf{M}_i = \mathbf{A}_i^{-1} \mathbf{B}_i, \quad i = 1, 2, 3. \tag{1.16}$$

To assemble the kinematics of the global robot, it is now possible to combine (1.3), (1.5) and (1.7) to obtain

$$\begin{bmatrix} \mathbf{a}_1^T & [(\mathbf{Q}\mathbf{b}_1) \times \mathbf{a}_1]^T \\ \mathbf{a}_2^T & [(\mathbf{Q}\mathbf{b}_2) \times \mathbf{a}_2]^T \\ \mathbf{a}_3^T & [(\mathbf{Q}\mathbf{b}_3) \times \mathbf{a}_3]^T \end{bmatrix} \begin{bmatrix} \dot{\mathbf{p}} \\ \boldsymbol{\omega} \end{bmatrix} = \begin{bmatrix} \mathbf{k}_1 & \mathbf{0} & \mathbf{0} \\ \mathbf{0} & \mathbf{k}_2 & \mathbf{0} \\ \mathbf{0} & \mathbf{0} & \mathbf{k}_3 \end{bmatrix}^T \dot{\boldsymbol{\theta}} \tag{1.17}$$

where $\mathbf{0}$ stands for the three-dimensional zero column vector, namely $\mathbf{0} = [0\ 0\ 0]^T$ and $\dot{\boldsymbol{\theta}} = [\dot{\boldsymbol{\theta}}_1^T\ \dot{\boldsymbol{\theta}}_2^T\ \dot{\boldsymbol{\theta}}_3^T]^T$ is the vector containing the 9 actuated joint velocities. Since vector $\mathbf{k}_i$ is of dimension 3×1, the first matrix appearing on the right-hand side of (1.17) is of dimension 3×9. Equation (1.17) contains the three velocity equations obtained from the first set of geometric constraints given by (1.1).

The second set of geometric constraints, given by (1.2), is now considered. Similarly to the above derivation, the time derivative of (1.2) yields

$$\dot{\mathbf{q}}_z^T \mathbf{a}_i + \mathbf{q}_z^T (\dot{\mathbf{p}} + \dot{\mathbf{Q}}\mathbf{b}_i - \dot{\mathbf{s}}_i) = 0 \tag{1.18}$$

which can be rewritten as

$$\mathbf{a}_i^T \dot{\mathbf{q}}_z + \mathbf{q}_z^T \dot{\mathbf{p}} + \mathbf{q}_z^T \dot{\mathbf{Q}}\mathbf{b}_i = \mathbf{q}_z^T \dot{\mathbf{s}}_i \tag{1.19}$$

in which

$$\mathbf{q}_z = \mathbf{Q}[\boldsymbol{z}']_{O'} \tag{1.20}$$

where $[\boldsymbol{z}']_{O'} = [0\ 0\ 1]^T$ represents the $\boldsymbol{z}'$ axis and is expressed in the moving frame, and

$$\dot{\mathbf{q}}_z = \dot{\mathbf{Q}}[\boldsymbol{z}']_{O'} = \boldsymbol{\Omega}\mathbf{q}_z. \tag{1.21}$$

With a derivation similar to the one given in (1.5), and using (1.21), the first term in (1.19) can be rewritten as

$$\mathbf{a}_i^T \dot{\mathbf{q}}_z = (\mathbf{q}_z \times \mathbf{a}_i)^T \boldsymbol{\omega} \tag{1.22}$$

and the third term in (1.19) can be rewritten as

$$\mathbf{q}_z^T \dot{\mathbf{Q}}\mathbf{b}_i = [(\mathbf{Q}\mathbf{b}_i) \times \mathbf{q}_z]^T \boldsymbol{\omega}. \tag{1.23}$$

Adding (1.22) and (1.23) then yields

$$(\mathbf{q}_z \times \mathbf{a}_i)^T \boldsymbol{\omega} + [(\mathbf{Q}\mathbf{b}_i) \times \mathbf{q}_z]^T \boldsymbol{\omega} = [(\mathbf{Q}\mathbf{b}_i - \mathbf{a}_i) \times \mathbf{q}_z]^T \boldsymbol{\omega}. \tag{1.24}$$

Now let

$$\mathbf{u}_i = \mathbf{Q}\mathbf{b}_i - \mathbf{a}_i \tag{1.25}$$

which is the vector from point O' to the centre of joint S_i. Then, (1.19) can be rewritten as

$$\mathbf{q}_z^T \dot{\mathbf{p}} + (\mathbf{u}_i \times \mathbf{q}_z)^T \boldsymbol{\omega} = \mathbf{q}_z^T \dot{\mathbf{s}}_i \tag{1.26}$$

in which

$$\mathbf{q}_z^T \dot{\mathbf{s}}_i = \mathbf{q}_z^T (\mathbf{M}_i \dot{\boldsymbol{\theta}}_i) = \mathbf{k}_{i+3}^T \dot{\boldsymbol{\theta}}_i, \qquad i = 1, 2, 3 \tag{1.27}$$

where $\mathbf{M}_i$ is defined in (1.16) and

$$\mathbf{k}_{i+3}^T = \mathbf{q}_z^T \mathbf{M}_i \tag{1.28}$$

is a line vector of dimension 1×3. Rewriting (1.26) in matrix form, we obtain

$$\begin{bmatrix} \mathbf{q}_z^T & (\mathbf{u}_1 \times \mathbf{q}_z)^T \\ \mathbf{q}_z^T & (\mathbf{u}_2 \times \mathbf{q}_z)^T \\ \mathbf{q}_z^T & (\mathbf{u}_3 \times \mathbf{q}_z)^T \end{bmatrix} \begin{bmatrix} \dot{\mathbf{p}} \\ \boldsymbol{\omega} \end{bmatrix} = \begin{bmatrix} \mathbf{k}_4 & \mathbf{0} & \mathbf{0} \\ \mathbf{0} & \mathbf{k}_5 & \mathbf{0} \\ \mathbf{0} & \mathbf{0} & \mathbf{k}_6 \end{bmatrix}^T \dot{\boldsymbol{\theta}}. \tag{1.29}$$

Equation (1.29) contains the three velocity equations obtained from the second set of constraints given by (1.2).

Finally, combining (1.17) and (1.29) and rearranging the components, we obtain

$$\mathbf{J}\mathbf{t} = \mathbf{K}\dot{\boldsymbol{\theta}} \tag{1.30}$$

where $\mathbf{t} = [\dot{\mathbf{p}}^T \ \boldsymbol{\omega}^T]^T$ is the vector of Cartesian velocities of the platform, and matrices $\mathbf{J}$ and $\mathbf{K}$ have the following form

$$\mathbf{J} = \begin{bmatrix} \mathbf{a}_1^T & [(\mathbf{Q}\mathbf{b}_1) \times \mathbf{a}_1]^T \\ \mathbf{q}_z^T & (\mathbf{u}_1 \times \mathbf{q}_z)^T \\ \mathbf{a}_2^T & [(\mathbf{Q}\mathbf{b}_2) \times \mathbf{a}_2]^T \\ \mathbf{q}_z^T & (\mathbf{u}_2 \times \mathbf{q}_z)^T \\ \mathbf{a}_3^T & [(\mathbf{Q}\mathbf{b}_3) \times \mathbf{a}_3]^T \\ \mathbf{q}_z^T & (\mathbf{u}_3 \times \mathbf{q}_z)^T \end{bmatrix} \tag{1.31}$$

$$\mathbf{K} = \begin{bmatrix} \mathbf{k}_1^T & \mathbf{0}^T & \mathbf{0}^T \\ \mathbf{k}_4^T & \mathbf{0}^T & \mathbf{0}^T \\ \mathbf{0}^T & \mathbf{k}_2^T & \mathbf{0}^T \\ \mathbf{0}^T & \mathbf{k}_5^T & \mathbf{0}^T \\ \mathbf{0}^T & \mathbf{0}^T & \mathbf{k}_3^T \\ \mathbf{0}^T & \mathbf{0}^T & \mathbf{k}_6^T \end{bmatrix} \tag{1.32}$$

where, as mentioned above, $\mathbf{0}$ stands for a zero column vector of dimension 3×1. Equation (1.30) represents the velocity equation of the (6+3)-dof kinematically redundant robot. It can be observed that matrix $\mathbf{J}$ is of dimension 6×6 while matrix $\mathbf{K}$ is of dimension 6×9. The dimensions of the matrices reflect the redundancy of the mechanism, which has in fact 9 degrees of freedom and 9 actuators.

1.4 Singularity Analysis

One of the main reasons for the limited orientational workspace of spatial parallel robots is the occurence of singularities. Moreover, the translational workspace can always be increased by scaling up the robot but this operation has no impact on the orientational workspace. Therefore, the singularity analysis is a very important component of the assessment of the performances of parallel robots. In this section, it will be shown that the singular configurations of the proposed redundant hybrid parallel robot are easily avoided, which yields an orientational workspace that is much larger than that of typical parallel mechanisms.

The singularities of the proposed robot architecture can be divided into two categories, namely the singularities (serial and parallel) occuring in one of the legs and the parallel (type II) singularities of the platform. Since the legs include a serial and a parallel component, the singularities occuring in one of the legs can be of either type. However, because of the simple architecture of the legs — one revolute joint in series with a planar five-bar linkage — the analysis of the singularities occuring in a leg is rather straightforward. The type I (serial) singularities of a leg occur when matrix $\mathbf{B}_i$, defined in (1.11), is singular. Such a singularity occurs if the spherical joint is located on the axis of the first revolute joint. In this case one has $b_{i11} = 0$ which makes matrix $\mathbf{B}_i$ singular. This is avoided in the final design by making the first joint horizontal, i.e., $\alpha = \pi$, which renders this configuration unreachable. A type I singularity also occurs if $\mathbf{v}_{i1}$ is orthogonal to $(\mathbf{e}_{i2} \times \mathbf{u}_{i1})$ or if $\mathbf{v}_{i2}$ is orthogonal to $(\mathbf{e}_{i3} \times \mathbf{u}_{i2})$. It is rather straightforward to avoid such configurations by a proper dimensioning of the 5-bar linkage to make these configurations correspond to the limits of the workspace. The type II singularities that can occur in a leg correspond to a singularity of matrix $\mathbf{A}_i$, defined in (1.10). In this matrix, the first row is always orthogonal to the last two. Therefore, singularities can occur if the last two rows become linearly dependent. From the structure of the matrix, it is easy to see that this condition corresponds to the alignment of links $i3$ and $i5$. These configurations are easily avoided in practice. In summary, the possible singularities of the legs are easily handled.

Our attention is now turned to the singular configurations of the moving platform (parallel singularities of the robot), which are typically the most limitative for parallel or hybrid parallel robots. Indeed, such singularities greatly limit the orientational workspace of spatial parallel mechanisms like the Gough-Stewart platform. The type II singularities occur when $\det(\mathbf{J}) =$

0, where $\mathbf{J}$ is the Jacobian matrix defined in (1.31). It is observed that, in the proposed mechanism, the spherical joint S_i is followed by link $i7$ and a revolute joint attached to the platform. With such an arrangement, we can always find two lines expressed by Plücker coordinates corresponding to the constraints on the platform provided by each leg: one of them is parallel to the unit vector $\mathbf{q}_z$ while the other is along vector $\mathbf{a}_i$, as shown in Fig. 1.3 (dashed lines). In each leg, these two lines intersect at the centre of joint S_i and they are perpendicular to each other. The Jacobian matrix $\mathbf{J}$ is simply the combination of these six Plücker lines. By introducing GLG, the singular conditions of the mechanism can be determined geometrically. In order to simplify the singularity analysis, we can divide the six lines into two sets and we show that we can investigate them independently. The first set contains the three lines parallel to unit vectors $\mathbf{q}_z$ and the other set is formed by the three lines along vectors $\mathbf{a}_i$. It can be observed, from Fig. 1.3, that the three lines along $\mathbf{q}_z$ are parallel to each other in space while the three lines along $\mathbf{a}_i$ are coplanar. The rationality of dividing these six Plücker lines in two groups can be proved mathematically. Assume that the lines are expressed in an arbitrary frame whose origin is located on the plane formed by vectors $\mathbf{a}_i$ and whose z-axis is in the direction of the three unit vectors $\mathbf{q}_z$. If the Plücker coordinates of the lines expressed in this frame are noted $[d_j\ m_j\ n_j;\ p_j\ q_j\ w_j], j = 1, \ldots, 6$, then the Plücker coordinates of the lines belonging to set one can be written as

$$\mathbf{J}_n = \begin{bmatrix} 0 & 0 & 1 & p_1 & q_1 & 0 \\ 0 & 0 & 1 & p_2 & q_2 & 0 \\ 0 & 0 & 1 & p_3 & q_3 & 0 \end{bmatrix} \tag{1.33}$$

while the Plücker coordinates of the lines belonging to set two can be expressed as

$$\mathbf{J}_a = \begin{bmatrix} d_4 & m_4 & 0 & 0 & 0 & w_4 \\ d_5 & m_5 & 0 & 0 & 0 & w_5 \\ d_6 & m_6 & 0 & 0 & 0 & w_6 \end{bmatrix}. \tag{1.34}$$

As mentioned above, these lines are represented as dashed lines going through joint S_i in Fig. 1.3. It can be observed that each line in matrix $\mathbf{J}_n$ is linearly independent from the lines in matrix $\mathbf{J}_a$ and vice versa. Therefore, it suffices to analyse each of the sets independently in order to determine the singular configurations. According to GLG, the largest number of linearly independent lines for spatial parallel lines or for coplanar lines — which is the case for each of the two sets here — is three. For any one of the two sets, a singularity may occur when the three lines intersect at one point or when they are parallel to each other on a plane. However, such singularities are easily avoidable for the proposed robot, as explained in the following subsections.

1.4.1 Singularity of Set One

In this case, the ith line ($i = 1, 2, 3$) parallel to $\mathbf{q}_z$ passes through point S_i and is restricted to rotate around the axis of the ith revolute joint attached to the platform. Its possible locations

form the contour of a cylinder of radius equal to l_{i7}. We therefore have three cylinders with parallel axes. Singularities may occur when the three lines, one on each cylinder, become coplanar. A simple way to avoid this possibility is to make the links $i7$ relatively short with respect to the platform in order to ensure that the cylinders are sufficiently far from one another, i.e., to ensure that no straight line can go through all 3 cylinders. This is easily taken care of at the design stage. For example, if the platform is an equilateral triangle with a circumradius r, one should have

$$l_{i7} < \frac{3}{4} r \tag{1.35}$$

in order to prevent such singularities (Wen et al., 2019).

1.4.2 Singularity of Set Two

Here, for this set of lines, the advantages of using kinematically redundant legs are reflected most vividly. A type II singularity occurs when the three coplanar Plücker lines belonging to this set intersect at a common point or are parallel to each other. However, such singular configurations can be avoided by reorienting one or two of the three links $i7$, using the kinematic redundancy, without changing the configuration of the platform. Moreover, it should be noted that although in principle using only two redundant legs is sufficient to avoid this set of singularities, we use three, such that we can always ensure that the robot is in a well-conditioned configuration, which keeps the platform far away from type II singularities, passive joint limits and mechanical interferences. This arrangement will be explained in the next section. With three redundant legs, it is possible, for instance, to maintain the relative angle between the links $i7$ and the platform constant, in a well conditioned arrangement, thereby completely avoiding singularities in all configurations of the platform while greatly simplifying the redundancy resolution.

As a comparison, consider the non-redundant robot developed in (Monsarrat and Gosselin, 2001), which is akin to the robot proposed in this paper. In the non-redundant robot presented in (Monsarrat and Gosselin, 2001), the six Plücker lines are associated with the six actuated input angles. For a given pose (position and orientation) of the platform, their directions cannot be changed, which yields unavoidable type II singularities. By contrast, in the redundant mechanism proposed here, the directions of the lines can be changed using the redundancy without affecting the pose of the platform. Except for the leg singularities, the present mechanism has only two different kinds of type II singularities and both of these are easily avoidable, as discussed above. However, for the non-redundant counterpart, five different kinds of singularities must be considered and no effective approach can be used to avoid them. The workspace — especially the orientational workspace — is considerably limited compared to that of the redundant mechanism proposed here. As an illustration of the capabilities of the proposed robot, its orientational workspace is shown in Section 1.7 (Fig. 1.8) for the reference position, considering all possible leg and platform interferences. It can be

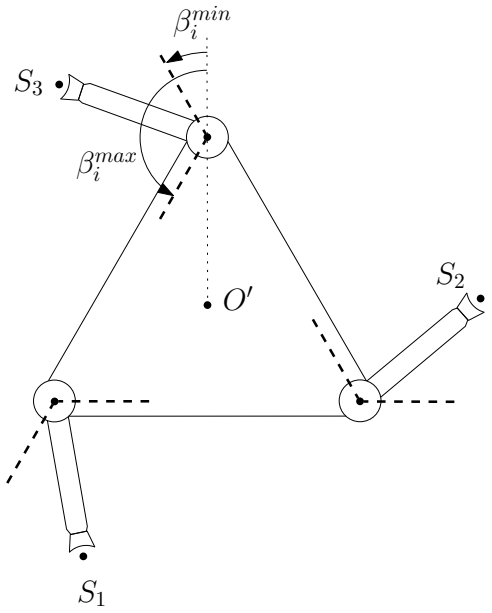

Figure 1.4 – Ranges of orientation of the distal links (domains for β_i) where singularity avoidance is guaranteed: $\beta_i \in [30°,\ 150°], i = 1, 2, 3$ (Wen et al., 2019).

readily observed that the robot is capable of very large tilt angles, which are far beyond the capabilities of other similar non-redundant parallel mechanisms. It should also be pointed out that the passive spherical joints, S_i, must have very large motion ranges to accommodate this motion. Such joints have been developed in (Schreiber and Gosselin, 2017) and are hence available.

1.4.3 Type II Singularity-free Range

The redundancy was used to avoid singular configurations, which leaves infinitely many non-singular configurations for a given position and orientation of the platform. Considering again the platform and the links $i7$, it can be readily observed, as shown in Fig. 1.4 that if links $i7$ are maintained at an angle comprised within the ranges illustrated, namely $\beta_i \in [\beta_i^{min},\ \beta_i^{max}] = [30°,\ 150°]$, then type II singularities can never occur (the three lines can never become dependent). This is also confirmed by the singularity locus, plotted in the $[\beta_1,\ \beta_2,\ \beta_3]$ space in Fig. 1.5. Indeed, it can readily be determined, from this graph, that a box defined as

$$30° < \beta_i < 150°, \quad i = 1, 2, 3 \tag{1.36}$$

is free from singularities.

1.5 Inverse Kinematics

The inverse kinematics of most redundant manipulators is solvable only using numerical methods, which is achieved at the velocity level (Siciliano, 1990). For the hybrid robot proposed

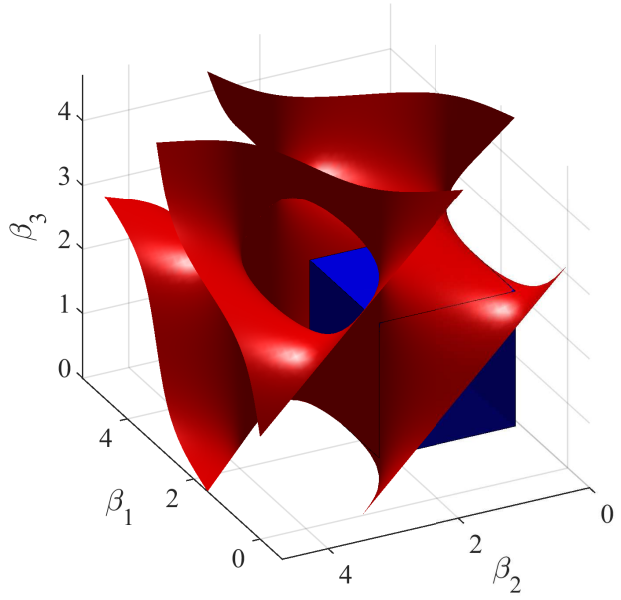

Figure 1.5 – Singularity locus of the proposed robot. The unit of $\beta_i, i = 1, 2, 3$ in this figure is radian. It is noted that this singularity locus is defined in the space of the redundant degrees of freedom and is independent from the position and orientation of platform. The box shown in blue represents the singularity-free zone corresponding to the inequalities given in (1.36).

here, an analytical solution to the inverse kinematics which is straightforward, consistent and conservative — thus overcoming the repeatability problem — can be obtained. Indeed, as explained in the singularity analysis presented above, it is possible to assign values to the angles β_i (see Fig. 1.3), which represent the redundant degrees of freedom, independently from the platform pose. For example, angles β_i can be prescribed to remain constant at all times, in order to generate a configuration that always remains far away from singularities.

Therefore, for a given pose of the platform (vector $\mathbf{p}$ and matrix $\mathbf{Q}$) and with given values of angles β_i, the position of the spherical joint, vector $\mathbf{s}_i$, in each of the legs is readily computed as

$$\mathbf{s}_i = \mathbf{p} + \mathbf{Q}\mathbf{b}_i - \mathbf{a}_i, \quad i = 1, 2, 3. \tag{1.37}$$

Once these vectors are obtained, each of the legs can be considered as a 3-dof robot that is used to position the spherical joint and an analytical solution of the inverse kinematics is readily obtained for such a robot. Due to the 5-bar linkages in the legs, this problem admits at most 8 solutions and the branches of solution are easily determined. The detailed equations are straightforward and are given in Appendix B. These equations are used to determine the workspace and other characteristics of the robot.

As a comparison, consider the (6+3)-dof redundant parallel robot proposed in (Gosselin and

Schreiber, 2016). It was shown that all singularities can be avoided for this robot by exploiting the redundancy. However, the redundancy resolution must be computed numerically and the conservative nature of the solution cannot be guaranteed. By contrast, the redundancy resolution of the robot proposed here is straightforward and conservative while requiring almost no computations.

1.6 Forward Kinematics

When all actuator coordinates are prescribed, the position of each spherical joint is readily obtained by solving the forward kinematics of each of the legs. The solution of this problem is straightforward and leads to two solutions in each leg, because of the 5-bar linkage arrangement. Also, the robot is designed to always operate in one of these two solutions and a unique solution is readily determined. Once the positions of the three spherical joints are obtained, the position and orientation of the moving platform can be computed using the same formulation as for planar 3-dof parallel manipulators (Gosselin et al., 1992), applied in the plane formed by the three spherical joints. This formulation yields a sixth order polynomial equation. Nevertheless, it should be pointed out that, in practice, a numerical solution is used since this problem is solved only based on a known initial guess that is very close to the actual solution. Also, because the robot configuration is always far from singularities, the numerical procedure converges stably and quickly. Globally, the direct kinematics of the proposed robot is significantly simpler than that of other kinematically redundant parallel robots such as the one proposed in (Gosselin and Schreiber, 2016). A more detailed analysis on the forward kinematics will be given in Chapter 3.

1.7 Workspace

For illustrative purposes, the geometric parameters used for the workspace evaluation of the proposed robot are chosen as follows:

$$
\begin{aligned}
&R_b = 250 \text{ mm}, \quad R_p = 125 \text{ mm}, \quad l_{i1} = l_{i7} = 50 \text{ mm} \\
&l_{i2} = 150 \text{ mm}, \quad l_{i5} = 450 \text{ mm}, \quad l_{i3} = l_{i4} = l_{i6} = 300 \text{ mm}, \\
&\alpha = 120^\circ, \quad \beta_i = 97^\circ, \quad i = 1, 2, 3
\end{aligned}
$$

where R_b and R_p are respectively the circumradius of the base and platform and angles β_i are chosen such that the robot will never be in a type II singular configuration. The geometric parameters of the robot are chosen based on a design exercise with the consideration that the size of the prototype be suitable and convenient for pHRI. The analytical inverse kinematic solution is exploited for planning the motions of the robot and a discretization method is implemented in the evaluations.

1.7.1 Translational Workspace

In this evaluation, the orientation of the platform is $\mathbf{Q} = \mathbf{I}$, where $\mathbf{I}$ is the 3×3 identity matrix. The base of the mechanism is regarded as the lower boundary of the workspace. In order to prevent the type I singularities, the minimal perpendicular distance between the centre of the ith spherical joint and the axis of corresponding first actuated revolute joint is set to be 20 mm, and the range of the angle between vectors $\mathbf{u}_{i1}$ and $\mathbf{w}_i$ (see Fig. 1.3) is limited to be $[10°, 170°]$. Each link of the robot is modeled as a cylinder with a radius of 7.5 mm. A safety distance, d, between each pair of not directly connected cylinders is set to $d = 5$ mm. A mechanical interference occurs when $d < 5$ mm.

The position of the platform during the evaluation is given as

$$\mathbf{p} = \begin{bmatrix} d_p \cos\theta_c & d_p \sin\theta_c & h \end{bmatrix}^T \tag{1.38}$$

with

$$0 \leq d_p \leq d_{p,max}, \quad 0 \leq \theta_c \leq 2\pi, \quad \text{and} \quad 0 \leq h \leq h_{max}, \tag{1.39}$$

where d_p is the distance that the platform moved in a direction defined by angle θ_c, and h is the height (along the z-axis of the base frame) of the platform. The simulation intervals of d_p and h, and of θ_c , are set to 1 mm and 1°, respectively. These intervals, as well as those set for assessing the orientational workspace in the next subsection, are chosen based on the compromise between the calculation time and accuracy of the obtained workspace. The platform reaches the boundary of the workspace ($d_p = d_{p,max}$ or $h = h_{max}$) if passive spherical joint limits or mechanical interferences are detected. In addition, we assume that the novel 4-dof spherical joint with a large motion range of ±150° (Schreiber and Gosselin, 2017) is used instead of the common ball and socket joints. In fact, the 4-dof spherical joints proposed in (Schreiber and Gosselin, 2017) are used in the prototype of the proposed robot. The results of the workspace evaluation are presented in Figs. 1.6 and 1.7. It can be observed that the robot is singularity-free throughout the translational workspace. However, due to the type I singularity condition (one), the lower part of the workspace is limited (the recessed parts appearing in Fig. 1.7). As mentioned, this limitation can be improved by increasing the angle α. Indeed, if $\alpha = \pi$, the translational workspace will be convex, which is a desirable property for parallel mechanisms. In fact, $\alpha = \pi$ is chosen in the prototype described in an upcoming section. Also, as a comparison, for the non-redundant counterpart of the proposed robot (Monsarrat and Gosselin, 2003), the translational workspace might be split into different regions due to singularities.

1.7.2 Orientational Workspace

The orientational workspace was evaluated when the position of the platform is fixed at $\mathbf{p} = [0\ 0\ 350]^T$ mm. Type I singularities are completely excluded in this location. Thereby, the orientational workspace is limited only by the passive spherical joint limits and mechanical

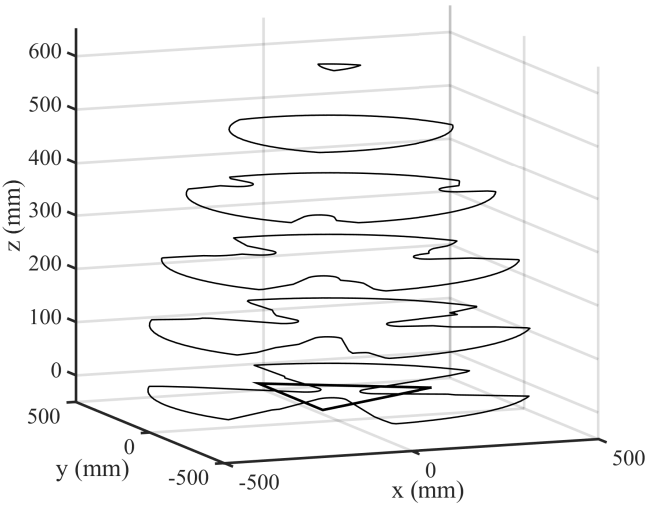

Figure 1.6 – The contours of several layers of the translational workspace of the proposed architecture.

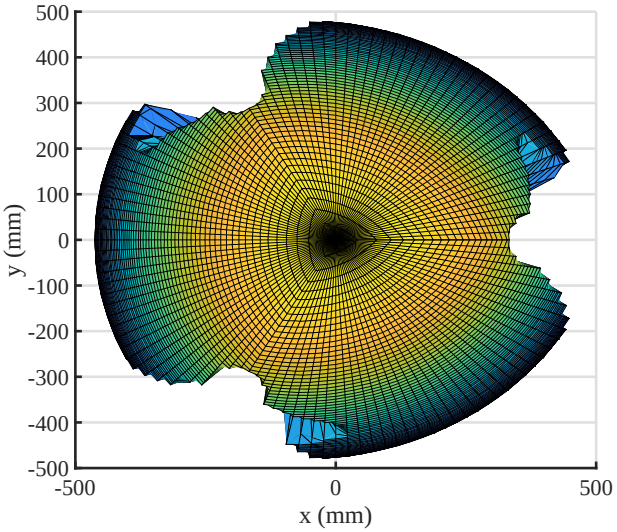

Figure 1.7 – Translational workspace (top view) of the proposed architecture.

interferences. The orientation of the platform in this evaluation is given by the following rotation matrix

$$\mathbf{Q} = \mathbf{Q}_{torsion}\mathbf{Q}_{tilt} \tag{1.40}$$

where

$$\mathbf{Q}_{torsion} = \begin{bmatrix} \cos\psi & -\sin\psi & 0 \\ \sin\psi & \cos\psi & 0 \\ 0 & 0 & 1 \end{bmatrix} \tag{1.41}$$

which is a rotation of the platform by a torsion angle ψ with respect to the z-axis of the base frame, and in which

$$\psi_{min} \leq \psi \leq \psi_{max}, \tag{1.42}$$

and

$$\mathbf{Q}_{tilt} = \begin{bmatrix} \cos\phi + u_{x'}^2(1-\cos\phi) & u_{x'}u_{y'}(1-\cos\phi) & u_{y'}\sin\phi \\ u_{x'}u_{y'}(1-\cos\phi) & \cos\phi + u_{y'}^2(1-\cos\phi) & -u_{x'}\sin\phi \\ -u_{y'}\sin\phi & u_{x'}\sin\phi & \cos\phi \end{bmatrix} \tag{1.43}$$

with

$$0 \leq \phi \leq \phi_{max}, \tag{1.44}$$

and where $u_{x'}$ and $u_{y'}$ are respectively the x' and y' components of a unit vector $\mathbf{u}$, namely

$$\mathbf{u} = \begin{bmatrix} u_{x'} \\ u_{y'} \\ 0 \end{bmatrix} = \begin{bmatrix} \cos\theta_c \\ \sin\theta_c \\ 0 \end{bmatrix} \tag{1.45}$$

which is expressed in the platform frame $O'x'y'z'$, and angle θ_c is defined in (1.38). Matrix $\mathbf{Q}_{tilt}$ represents a rotation of the platform by a tilt angle ϕ with respect to the unit vector $\mathbf{u}$. The simulation interval of angles ψ, ϕ and θ_c are all set to 1°. The orientational workspace is also conducted in two steps. We first figure out the maximum and minimum torsion angles, ψ_{max} and ψ_{min}, by leaving the term Q_{tilt} out of (1.40). Then, for each value of ψ, the maximum tilt angle, ϕ_{max}, is determined by tilting the platform with respect to the unit vector $\mathbf{u}$ defined by each value of θ_c.

Tilt and torsion angles are used to illustrate the orientational workspace (Bonev et al., 2002). The result is shown in Fig. 1.8. Cylindrical coordinates (z, r, θ_c) are used in this representation, where the z-axis stands for the torsion angle (ψ), the radius r stands for the tilt angle (ϕ), and θ_c is given in (1.45). It can be seen that a large span of the torsion angle (220°) can be reached. In Fig. 1.9, a section of the workspace corresponding to zero torsion is presented. It can be observed that the platform can reach a very large tilt angle of more than ±135° in certain directions. In the worst directions, the tilt angles can still be much larger than 90°. These results clearly show that the platform can produce an excellent rotational performance. By contrast, due to singularities, the maximum tilt angle of a Gough-Stewart platform in most cases is approximately 45°, and it is approximately 40° for the non-redundant counterpart of the proposed robot (Monsarrat and Gosselin, 2003).

1.8 Example

In this section, a tilt simulation is conducted to demonstrate the excellent rotation ability of the platform. Different performance indices are detected during the motion. The platform is initially at $\mathbf{p} = [0\ 0\ 350]^T$ mm, with $\mathbf{Q} = \mathbf{I}$ and $\beta_i = 97°, i = 1, 2, 3$. The angles β_i are maintained for the whole trajectory.

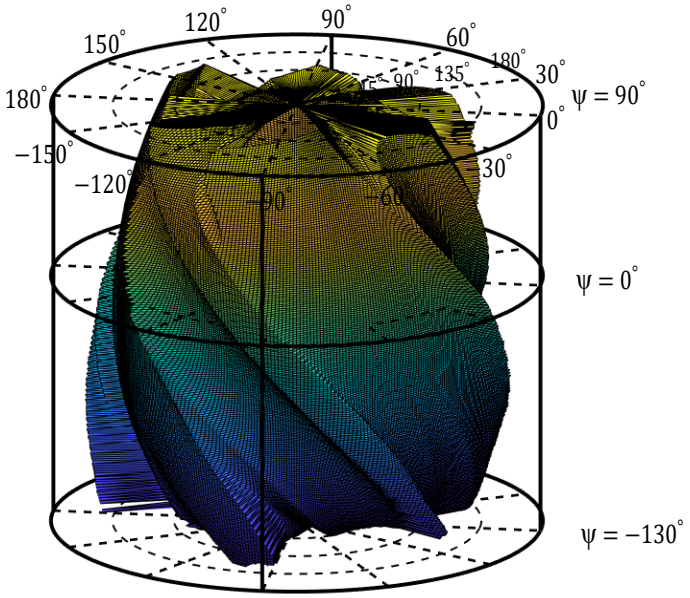

Figure 1.8 – Orientational workspace of the proposed architecture in the reference position.

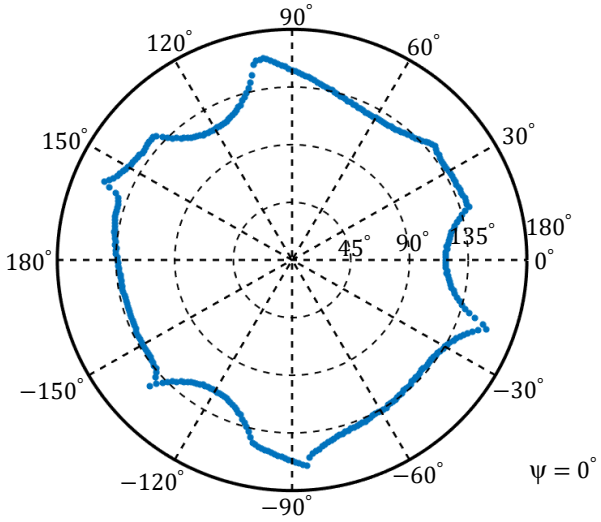

Figure 1.9 – The largest tilt angles of a section (zero torsion) of the proposed architecture.

The trajectory is divided into the following five sub-trajectories. The equation of the sub-trajectory one is given as

$$\mathbf{Q} = \begin{bmatrix} \cos\phi & 0 & \sin\phi \\ 0 & 1 & 0 \\ -\sin\phi & 0 & \cos\phi \end{bmatrix} \quad \text{with} \quad 0 \leq \phi \leq \phi_{max} \tag{1.46}$$

which is a tilt rotation with respect to the y'-axis of the platform frame with $\phi_{max} = 80°$. The second sub-trajectory is a translation along the x-axis of the base frame

$$\mathbf{t}_x = [x\ 0\ 350]^T \text{ mm} \quad \text{with} \quad 0 \leq x \leq 100. \tag{1.47}$$

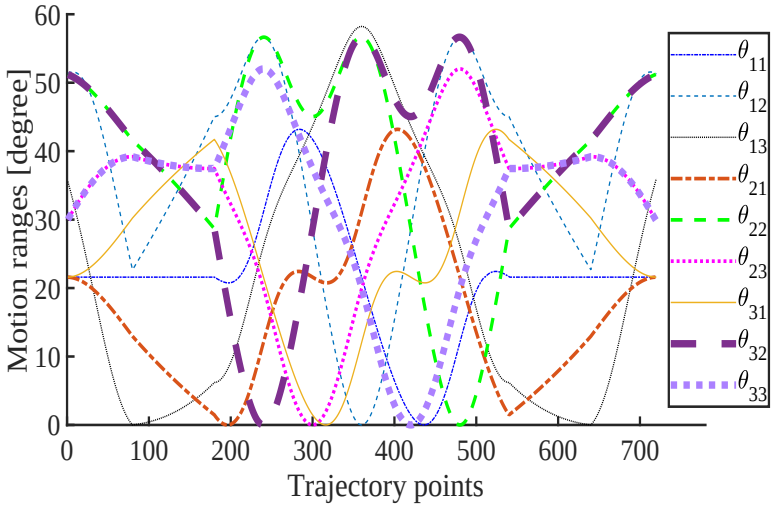

Figure 1.10 – Absolute motion range of the nine actuators for the example trajectory.

The third sub-trajectory is a circumferential tilt rotation, the orientation of the platform during this sub-trajectory is determined by the following rotation matrix (Gosselin and Schreiber, 2016)

$$\mathbf{Q} = \begin{bmatrix} \sin^2\zeta + \cos^2\zeta\cos\phi_{max} & \sin\zeta\cos\zeta(\cos\phi_{max}-1) & \cos\zeta\sin\phi_{max} \\ \sin\zeta\cos\zeta(\cos\phi_{max}-1) & \cos^2\zeta + \sin^2\zeta\cos\phi_{max} & \sin\zeta\sin\phi_{max} \\ -\cos\zeta\sin\phi_{max} & -\sin\zeta\sin\phi_{max} & \cos\phi_{max} \end{bmatrix}. \tag{1.48}$$

The position of the origin of the platform frame in this sub-trajectory is

$$\mathbf{p} = 100[\cos\zeta \;\; \sin\zeta \;\; 3.5]^T \text{ mm} \quad \text{with} \quad 0 \leq \zeta \leq 2\pi \tag{1.49}$$

which is a circular motion. The circle is parallel to the base and has a radius of 100 mm. At the end of this step, the platform is in the final configuration of sub-trajectory two. Finally, the platform is returned to the initial configuration by taking the opposite movements of sub-trajectories two and one.

The absolute motion range of actuators are measured throughout the trajectory. The results are shown in Fig. 1.10, in which $\theta_{ij}, i, j = 1, 2, 3$ denotes the absolute motion range of the jth actuator in the ith leg. It can be observed that the largest absolute motion range is no more than 60°, which is reasonable.

The 2-norm condition number of the Jacobian matrix is often used for describing the closeness of the platform to a singularity (Merlet, 2006a). However, it loses physical meaning when the units of the elements in the Jacobian are inconsistent. To overcome this, a new Jacobian matrix that transforms the velocities of three non-collinear points on the platform into actuator velocities is developed (Gosselin, 1990). For the proposed KRHR, rather than choosing three points on the platform, we prefer the centres of the three spherical joints. It is feasible since

all the angles β_i are remained constant in this example. For each sub-leg, as describe in (1.7), the velocity equations can be expressed as,

$$\dot{\mathbf{s}}_i = \mathbf{M}_i \dot{\boldsymbol{\theta}}_i, \quad i = 1, 2, 3 \tag{1.50}$$

where $\mathbf{M}_i$ has been given in (1.16) and in which all elements are with unit of length. The three equations in (1.50) can be combined into one formula,

$$\dot{\mathbf{s}} = \mathbf{J}_1 \dot{\boldsymbol{\theta}} \tag{1.51}$$

where $\dot{\mathbf{s}}$ is the 9×1 vector of the velocities of the centres of the three spherical joints, and

$$\mathbf{J}_1 = \begin{bmatrix} \mathbf{M}_1 & \mathbf{0} & \mathbf{0} \\ \mathbf{0} & \mathbf{M}_2 & \mathbf{0} \\ \mathbf{0} & \mathbf{0} & \mathbf{M}_3 \end{bmatrix} \tag{1.52}$$

in which $\mathbf{0}$ is the 3×3 zero matrix. Therefore, matrix $\mathbf{J}_1$ is of dimension 9×9 and is of full rank as long as none of $\mathbf{M}_i$ is singular. The 2-norm condition numbers of $\mathbf{J}_1$ and $\mathbf{M}_i$ for the example trajectory are shown in Fig. 1.11. These indices indicate the closeness of the robot to a type I singularity. The numerical values are very close to 1, which indicate that the platform or the ith sub-leg clearly stays away from the type I singularities.

Additionally, another two useful indices corresponding to kinematic sensitivity developed in (Cardou et al., 2010), namely: the 2-norm of the position part of matrix $\mathbf{U} = \mathbf{J}^{-1}\mathbf{K}$ (denoted as $\mathbf{U}_p$), and the the 2-norm of the rotation part of matrix $\mathbf{U}$ (denoted as $\mathbf{U}_r$), are also detected to verify the dexterity of the mechanism. These indices represent the maximum amplification from the resolution of the actuated revolute joints to the platform displacement and rotation. Since the numerical value of the 2-norm of $\mathbf{U}_p$ is unit sensitive, we choose metre as the unit of the elements involved in the computation of this index, in order to reduce the magnitude of the numerical value. The results of these indices for the example trajectory are illustrated in Fig. 1.12. It can be seen that the kinematic sensitivity of the robot is stable and excellent throughout the trajectory, thereby we acquire the same conclusion as that obtained based on the 2-norm condition number of Jacobian $\mathbf{J}_1$.

1.9 Conclusion

In this chapter, a novel (6+3)-dof KRHPR was introduced. It was shown that the type II singularities of the mechanism can be easily avoided by proper design and simple trajectory planning rules. As a result, the orientational workspace of the robot is very large when compared to other similar non-redundant parallel mechanisms. Although the architecture of the mechanism is not fully parallel, the moving actuators are located very close to the base and undergo motion with only a small amplitude, thereby greatly reducing the inertia of

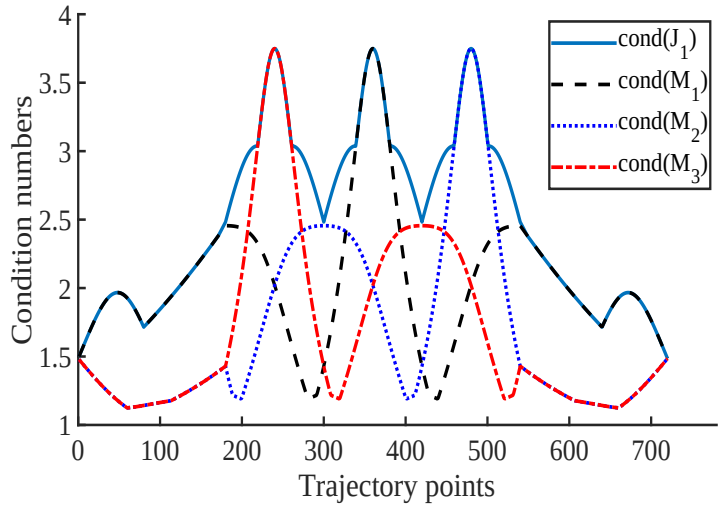

Figure 1.11 – Condition numbers of $\mathbf{J}_1$ and $\mathbf{M}_i, i = 1, 2, 3$ for the example trajectory.

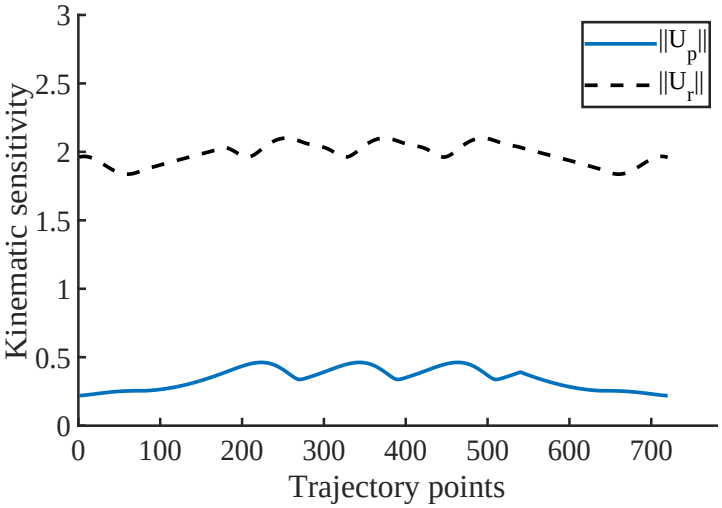

Figure 1.12 – Kinematic sensitivity for the example trajectory.

the moving components. Moreover, the robot is easily backdrivable due to the direct drive transmission. All of these indicate that the robot is well suited for pHRI applications.

Additionally, a video (animation) presents the (6+3)-dof KRHPR performing trajectories is available at: https://ieeexplore.ieee.org/abstract/document/8793772/media#media. It demonstrates the large orientationnal workspace of the robot by performing movements of tilt and torsion of the platform at +/− 90 degrees. It also shows the movement of the gripper, using two of the three redundant degrees of freedom to move each of the gripper fingers independently. Finally, a trajectory combining tilt, torsion and the opening/closing motion of the fingers is shown.

Chapter 2

KRHPRs with Simple Singularity Conditions and Analytical Inverse Kinematic Solutions

2.1 Introduction

Each leg of the KRHPR studied in Chapter 1 can be regarded as a combination of a fully actuated sub-leg and a redundant link. In this chapter, we generalise this concept and propose a class of planar and spatial KRHPRs. In the proposed architecture, the platform is connected to the base through three identical kinematically redundant legs. We introduce two different forms of redundant links, namely: revolute/spherical-revolute and revolute/spherical-prismatic links[1]. The links are attached to the moving platform in three different arrangements by revolute or prismatic joints (see Fig. 2.1). The axes of the revolute joints fixed on the platform shown in Fig. 2.1a are orthogonal to the platform plane. The composed KRHPRs are completely type II singularity-free, while the inverse kinematic problem can be solved analytically. These will be discussed in detail in the following sections.

The rest of this chapter is organized as follows. In Section 2.2, the velocity equations of the proposed planar KRHPRs are developed and the singularity conditions of the robots are investigated. Feasibility of using other types of planar sub-legs to compose the planar KRHPRs are explained. Section 2.3 focuses on the development of the velocity equations and singularity analysis of the spatial KRHPRs with three identical 3-dof revolute joint actuated serial sub-legs. Different types of mechanisms that can be used as sub-legs for spatial KRHPRs are enumerated in Section 2.4. Methods of solving the inverse kinematic problem of both planar and spatial KRHPRs are provided in Section 2.5. Finally, conclusions are drawn.

[1] Here, revolute/spherical means that in planar robots a revolute joint is used to connect the distal end of the sub-leg to the redundant link while in spatial robots a spherical joint is used for this purpose.

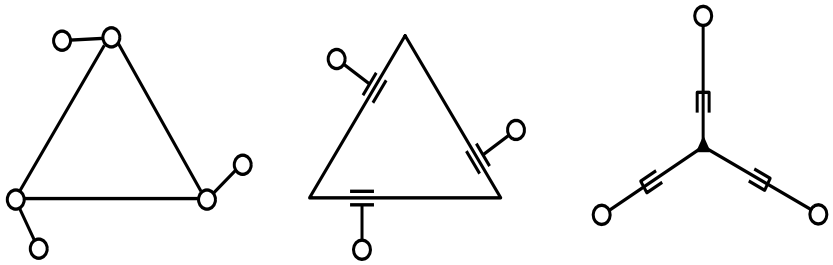

Figure 2.1 – Three different assembly arrangements of the platform and the redundant links: (a) R/S-R, (b) R/S-P, (c) R/S-P.

2.2 Planar Architectures

2.2.1 Velocity Equations of Architectures with Three Identical RR Sub-Legs

We start with a 3-RRRR planar KRHPR shown in Fig. 2.2. Here R and R denote the actuated and passive revolute joints. The length of the redundant RR link in each leg can be obtained as

$$(\mathbf{p} + \mathbf{Q}\mathbf{b}_i - \mathbf{r}_i)^T(\mathbf{p} + \mathbf{Q}\mathbf{b}_i - \mathbf{r}_i) = l^2, \quad i = 1, 2, 3 \tag{2.1}$$

where $\mathbf{Q}$ is the 2×2 orientation matrix of the platform frame with respect to the base frame, $\mathbf{p}$ is the position vector of the origin of the platform frame and $\mathbf{r}_i$ is the position vector of the third revolute joint of the ith leg. The time derivative of (2.1) yields

$$\mathbf{a}_i^T(\dot{\mathbf{p}} + \dot{\mathbf{Q}}\mathbf{b}_i - \dot{\mathbf{r}}_i) = 0 \tag{2.2}$$

where

$$\mathbf{a}_i = \mathbf{p} + \mathbf{Q}\mathbf{b}_i - \mathbf{r}_i \tag{2.3}$$

and where the product $\mathbf{a}_i^T\dot{\mathbf{r}}_i$ can be written as

$$\mathbf{a}_i^T\dot{\mathbf{r}}_i = \mathbf{a}_i^T\mathbf{M}_i\dot{\boldsymbol{\theta}}_i, \tag{2.4}$$

where $\mathbf{M}_i$ is the 2×2 Jacobian matrix of the ith serial RR sub-leg and $\dot{\boldsymbol{\theta}}_i = [\dot{\theta}_{i1}\ \dot{\theta}_{i2}]^T$.

Moreover, one has

$$\dot{\mathbf{Q}} = \dot{\phi}\mathbf{E}\mathbf{Q} \tag{2.5}$$

where $\dot{\phi}$ is the angular velocity of the platform and where

$$\mathbf{E} = \begin{bmatrix} 0 & -1 \\ 1 & 0 \end{bmatrix}. \tag{2.6}$$

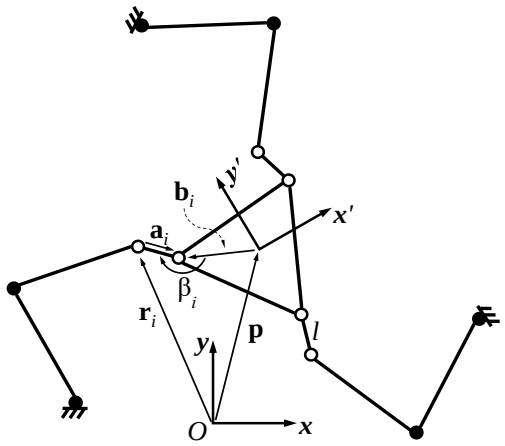

Figure 2.2 – Kinematic modelling of the 3-RRRR planar KRHPR.

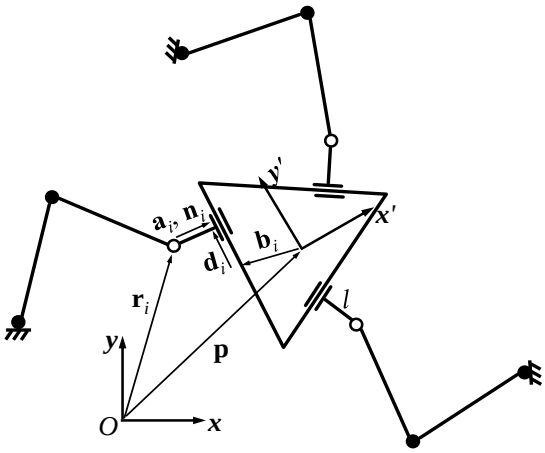

Figure 2.3 – Kinematic modelling of the 3-RRRP planar KRHPR with platform assembly arrangement (b) of Figure 2.1.

Then, defining $c_i = \mathbf{a}_i^T \mathbf{E}\mathbf{Q}\mathbf{b}_i$ and then substituting (2.4) and (2.5) into (2.2) yields the velocity equations of the robot, namely $\mathbf{J}\mathbf{t} = \mathbf{K}\dot{\boldsymbol{\theta}}$. In which the Jacobian matrices are respectively

$$\mathbf{J} = \begin{bmatrix} \mathbf{a}_1^T & c_1 \\ \mathbf{a}_2^T & c_2 \\ \mathbf{a}_3^T & c_3 \end{bmatrix}, \quad \mathbf{K} = \begin{bmatrix} \mathbf{a}_1^T\mathbf{M}_1 & \mathbf{0} & \mathbf{0} \\ \mathbf{0} & \mathbf{a}_2^T\mathbf{M}_2 & \mathbf{0} \\ \mathbf{0} & \mathbf{0} & \mathbf{a}_3^T\mathbf{M}_3 \end{bmatrix}, \tag{2.7}$$

where $\mathbf{0}$ is a 1×2 zero vector. Matrix $\mathbf{J}$ is of dimension 3×3 while matrix $\mathbf{K}$ is of dimension 3×6. And $\mathbf{t} = [\dot{\mathbf{p}}^T, \dot{\phi}]^T$ and $\dot{\boldsymbol{\theta}} = [\dot{\boldsymbol{\theta}}_1^T \ \dot{\boldsymbol{\theta}}_2^T \ \dot{\boldsymbol{\theta}}_3^T]^T$. In addition, each row in the Jacobian $\mathbf{J}$ represents a planar Plücker line along the direction of vector $\mathbf{a}_i$ and passes through both the passive revolute joints in the same leg.

For the assembly arrangements of the planar 3-RRRP architectures (see Figs. 2.3 and 2.4), the axis of the ith prismatic (abbreviated as P) joint is always perpendicular to a unit vector

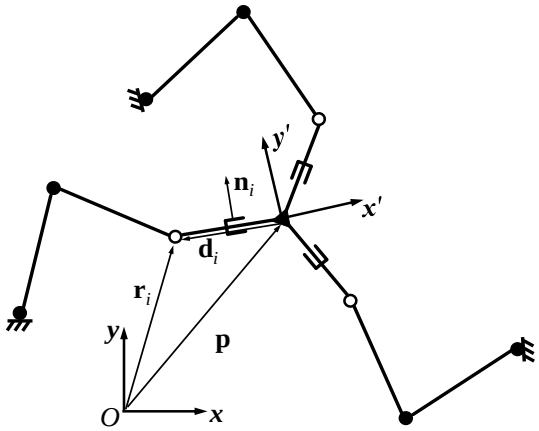

Figure 2.4 – Kinematic modelling of the 3-RRRP planar KRHPR with platform assembly arrangement (c) of Figure 2.1.

$\mathbf{n}_i$ which is expressed in the platform frame. This can be written as

$$\mathbf{d}_i^T(\mathbf{Q}\mathbf{n}_i) = 0. \tag{2.8}$$

Vector $\mathbf{d}_i$ in the platform assembly arrangement (b) can be written as

$$\mathbf{d}_i = \mathbf{r}_i + \mathbf{a}_i - \mathbf{p} - \mathbf{Q}\mathbf{b}_i \tag{2.9}$$

in which $\mathbf{a}_i = l\mathbf{Q}\mathbf{n}_i$ and $\mathbf{b}_i$ is a constant vector pointing from the origin of the platform frame to an arbitrary point on the axis of the ith prismatic joint, expressed in the platform frame. Differentiating (2.8) with respect to time and conducting a derivation similar to the one presented above for the 3-RRRR architecture, one can obtain the following Jacobian matrices

$$\mathbf{J} = \begin{bmatrix} \mathbf{n}_1^T\mathbf{Q}^T & c_1 \\ \mathbf{n}_2^T\mathbf{Q}^T & c_2 \\ \mathbf{n}_3^T\mathbf{Q}^T & c_3 \end{bmatrix} \tag{2.10}$$

$$\mathbf{K} = \begin{bmatrix} \mathbf{n}_1^T\mathbf{Q}^T\mathbf{M}_1 & \mathbf{0} & \mathbf{0} \\ \mathbf{0} & \mathbf{n}_2^T\mathbf{Q}^T\mathbf{M}_2 & \mathbf{0} \\ \mathbf{0} & \mathbf{0} & \mathbf{n}_3^T\mathbf{Q}^T\mathbf{M}_3 \end{bmatrix} \tag{2.11}$$

in which the scalars $c_i, i = 1, 2, 3$ are

$$c_i = \mathbf{n}_i^T\mathbf{Q}^T(\mathbf{E}\mathbf{Q}\mathbf{b}_i - \mathbf{E}^T\mathbf{d}_i). \tag{2.12}$$

It can be easily observed that each Plücker line in $\mathbf{J}$ passes through the passive revolute and prismatic joints and is perpendicular to the prismatic joint axis in the associated leg. For the platform assembly arrangement (c), the vector $\mathbf{d}_i$ is written as

$$\mathbf{d}_i = \mathbf{r}_i - \mathbf{p}. \tag{2.13}$$

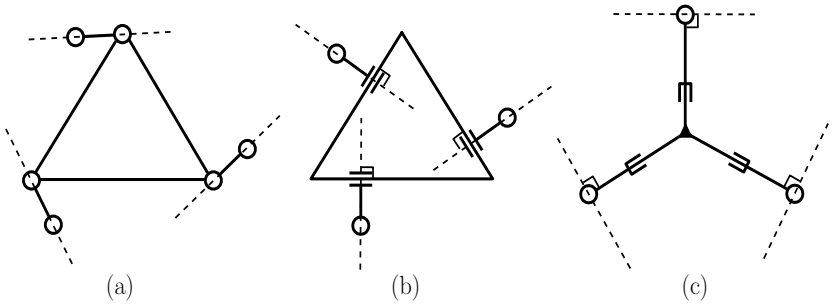

Figure 2.5 – Three Plücker lines in each platform assembly arrangement.

In this case the Jacobian matrices $\mathbf{J}$ and $\mathbf{K}$ have the same forms as (2.10) and (2.11) except that $c_i, i = 1, 2, 3$ become

$$c_i = -\mathbf{n}_i^T \mathbf{Q}^T \mathbf{E}^T \mathbf{d}_i \tag{2.14}$$

and the Plücker lines in $\mathbf{J}$ have the same properties as those in assembly arrangement (b).

2.2.2 Singularity Analysis of Architectures with Three Identical RR Sub-Legs

The Plücker lines for each platform assembly arrangement are illustrated in Fig. 2.5 by dashed lines. A type II singularity occurs whenever the three Plücker lines intersect at one common point (may happen in assembly arrangements (a) and (b)) or are parallel to each other (may happen only in assembly arrangement (a)). Such singularities for assembly arrangement (c) are automatically avoided due to mechanical limits. For the other assembly arrangements, type II singularities are also readily avoided. Since the sub-legs are fully actuated, it is possible to control the geometric relationship between each redundant link and the moving platform independently during motions, to ensure that the robot is never in a type II singular configuration. For instance, a simple approach is to predetermine a non-singular geometric relationship between the redundant links and the moving platform and maintain it unchanged. Moreover, if the legs of the proposed planar KRHPR are stacked in different planes parallel to each other, theoretically, the rotational workspace could be unlimited, whereas the rotational workspace of the 3-RRR non-redundant counterpart would mostly still be limited by type II singularities, which can be visualized by determining the type II singularity loci (Bonev and Gosselin, 2001).

Additionally, the type I singularities, corresponding to $\det(\mathbf{M}_i) = 0$, can be easily determined since they occur simply when the ith RR sub-leg is fully expanded or folded.

2.2.3 Other Feasible Planar Sub-Legs

A feasible sub-leg could be a serial, parallel, or redundant planar robot which has at least two translational degrees of freedom. For each platform assembly arrangement, using dif-

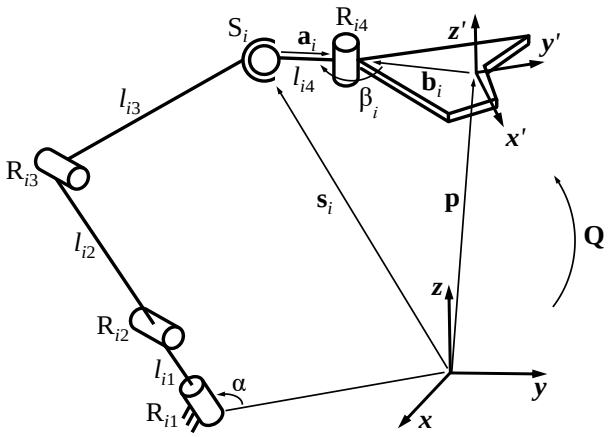

Figure 2.6 – Kinematic modelling of one leg of the 3-RRRSR spatial KRHPR.

ferent forms of sub-legs only changes the Jacobian matrix $\mathbf{M}_i$. Thereby, type II singularity conditions are preserved. Most planar mechanisms have very simple structures, thus we omit the kinematic analysis. Special attention should be paid to the planar parallel mechanisms because they may encounter both type I and type II singularities. However, the singular configurations can be revealed easily via screw theory (Bonev et al., 2003) or Grassmann-Cayley algebra (Wen et al., 2017).

2.3 Spatial Architectures with RRR Sub-Legs

2.3.1 Velocity Equations

In each leg of the spatial 3-RRRSR KRHPR (see Fig. 2.6), the axes of joints R_{i2} and R_{i3}, $(i = 1, 2, 3)$ are parallel to each other and perpendicular to the axis of joint R_{i1}. Parameters $l_{ij} (j = 1, 2, 3, 4)$ denote the length of the jth link in the ith leg and S_i represents the passive spherical joint of leg i.

The velocity equations of this KRHPR is similar to the variant of this architecture presented in Chapter 1. The Jacobians $\mathbf{J}$ and $\mathbf{K}$ can be written in the same form of (1.31) and (1.32), except that the Jacobian of the ith RRR linkage, which is $\mathbf{M}_i$, in matrix $\mathbf{K}$ will be

$$\mathbf{M}_i = [\mathbf{e}_{i1} \times \mathbf{r}_{i1} \quad \mathbf{e}_{i2} \times \mathbf{r}_{i2} \quad \mathbf{e}_{i3} \times \mathbf{r}_{i3}], \tag{2.15}$$

in which the unit vector $\mathbf{e}_{ik}, k = 1, 2, 3$ represents the direction of the axis of the kth actuated joint and $\mathbf{r}_{ik}$ is a position vector pointing from the centre of this actuated joint to the centre of joint S_i. All these quantities are expressed in the base frame.

The derivations of the velocity equations for the 3-RRRSP KRHPRs with both platform assembly arrangements (b) and (c) (see Figs. 2.7 and 2.8) are simpler than that of the 3-RRRSR

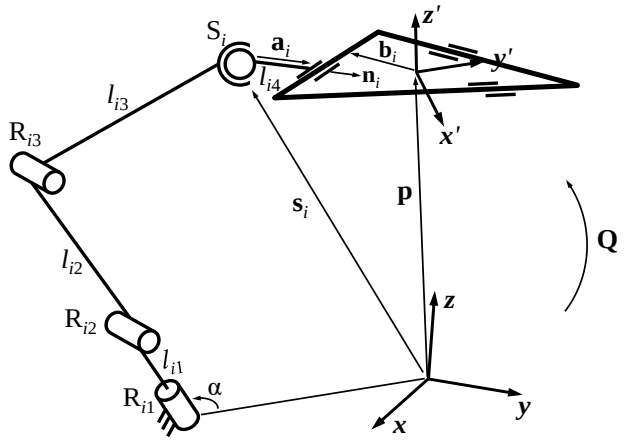

Figure 2.7 – Kinematic modelling of one leg of the 3-RRRSP spatial KRHPR with platform assembly arrangement (b).

architecture (although the detailed derivation is not provided here). For the architecture schematically shown in Fig. 2.7, it can be observed that a vector along the axis of the ith passive prismatic joint is always perpendicular to a plane formed by two mutually perpendicular vectors $\mathbf{Qn}_i$ and $\mathbf{q}_z$, which can be written mathematically as

$$\mathbf{d}_i^T(\mathbf{Qn}_i) = 0 \tag{2.16}$$

$$\mathbf{d}_i^T\mathbf{q}_z = 0, \quad i = 1, 2, 3 \tag{2.17}$$

where

$$\mathbf{d}_i = \mathbf{s}_i + \mathbf{a}_i - \mathbf{p} - \mathbf{Qb}_i \tag{2.18}$$

with $\mathbf{a}_i = l_{i4}\mathbf{Qn}_i$. Also, $\mathbf{b}_i$ is a constant vector pointing from the origin of the platform frame to an arbitrary point on the axis of ith prismatic joint, $\mathbf{n}_i$ is a constant unit vector on the platform plane which is perpendicular to the ith prismatic joint and expressed in the platform frame, and $\mathbf{q}_z$ is a unit vector along the z'-axis and is expressed in the base frame, as it has been defined in (1.20). If vector $\mathbf{b}_i$ is chosen to be parallel to vector $\mathbf{n}_i$, (2.16) can be further simplified to

$$(\mathbf{s}_i - \mathbf{p})^T(\mathbf{Qn}_i) = b - l_{i4} \tag{2.19}$$

where the constant scalars b and l_{i4} are obtained from

$$b = (\mathbf{Qb}_i)^T(\mathbf{Qn}_i), \quad l_{i4} = \mathbf{a}_i^T(\mathbf{Qn}_i). \tag{2.20}$$

On the other hand, since vector $\mathbf{q}_z$ is always perpendicular to vectors $\mathbf{a}_i$ and $\mathbf{Qb}_i$, (2.17) can be rewritten as

$$(\mathbf{s}_i - \mathbf{p})^T\mathbf{q}_z = 0. \tag{2.21}$$

The time derivative of (2.19) gives

$$(\mathbf{Qn}_i)^T\dot{\mathbf{p}} - (\mathbf{s}_i - \mathbf{p})^T(\dot{\mathbf{Q}}\mathbf{n}_i) = (\mathbf{Qn}_i)^T\dot{\mathbf{s}}_i. \tag{2.22}$$

Since

$$\begin{aligned}(\mathbf{s}_i - \mathbf{p})^T(\dot{\mathbf{Q}}\mathbf{n}_i) &= (\mathbf{s}_i - \mathbf{p})^T(\boldsymbol{\Omega}\mathbf{Q}\mathbf{n}_i) \\ &= (\mathbf{s}_i - \mathbf{p})^T[\boldsymbol{\omega} \times (\mathbf{Q}\mathbf{n}_i)] \\ &= [(\mathbf{Q}\mathbf{n}_i) \times (\mathbf{s}_i - \mathbf{p})]^T\boldsymbol{\omega} \end{aligned} \tag{2.23}$$

and $\dot{\mathbf{s}}_i = \mathbf{M}_i\dot{\boldsymbol{\theta}}_i$ with $\dot{\boldsymbol{\theta}}_i = [\dot{\theta}_{i1}\ \dot{\theta}_{i2}\ \dot{\theta}_{i3}]^T$ (the vector of actuated joint velocities of the ith leg), equation (2.22) can be rewritten as

$$(\mathbf{Q}\mathbf{n}_i)^T\dot{\mathbf{p}} + [(\mathbf{s}_i - \mathbf{p}) \times (\mathbf{Q}\mathbf{n}_i)]^T\boldsymbol{\omega} = (\mathbf{Q}\mathbf{n}_i)^T\mathbf{M}_i\dot{\boldsymbol{\theta}}_i. \tag{2.24}$$

Similarly, the time derivative of (2.21) yields

$$\mathbf{q}_z^T\dot{\mathbf{p}} - (\mathbf{s}_i - \mathbf{p})^T\dot{\mathbf{q}}_z = \mathbf{q}_z^T\dot{\mathbf{s}}_i, \tag{2.25}$$

here

$$(\mathbf{s}_i - \mathbf{p})^T\dot{\mathbf{q}}_z = (\mathbf{s}_i - \mathbf{p})^T(\boldsymbol{\omega} \times \mathbf{q}_z) = [\mathbf{q}_z \times (\mathbf{s}_i - \mathbf{p})]^T\boldsymbol{\omega}, \tag{2.26}$$

thus (2.25) can be rewritten as

$$\mathbf{q}_z^T\dot{\mathbf{p}} + [(\mathbf{s}_i - \mathbf{p}) \times \mathbf{q}_z]^T\boldsymbol{\omega} = \mathbf{q}_z^T\mathbf{M}_i\dot{\boldsymbol{\theta}}_i. \tag{2.27}$$

The Jacobian matrices can be obtained by combining the corresponding terms in (2.24) and (2.27), yielding

$$\mathbf{J} = \begin{bmatrix} \mathbf{n}_1^T\mathbf{Q}^T & [(\mathbf{s}_1 - \mathbf{p}) \times (\mathbf{Q}\mathbf{n}_1)]^T \\ \mathbf{q}_z^T & [(\mathbf{s}_1 - \mathbf{p}) \times \mathbf{q}_z]^T \\ \mathbf{n}_2^T\mathbf{Q}^T & [(\mathbf{s}_2 - \mathbf{p}) \times (\mathbf{Q}\mathbf{n}_2)]^T \\ \mathbf{q}_z^T & [(\mathbf{s}_2 - \mathbf{p}) \times \mathbf{q}_z]^T \\ \mathbf{n}_3^T\mathbf{Q}^T & [(\mathbf{s}_3 - \mathbf{p}) \times (\mathbf{Q}\mathbf{n}_3)]^T \\ \mathbf{q}_z^T & [(\mathbf{s}_3 - \mathbf{p}) \times \mathbf{q}_z]^T \end{bmatrix} \tag{2.28}$$

and

$$\mathbf{K} = \begin{bmatrix} \mathbf{n}_1^T\mathbf{Q}^T\mathbf{M}_1 & \mathbf{0} & \mathbf{0} \\ \mathbf{q}_z^T\mathbf{M}_1 & \mathbf{0} & \mathbf{0} \\ \mathbf{0} & \mathbf{n}_2^T\mathbf{Q}^T\mathbf{M}_2 & \mathbf{0} \\ \mathbf{0} & \mathbf{q}_z^T\mathbf{M}_2 & \mathbf{0} \\ \mathbf{0} & \mathbf{0} & \mathbf{n}_3^T\mathbf{Q}^T\mathbf{M}_3 \\ \mathbf{0} & \mathbf{0} & \mathbf{q}_z^T\mathbf{M}_3 \end{bmatrix}. \tag{2.29}$$

The constraint conditions of the architecture illustrated in Fig. 2.8 can be described similarly to those of the above discussed 3-RRRSP KRHPR. Thus, one can write the constraint equations as follows

$$(\mathbf{s}_i - \mathbf{p})^T(\mathbf{Q}\mathbf{n}_i) = 0 \tag{2.30}$$

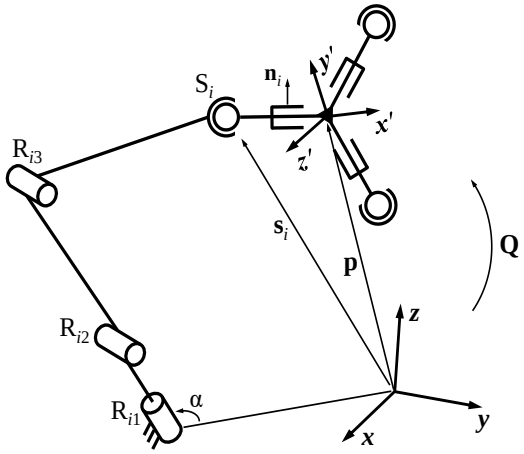

Figure 2.8 – Kinematic modelling of one leg of the 3-RRRSP spatial KRHPR with platform assembly arrangement (c).

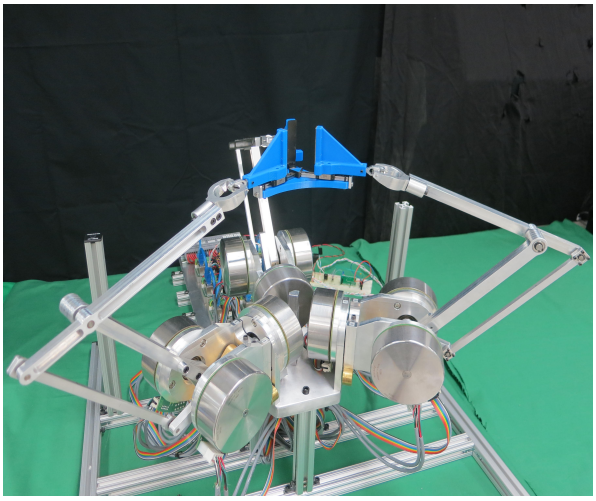

Figure 2.9 – Prototype of the 3-[R(RR-RRR)SP] robot. The gripper on the moving platform has three jaws where each of them can move along the corresponding passive prismatic joint.

$$(\mathbf{s}_i - \mathbf{p})^T \mathbf{q}_z = 0. \tag{2.31}$$

Clearly, one obtains the Jacobian matrices $\mathbf{J}$ and $\mathbf{K}$ with the same forms as (2.28) and (2.29) after differentiating the above equations with respect to time. A prototype of the variant of the 3-RRRSP spatial KRHPR with platform assembly arrangement (c), namely the 3-[R(RR-RRR)SP] spatial KRHPR, is shown in Fig. 2.9. The Jacobians of the prototype can be written in the similar forms of those of (2.28) and (2.29), in which $\mathbf{M}_i$ (with $i = 1, 2, 3$) is defined in (1.16).

2.3.2 Singularity Analysis

The type I singularity conditions of the proposed spatial KRHPRs are similar to those of the architecture studied in Chapter 1 and thus such singularities are easily alleviated. The

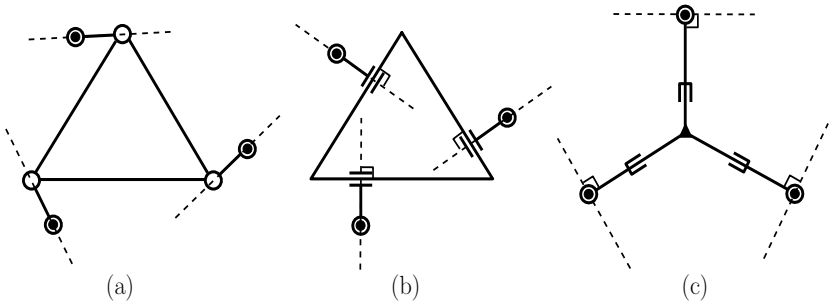

Figure 2.10 – Six Plücker lines in each platform assembly arrangement.

complexity of type II singularity conditions is significantly reduced thanks to the types of redundant links as well as the platform assembly arrangements. Each row of Jacobian $\mathbf{J}$ represents a spatial Plücker line. For a spherical-revolute redundant link, as analysed in Chapter 1, one Plücker line lies on the platform plane and passes through both joints, the other one is parallel to vector $\mathbf{q}_z$. For a spherical-prismatic redundant link, one line passes through both joints and is perpendicular to the prismatic joint and the other one is parallel to vector $\mathbf{q}_z$. In each case, two lines intersect at the centre of the spherical joint. As described in Fig. 2.10, the dashed lines represent the coplanar Plücker lines; while the spatial parallel Plücker lines (orthogonal to the paper) are indicated by small solid circles. These two groups of lines belong to two orthogonal vector spaces. Each line in one vector space is linearly independent (in fact orthogonal) from those in the other vector space. Therefore, matrix $\mathbf{J}$ becomes singular only when the lines in one of the two vector spaces become linearly dependent.

Nevertheless, all type II singularities can either be avoided or eliminated. Three cases should be taken into consideration, namely (*i*) three spatial parallel Plücker lines become coplanar parallel, (*ii*) three coplanar Plücker lines become parallel or (*iii*) intersect at a common point. The platform assembly arrangement (a) may be subjected to all these cases, while the platform assembly arrangement (b) is only subjected to the last one. These singularities are readily avoided using the technique proposed for the planar KRHPRs. Moreover, similarly to the planar case, it can be inferred that the platform assembly arrangement (c) is completely free from type II singularities.

2.4 Examples of Other Sub-Legs for Spatial KRHPRs

Similarly to the planar case, the velocity equations of a novel KRHPR synthesized using the following sub-legs are obtained simply by replacing the sub-leg Jacobians $\mathbf{M}_i$ in matrix $\mathbf{K}$ by that of the new sub-leg.

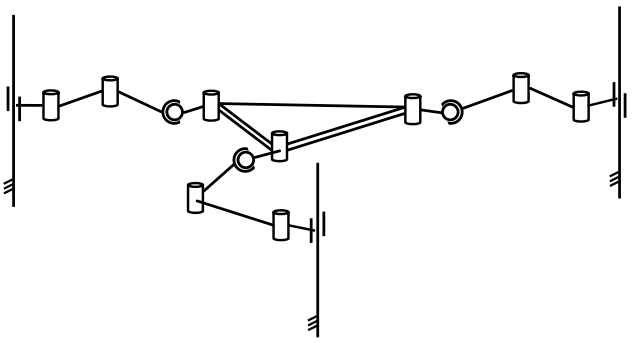

Figure 2.11 – The 3-PRRSR architecture with parallel axes of the actuated joints.

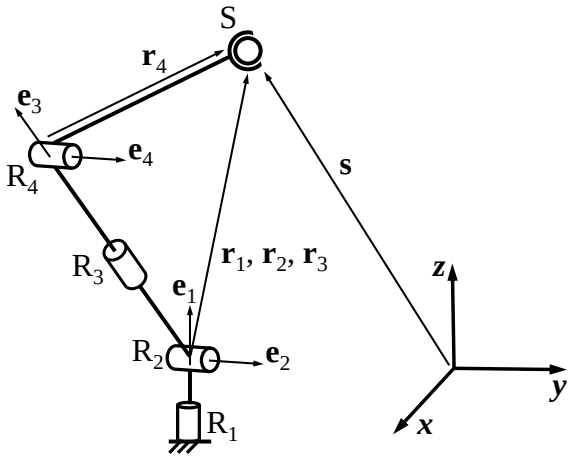

Figure 2.12 – The 4R sub-leg.

2.4.1 Serial Sub-Legs: PRR and 4R Linkages

A simple way to avoid the shoulder singularity of the RRR linkage is to replace the first revolute joint by an actuated prismatic (P) one whose axis is parallel to those of the following joints. The Jacobian matrix of this PRR sub-leg is obtained simply by changing the first column of the matrix in (2.15) by the direction vector of the prismatic joint.

Additionally, it is interesting to note that if three PRR sub-legs are assembled with the axes of all actuated joints in parallel, the translational workspace of the robot can be, theoretically, unlimited in the direction of the actuated joints axes. Such an architecture is represented schematically in Fig. 2.11.

The 4R sub-leg can be regarded as an alternative to the PRR sub-leg, since it also has the ability to avoid shoulder singularity (Hollerbach, 1985). This linkage (see Fig. 2.12) is obtained by adding an actuated revolute joint between the two parallel revolute joints in the RRR sub-

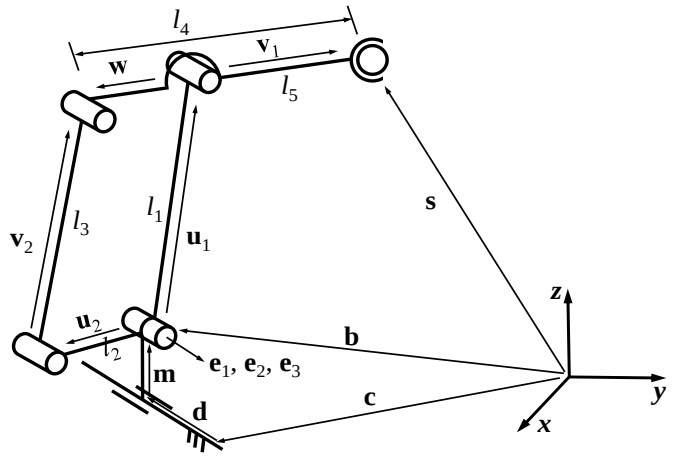

Figure 2.13 – The P(RR-RRR) linkage.

leg. The Jacobian matrix can be written as

$$\mathbf{M} = [\mathbf{e}_1 \times \mathbf{r}_1 \quad \mathbf{e}_2 \times \mathbf{r}_2 \quad \mathbf{e}_3 \times \mathbf{r}_3 \quad \mathbf{e}_4 \times \mathbf{r}_4] \tag{2.32}$$

where $\mathbf{e}_i$ and $\mathbf{r}_i, i = 1, 2, 3, 4$ are respectively the direction vector of the ith revolute joint and the position vector from the centre of the ith revolute joint to the end-point.

2.4.2 Hybrid Sub-Leg: P(RR-RRR) Linkage

In this linkage (see Fig. 2.13), the axis of the prismatic joint is parallel to those of the revolute joints. Three constraint equations can be written as

$$\mathbf{e}_1^T(\mathbf{s} - \mathbf{b}) = 0 \tag{2.33}$$

$$(\mathbf{s} - \mathbf{b} - \mathbf{u}_1)^T(\mathbf{s} - \mathbf{b} - \mathbf{u}_1) = \mathbf{v}_1^T\mathbf{v}_1 = l_5^2 \tag{2.34}$$

$$(\mathbf{u}_1 + \mathbf{w} - \mathbf{u}_2)^T(\mathbf{u}_1 + \mathbf{w} - \mathbf{u}_2) = \mathbf{v}_2^T\mathbf{v}_2 = l_3^2 \tag{2.35}$$

where

$$\mathbf{b} = \mathbf{c} + \mathbf{d} + \mathbf{m} \tag{2.36}$$

in which vector $\mathbf{c}$ is pointing from the origin of the base frame to an arbitrary point on the axis of the prismatic joint, vector $\mathbf{d}$ is pointing from the end point of vector $\mathbf{c}$ to the centre of the prismatic joint, and vector $\mathbf{m}$ is along the link between the prismatic joint and the following two revolute joints, both $\mathbf{c}$ and $\mathbf{m}$ are constant vectors.

Since $\mathbf{e}_1$ is a constant unit vector and we can express the vector $\mathbf{d}$ as $\mathbf{d} = d\mathbf{e}_1$, the time derivative of (2.33) can be written as

$$\mathbf{e}_1^T\dot{\mathbf{s}} = \dot{d}. \tag{2.37}$$

Equation (2.34) can be rewritten as

$$(\mathbf{s} - \mathbf{b})^T(\mathbf{s} - \mathbf{b}) - 2(\mathbf{s} - \mathbf{b})^T\mathbf{u}_1 = l_5^2 - l_1^2 \tag{2.38}$$

in which $l_1^2 = \mathbf{u}_1^T \mathbf{u}_1$. The time derivative of the above equation yields

$$(\mathbf{s} - \mathbf{b})^T(\dot{\mathbf{s}} - \dot{\mathbf{d}}) - \mathbf{u}_1^T(\dot{\mathbf{s}} - \dot{\mathbf{d}}) - (\mathbf{s} - \mathbf{b})^T \dot{\mathbf{u}}_1 = 0. \tag{2.39}$$

After rearranging the terms, one can obtain

$$(\mathbf{s} - \mathbf{b} - \mathbf{u}_1)^T \dot{\mathbf{s}} = (\mathbf{s} - \mathbf{b} - \mathbf{u}_1)^T \dot{\mathbf{d}} + (\mathbf{s} - \mathbf{b})^T \dot{\mathbf{u}}_1 \tag{2.40}$$

which yields

$$\mathbf{v}_1^T \dot{\mathbf{s}} = \dot{\theta}_2 (\mathbf{s} - \mathbf{b})^T (\mathbf{e}_2 \times \mathbf{u}_1) \tag{2.41}$$

with

$$\dot{\mathbf{u}}_1 = \dot{\theta}_2 \mathbf{e}_2 \times \mathbf{u}_1 \tag{2.42}$$

where $\dot{\theta}_2$ is the angular velocity of the first actuated revolute joint. The first term on the right hand side of (2.40) vanishes because $\mathbf{v}_1^T \dot{\mathbf{d}} = \dot{d} \mathbf{v}_1^T \mathbf{e}_1 = 0$.

The time derivative of (2.35) leads to

$$\mathbf{v}_2^T [\dot{\mathbf{u}}_1 + (1 - \frac{l_4}{l_5})(\dot{\mathbf{s}} - \dot{\mathbf{d}} - \dot{\mathbf{u}}_1) - \dot{\mathbf{u}}_2] = 0 \tag{2.43}$$

with

$$\dot{\mathbf{w}} = (1 - \frac{l_4}{l_5}) \dot{\mathbf{v}}_1 = (1 - \frac{l_4}{l_5})(\dot{\mathbf{s}} - \dot{\mathbf{d}} - \dot{\mathbf{u}}_1). \tag{2.44}$$

Considering that $\mathbf{v}_2^T \dot{\mathbf{d}} = \dot{d} \mathbf{v}_2^T \mathbf{e}_1 = 0$, then one can obtain the following velocity equation after rearranging the terms in (2.43)

$$(1 - \frac{l_4}{l_5}) \mathbf{v}_2^T \dot{\mathbf{s}} = \frac{l_4}{l_5} \dot{\theta}_2 \mathbf{v}_2^T (\mathbf{u}_1 \times \mathbf{e}_2) + \dot{\theta}_3 \mathbf{v}_2^T (\mathbf{e}_3 \times \mathbf{u}_2) \tag{2.45}$$

with

$$\dot{\mathbf{u}}_2 = \dot{\theta}_3 \mathbf{e}_3 \times \mathbf{u}_2 \tag{2.46}$$

where $\dot{\theta}_3$ is the angular velocity of the second actuated revolute joint.

Combining (2.37), (2.41) and (2.45), one obtains the following velocity equations

$$\mathbf{J} \dot{\mathbf{s}} = \mathbf{K} \dot{\boldsymbol{\theta}} \tag{2.47}$$

where $\dot{\boldsymbol{\theta}} = [\dot{d} \ \dot{\theta}_2 \ \dot{\theta}_3]^T$ and the Jacobian matrices $\mathbf{J}$ and $\mathbf{K}$ are

$$\mathbf{J} = \begin{bmatrix} \mathbf{e}_1^T \\ \mathbf{v}_1^T \\ (1 - \frac{l_4}{l_5}) \mathbf{v}_2^T \end{bmatrix} \tag{2.48}$$

and

$$\mathbf{K} = \begin{bmatrix} 1 & 0 & 0 \\ 0 & (\mathbf{s} - \mathbf{b})^T (\mathbf{e}_2 \times \mathbf{u}_1) & 0 \\ 0 & \frac{l_4}{l_5} \mathbf{v}_2^T (\mathbf{u}_1 \times \mathbf{e}_2) & \mathbf{v}_2^T (\mathbf{e}_3 \times \mathbf{u}_2) \end{bmatrix}. \tag{2.49}$$

Note that matrix $\mathbf{K}$ could be diagonal if the closed loop in the linkage is designed to be a parallelogram. Finally, the combined Jacobian is written as

$$\mathbf{M} = \mathbf{J}^{-1}\mathbf{K}. \tag{2.50}$$

Clearly, Jacobian $\mathbf{J}$ becomes singular only when vectors $\mathbf{v}_1$ and $\mathbf{v}_2$ are collinear and Jacobian $\mathbf{K}$ is singular if vectors $\mathbf{v}_1$ and $\mathbf{u}_1$, or $\mathbf{v}_2$ and $\mathbf{u}_2$, become collinear.

2.4.3 Parallel Sub-Leg: 3-CPR Mechanism

In each leg of the 3-CPR mechanism (see Fig. 2.14), the axis of the cylindrical joint (C) is parallel to the axis of the revolute joint, the axis of the prismatic joint is orthogonal to those of the other joints. This mechanism has three translational degrees of freedom and the constraint characteristics have been studied in (Zhao et al., 2002).

The constraint equation on the length of the actuators is written as

$$\mathbf{p}_i^T \mathbf{p}_i = \rho_i^2, \quad i = 1, 2, 3 \tag{2.51}$$

where vector $\mathbf{p}_i$ is written as

$$\mathbf{p}_i = \mathbf{s} + \mathbf{v}_i - \mathbf{c}_i - \mathbf{w}_i, \quad i = 1, 2, 3 \tag{2.52}$$

in which vector $\mathbf{c}_i$ is pointing from the origin of the base frame to an arbitrary point on the axis of the ith cylindrical joint and $\mathbf{w}_i$ is along the axis of the same cylindrical joint. Since $\mathbf{v}_i$ and $\mathbf{c}_i$ are constant vectors as well as $\mathbf{p}_i^T \dot{\mathbf{w}}_i = 0$, the time derivative of (2.51) yields

$$\mathbf{p}_i^T \dot{\mathbf{s}} = \rho_i \dot{\rho}_i, \quad i = 1, 2, 3. \tag{2.53}$$

The velocity equations can then be written as

$$\mathbf{J}\dot{\mathbf{s}} = \mathbf{K}\dot{\boldsymbol{\rho}} \tag{2.54}$$

with $\dot{\boldsymbol{\rho}} = [\dot{\rho}_1 \quad \dot{\rho}_2 \quad \dot{\rho}_3]^T$ and the Jacobians $\mathbf{J}$ and $\mathbf{K}$ are respectively

$$\mathbf{J} = \begin{bmatrix} \mathbf{p}_1^T \\ \mathbf{p}_2^T \\ \mathbf{p}_3^T \end{bmatrix}, \quad \mathbf{K} = \begin{bmatrix} \rho_1 & 0 & 0 \\ 0 & \rho_2 & 0 \\ 0 & 0 & \rho_3 \end{bmatrix}. \tag{2.55}$$

It can be seen that as long as vectors $\mathbf{p}_i, i = 1, 2, 3$ in the mechanism are not coaxial or coplanar, Jacobian $\mathbf{J}$ will not be singular.

2.4.4 Other Feasible Sub-Legs

Any mechanism that can endow three translational degrees of freedom at the spherical joint which is connected to the redundant link is a potential candidate. Examples of parallel mechanisms are: the 3-UPS (Gosselin and Schreiber, 2018), 3-UPU (Huang and Li, 2002) and

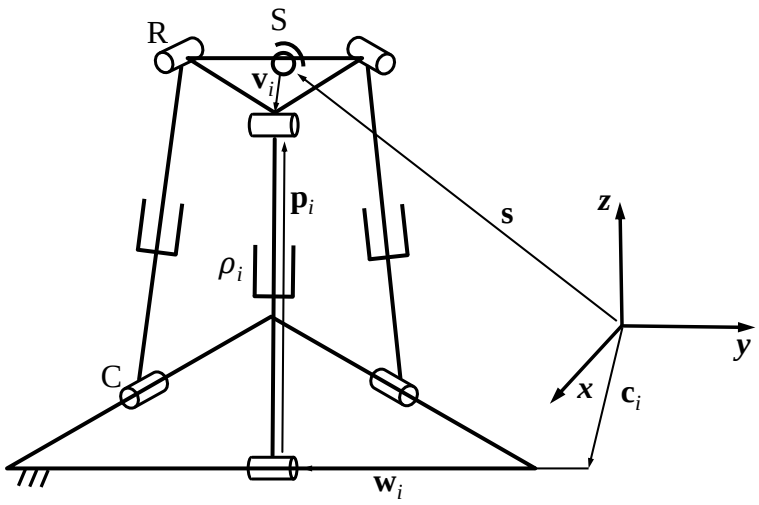

Figure 2.14 – The 3-CPR mechanism.

the Tripteron (Gosselin et al., 2004) robots, which are actuated by prismatic joints, or the Delta Robot (Clavel, 1990; Bonev, 2001), which is actuated using revolute joints. Moreover, methodologies proposed in (Kong and Gosselin, 2004a,b,c,d; Huang et al., 2006; Kong et al., 2006; Kong and Gosselin, 2007) greatly facilitate the synthesis of parallel mechanisms, as they cannot be obtained intuitively in most cases. However, one should avoid to use a parallel mechanism with complex singularity conditions.

2.5 Inverse Kinematics Analysis

For the proposed KRHPRs, an analytical inverse kinematic solution at the displacement level which is computationally efficient and conservative can be obtained in a similar manner as that studied in Chapter 1. If the angles $\beta_i, i = 1, 2, 3$ (see Figs. 2.2 and 2.6) or the displacements of the prismatic joints in the redundant links (see Figs. 2.3, 2.4, 2.7 and 2.8) are predetermined, as mentioned, it is possible to maintain the platform in favorable configurations which keep it away from type II singularities, as well as passive joint limits and mechanical interferences. By doing so, given the orientation matrix of the platform, the vector pointing from the origin of the platform frame to the passive joint which connects the sub-leg to the redundant link in the ith leg can be readily computed. The sum of this vector and the position vector of the platform frame result in vector $\mathbf{r}_i$ (in planar KRHPRs) or $\mathbf{s}_i$ (in spatial KRHPRs), which is the end-point of the ith planar or spatial sub-leg. At last, an analytical inverse kinematic solution of a KRHPR is solved by solving the inverse kinematic problem of every sub-leg.

Note that this method is valid only when the inverse kinematic problem of the sub-leg can be solved analytically. For the 4R linkage discussed above, an analytical solution has been developed in (Hollerbach, 1985). Besides, for the parallel sub-legs that have additional rotational

degrees of freedom, the orientation of the sub-legs should be pre-specified before solving the inverse kinematic problem.

2.6 Conclusion

By introducing two different types of redundant links and three different platform assembly arrangements, a class of three-legged planar and spatial KRHPRs are synthesized. The KRHPR can produce a better rotational behaviour than its non-redundant counterpart. But the improvement of the orientational workspace is at the expense of increased mass and inertia due to the redundant links and the additional actuators, which may reduce the dynamic performances of the KRHPR. However, this may not be a concern, since the proposed KRHPRs are mainly intended for applications with relatively low accelerations, such as pHRI. Moreover, it was shown that using several redundant legs yields advantages, namely: *i*) the type of the joints used in the sub-legs is not limited and the geometric design is less restrictive, *ii*) type II singular configurations can be determined and avoided easily in spite of the types of the actuated legs and, *iii*) in most instances, an analytical, consistent and conservative solution for the inverse kinematic problem of the composed KRHPRs can be obtained, which is a desirable property for a redundant robot.

Chapter 3

Forward Kinematic Analysis of Spatial KRHPRs with Spherical-Revolute Redundant Links

3.1 Introduction

In applications such as pHRI, the performance of a parallel robot is most likely limited due to the difficulty of acquiring a unique solution of the forward kinematics and the relatively small orientational workspace (because of the occurrence of type II (or parallel) singularities (Gosselin and Angeles, 1990)). The orientational workspace of a parallel robot can be enlarged by introducing kinematic redundancies to alleviate the type II singularities, as studied in the previous chapters. However, the complexity of the forward kinematics is not decreased in the presence of kinematic redundancy. Similarly to their non-redundant counterparts, different assembly modes of a kinematically redundant parallel robot may exist for given actuated joint variables.

For example, it is well known that, the forward kinematic problem of the Gough-Stewart platform can be described as a fortieth-degree univariate polynomial formulation (Husty, 1994). Researchers have proposed several different approaches for solving the forward kinematic problem, such as elimination (Husty, 1994; Innocenti, 2001; Lee and Shim, 2001), homotopy (Raghavan, 1993), Gröbner basis (Lazard, 1993), continuation (Wampler, 1996), and interval analysis (Merlet, 2004). A more comprehensive discussion on this topic can be found in (Merlet, 2006b). Nevertheless, because of the very nature of the structure of Gough-Stewart platforms, determining all the solutions (real or complex) is challenging. Furthermore, as mentioned in (Gosselin and Schreiber, 2016), the forward kinematic problem of a kinematically redundant Gough-Stewart platform is similar to that of its non-redundant counterpart.

In this chapter, we address the forward kinematic problem of a class of three-legged $(6+3)$-

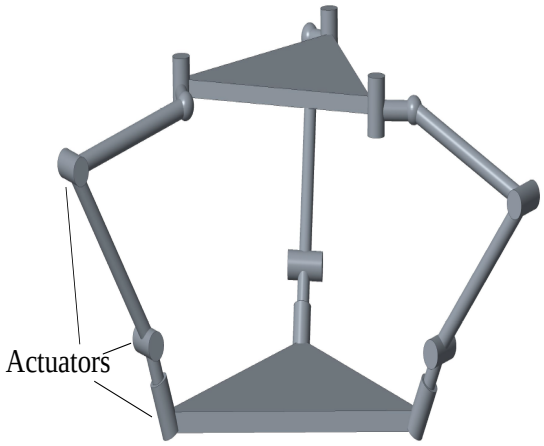

Figure 3.1 – The architecture of a 3-RRRSR kinematically redundant mechanism.

dof spatial KRHPRs with spherical-revolute redundant links proposed in Chapter 2. Different from the issue mentioned in the preceding paragraph, the forward kinematic problem of the KRHPR is much easier than that of its non-redundant counterpart and that of most other kinematically redundant parallel robots. As it will be seen in one of the approaches developed in Section 3.2, the maximum order of the univariate polynomial formulation of the forward kinematic problem is only six, which can be readily handled.

A possible approach to determine a unique forward kinematic solution is to exploit the Newton-Raphson method (Reboulet, 1985; Hesselbach and Kerle, 1995), which is also employed in this study. However, this method may encounter, though it is rare, the convergence problem. Another possible approach to obtain a forward kinematic solution is by introducing extra sensors to measure the passive joint coordinates (Parenti-Castelli and Di Gregorio, 1999; Bonev et al., 2001; Chiu and Perng, 2001). The minimum number of necessary extra encoders then becomes an issue. In this chapter, we show that generally the number of extra encoders that are needed to obtain a unique forward kinematic solution for the KRHPR is less than that for its non-redundant counterpart.

The rest of this chapter is organized as follows: in Section 3.2, seven different approaches for solving the forward kinematics with or without extra rotary encoders for a KRHPR with RRRSR legs are developed. Then, considering that the obtained orientation matrix of the platform may not be orthonormal in the presence of manufacturing and measurement errors, the Gram-Schmidt process is exploited to orthonormalize this matrix. In Section 3.4, a simulation is conducted to verify the effectiveness of these approaches. The forward kinematic problem of the R(RR-RRR) sub-leg of the 3-[R(RR-RRR)SR] architecture proposed in Chapter 1 is briefly studied in Section 3.5. Finally, conclusions are drawn.

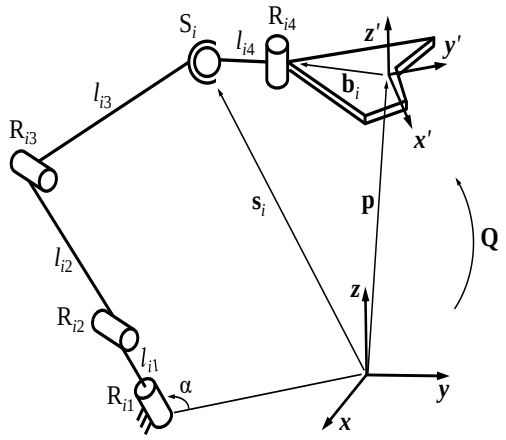

Figure 3.2 – Kinematic modelling of one leg of the 3-RRRSR mechanism.

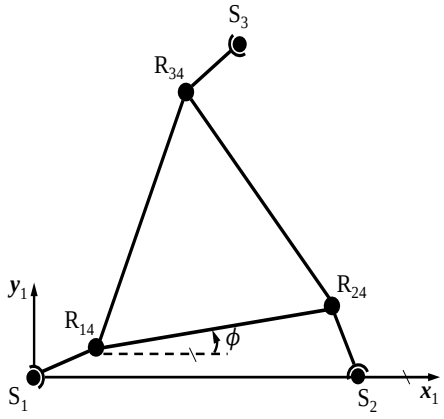

Figure 3.3 – The intermediate coordinate frame.

3.2 Forward Kinematic Analysis of a KRHPR with RRRSR Legs

We start the forward kinematic analysis of an architecture with relatively simple structure, namely: the 3-RRRSR KRHPR, as shown in Fig. 3.1. The kinematic modelling of one leg of the robot is shown in Fig. 3.2 which is the same as that illustrated in Fig. 2.6.

3.2.1 Approach One: Particular Method

It can be observed from Fig. 3.2 that vector $\mathbf{s}_i$ is readily obtained by solving the forward kinematics of the ith RRR sub-leg, and the solution can be uniquely determined. Then, as shown in Fig. 3.3, an intermediate frame $S_1x_1y_1z_1$ can be defined, in which the x_1-axis points from the centre of joint S_1 to that of joint S_2 and the y_1-axis lies on the plane of the platform.

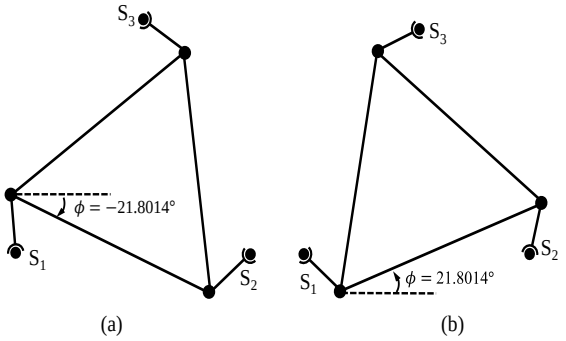

Figure 3.4 – Two different solutions obtained from approach one.

The direction cosines of x_1- and z_1-axes expressed in the base frame can be given as

$$\mathbf{x}_1 = \frac{\mathbf{s}_{12}}{||\mathbf{s}_{12}||} \tag{3.1}$$

$$\mathbf{z}_1 = \frac{\mathbf{s}_{12} \times \mathbf{s}_{13}}{||\mathbf{s}_{12} \times \mathbf{s}_{13}||} \tag{3.2}$$

where $||\cdot||$ denotes the Euclidean norm of a vector and $\mathbf{s}_{1j} = \mathbf{s}_j - \mathbf{s}_1,\ j = 2, 3$. Since the magnitude of l_{i4} is designed to be smaller than one half of the circumradius of the platform, the vectors $\mathbf{s}_{12}$ and $\mathbf{s}_{13}$ cannot be collinear and their norms can never be 0. The expression of the y_1-axis is obtained easily by the right-hand rule. The orientation matrix of the intermediate frame expressed in the base frame can then be determined as

$${}^{B}_{I}\mathbf{Q} = [\mathbf{x}_1\ \mathbf{y}_1\ \mathbf{z}_1]. \tag{3.3}$$

Once ${}^{B}_{I}\mathbf{Q}$ is obtained, the rest of the forward kinematic problem for the proposed robot is similar to that of the planar 3-R$\underline{\text{P}}$R (or 3-$\underline{\text{R}}$RR) parallel manipulators (Gosselin et al., 1992), i.e., it consists in identifying the possible poses of the platform with respect to the intermediate frame.

By implementing the approach proposed in (Gosselin et al., 1992), a sixth-degree polynomial equation with the unknown ϕ (see Fig. 3.3) can be established, a maximum of six different real solutions can then be obtained. For example, when the coordinates of the centre of the joints $\text{S}_i, i = 1, 2, 3$, expressed in the intermediate frame $\text{S}_1x_1y_1z_1$, are respectively $[0\ 0\ 0]^T$, $[233.1845\ 0\ 0]^T$, $[116.5923\ 201.9437\ 0]^T$ with units in mm, only two ($\phi = \pm 21.8014°$) of the six solutions are real. The poses of the moving platform corresponding to these two real solutions are schematically illustrated in Fig. 3.4.

By contrast, the forward kinematic problem of the non-redundant counterpart of the 3-$\underline{\text{RRR}}$SR KRHPR proposed in (Monsarrat and Gosselin, 2001), namely: the 3-[R($\underline{\text{RR}}$-$\underline{\text{R}}$RR)S] parallel robot, is not equivalent to that of any planar parallel robot. Therefore, the order of the polynomial formulation describing the forward kinematic problem is much higher. Moreover,

it can be seen that although the same type of redundant link is exploited in the $(6+3)$-dof spatial kinematically redundant parallel robot proposed in (Gosselin and Schreiber, 2016), it is impossible to implement the particular method discussed above to solve the forward kinematic problem. This is because in the architecture proposed in (Gosselin and Schreiber, 2016), instead of the revolute joint, the spherical joint of the redundant link is attached to the moving platform, and hence the moving platform and all of the redundant links are not coplanar.

3.2.2 Approach Two: Newton-Raphson Method

Although it is possible to obtain all the possible postures of the platform by utilizing the previous approach, in practical applications, a unique solution is desired. The Newton-Raphson method can be used for this purpose. Because the direction cosines of the z'-axis, denoted by $\mathbf{q}_z$, is the same as the vector $\mathbf{z}_1$ which is given in Eq. (3.2), the remaining unknown parameters are the direction cosines of the x'- and y'- axes, denoted, respectively, by $\mathbf{q}_x$ and $\mathbf{q}_y$, and the position vector $\mathbf{p}$, which contains in total nine variables. Thus, a system of nine constraint equations can be formed to implement the Newton-Raphson method.

As it can be observed from Fig. 3.2, a constraint equation on the squared length of each redundant link can be written as

$$(\mathbf{p}+\mathbf{Q}\mathbf{b}_i-\mathbf{s}_i)^T(\mathbf{p}+\mathbf{Q}\mathbf{b}_i-\mathbf{s}_i)-l_{i4}^2=0, \quad i=1,2,3 \tag{3.4}$$

in which $\mathbf{Q}=[\mathbf{q}_x\ \mathbf{q}_y\ \mathbf{q}_z]$. In addition, the vectors $(\mathbf{s}_1-\mathbf{p})$ and $\mathbf{q}_z$ are always orthogonal, thus

$$(\mathbf{s}_1-\mathbf{p})^T\mathbf{q}_z=0. \tag{3.5}$$

Finally, the rotation matrix must be orthogonal, namely

$$\mathbf{Q}^T\mathbf{Q}-\mathbf{I}=\mathbf{0} \tag{3.6}$$

where $\mathbf{I}$ is the 3×3 identity matrix. Equation (3.6) provides five constraint equations since $\mathbf{q}_z$ is obtained from the outset using Eq. (3.2), as explained above.

Combining Eqs. (3.4), (3.5) and (3.6) yields a system of nine equations in nine unknowns

$$\mathbf{F}(\mathbf{X})=\mathbf{0} \tag{3.7}$$

where $\mathbf{X}=[\mathbf{q}_x^T\ \mathbf{q}_y^T\ \mathbf{p}^T]^T$ and where most of the equations are nonlinear. The Newton-Raphson method at iteration k can be written as

$$\text{Solve} \quad \mathbf{F}'(\mathbf{X}^{(k)})\boldsymbol{\delta}^{(k)}=-\mathbf{F}(\mathbf{X}^{(k)}) \quad \text{for} \quad \boldsymbol{\delta}^{(k)} \tag{3.8}$$

$$\mathbf{X}^{(k+1)}=\mathbf{X}^{(k)}+\boldsymbol{\delta}^{(k)}, \quad k=0,1,\cdots \tag{3.9}$$

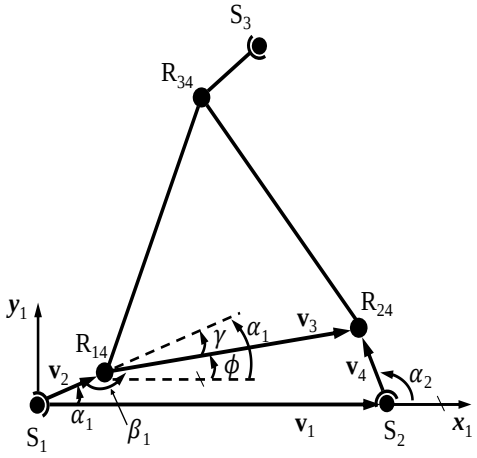

Figure 3.5 – One extra encoder at joint R_{14} associated with angle β_1.

where matrix $\mathbf{F}'(\mathbf{X})$ is the partial derivative of vector $\mathbf{F}(\mathbf{X})$ with respect to vector $\mathbf{X}$ and is of dimension 9×9.

The procedure stops when the equations are satisfied within a predetermined accuracy. With a proper initial guess (which is usually available in the continuous tracking of a trajectory), the procedure converges very quickly (typically less than 4 iterations are required).

3.2.3 Approach Three: Using One Extra Encoder

One possible way to avoid the use of a numerical method while limiting the number of possible solutions consists in adding extra encoders to the passive joints to acquire more information (Tancredi et al., 1995; Han et al., 1996). We start the analysis by adding an encoder to joint R_{14} to measure the magnitude of angle β_1. As shown in Fig. 3.5, the vectors $\mathbf{v}_i,\ i = 1, 2, 3, 4$, construct a planar 4-bar linkage whose vector loop equation expressed in the intermediate frame $S_1 x_1 y_1 z_1$ can be written as

$$\mathbf{v}_2 + \mathbf{v}_3 = \mathbf{v}_1 + \mathbf{v}_4. \tag{3.10}$$

Writing Eq. (3.10) in matrix form yields

$$\begin{bmatrix} v_2 \cos\alpha_1 \\ v_2 \sin\alpha_1 \end{bmatrix} + \begin{bmatrix} v_3 \cos\phi \\ v_3 \sin\phi \end{bmatrix} = \begin{bmatrix} v_1 \\ 0 \end{bmatrix} + \begin{bmatrix} v_4 \cos\alpha_2 \\ v_4 \sin\alpha_2 \end{bmatrix} \tag{3.11}$$

where $\phi = \alpha_1 - \gamma$ with $\gamma = \pi - \beta_1$, and $v_i, i = 1, 2, 3, 4$ denotes the norm of the corresponding vector. Equation (3.11) can be rewritten as

$$\begin{bmatrix} a\cos\alpha_1 + b\sin\alpha_1 - v_1 \\ -b\cos\alpha_1 + a\sin\alpha_1 \end{bmatrix} = \begin{bmatrix} v_4 \cos\alpha_2 \\ v_4 \sin\alpha_2 \end{bmatrix} \tag{3.12}$$

in which $a = v_2 + v_3 \cos\gamma$ and $b = v_3 \sin\gamma$. Since $v_2 = v_4$, Equation (3.12) can be rewritten as the following equation by eliminating α_2

$$L \sin\alpha_1 + M \cos\alpha_1 - N = 0, \tag{3.13}$$

which contains only one variable α_1 and where

$$L = 2v_1 b \tag{3.14}$$

$$M = 2v_1 a \tag{3.15}$$

$$N = v_1^2 + v_3^2 + 2v_2 v_3 \cos\gamma. \tag{3.16}$$

By applying the tangent half-angle formula to $\sin\alpha_1$ and $\cos\alpha_1$, one can obtain

$$(M+N)T^2 - 2LT - (M-N) = 0 \tag{3.17}$$

where $T = \tan\frac{\alpha_1}{2}$. This quadratic equation can provide at most two different real solutions for T, which correspond to the two different assembly modes of the 4-bar linkage. At last, the availability of these two solutions should be validated by computing the length of l_{34}. For example, with the same coordinates of the centre of the joints $S_i, i = 1, 2, 3$ given in approach one, the obtained two postures of the platform and the redundant links are shown in Fig. 3.6. It can be seen that the solution shown in Fig. 3.6a is exactly the same as the one shown in Fig. 3.4a, while the other solution shown in Fig. 3.6b is invalid because the length of l_{34} cannot be preserved. Therefore, this method yields only two possible solutions, which can generally be reduced to a unique solution, that can be computed analytically. However, there is no guarantee that one of the two solutions can always be eliminated, although this should be the case in general.

Considering the non-redundant counterpart (the 3-[R(RR-RRR)S] parallel robot) proposed in (Monsarrat and Gosselin, 2001), the Cartesian coordinates of the moving platform can be readily obtained if the position of each of the S joints is determined. If one extra encoder is used to measure the coordinate of a passive R joint located on the base, we are only able to determine the position of the corresponding S joint. Therefore, different assembly modes exist for the moving platform and each of the other two legs. Thereby, the forward kinematic problem still cannot be established as a polynomial equation that is as simple as (3.17).

3.2.4 Approach Four: Using Two Extra Encoders

It is shown in approach three that a unique analytical solution cannot be produced in the presence of only one extra encoder. The elimination of one of the two solutions was done a posteriori. Therefore, we attempt to add two extra encoders to measure the angles β_1 and β_2 of the passive joints R_{14} and R_{24} (see Fig. 3.7). The vector loop equations for these two legs can be written as

$$\mathbf{s}_1 = \mathbf{p} + \mathbf{Q}\mathbf{d}_1 \tag{3.18}$$

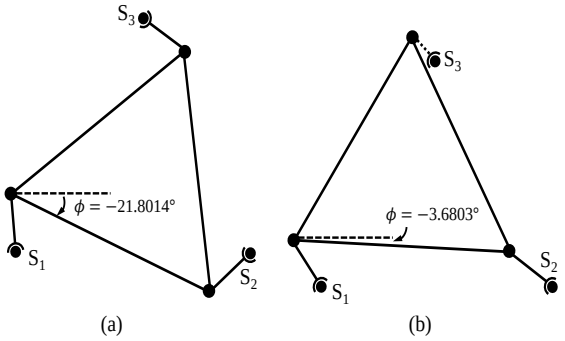

Figure 3.6 – Two different solutions obtained from approach three. Only solution (a) is valid, which can be verified by computing the resulting length l_{34}.

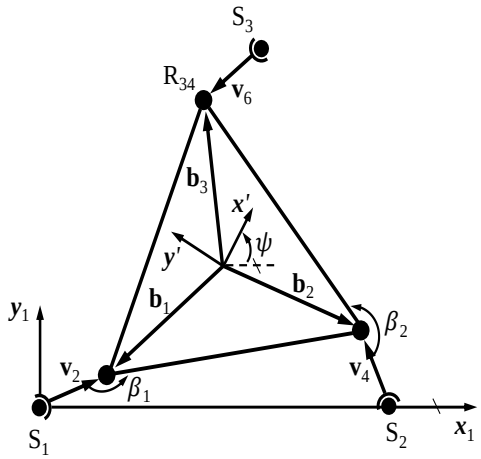

Figure 3.7 – Two extra encoders at joints R_{14} and R_{24}, associated respectively with angles β_1 and β_2.

$$\mathbf{s}_2 = \mathbf{p} + \mathbf{Q}\mathbf{d}_2, \tag{3.19}$$

where $\mathbf{d}_i = \mathbf{b}_i - \mathbf{v}_j$, $i = 1, 2$ and $j = 2i$, which are expressed in the platform frame. Subtracting Eq. (3.18) from Eq. (3.19) yields

$$\mathbf{s}_{12} = \mathbf{Q}\mathbf{d}_{12} \tag{3.20}$$

where the orientation matrix $\mathbf{Q}$ is defined as

$$\mathbf{Q} = {}^{B}_{I}\mathbf{Q}\,{}^{I}_{P}\mathbf{Q} \tag{3.21}$$

where ${}^{B}_{I}\mathbf{Q}$ is given in Eq. (3.3) and ${}^{I}_{P}\mathbf{Q}$ represents the orientation of the platform frame expressed in the intermediate frame defined in Fig. 3.3. Substituting Eq. (3.21) into Eq. (3.20) yields

$${}^{I}_{B}\mathbf{Q}\mathbf{s}_{12} = {}^{I}_{P}\mathbf{Q}\mathbf{d}_{12} \tag{3.22}$$

in which ${}^{I}_{B}\mathbf{Q} = {}^{B}_{I}\mathbf{Q}^{T}$. Since the platform and intermediate frames share the same xy plane, ${}^{I}_{P}\mathbf{Q}$ can be simply expressed as

$$ {}^{I}_{P}\mathbf{Q} = \begin{bmatrix} \cos\psi & -\sin\psi & 0 \\ \sin\psi & \cos\psi & 0 \\ 0 & 0 & 1 \end{bmatrix} \tag{3.23} $$

where angle ψ is illustrated in Fig. 3.7. Substituting Eq. (3.23) into Eq. (3.22) and defining ${}^{I}_{B}\mathbf{Q}\mathbf{s}_{12} = [\lambda\ 0\ 0]^{T}$ and $\mathbf{d}_{12} = [d_{12x}\ d_{12y}\ 0]^{T}$, one can obtain

$$ \begin{bmatrix} d_{12x} & -d_{12y} \\ d_{12y} & d_{12x} \end{bmatrix} \begin{bmatrix} \cos\psi \\ \sin\psi \end{bmatrix} = \begin{bmatrix} \lambda \\ 0 \end{bmatrix}. \tag{3.24} $$

A unique set of solution for $\cos\psi$ and $\sin\psi$ can always be obtained since the matrix in Eq. (3.24) is always invertible, due to the fact that $\mathbf{d}_{12}$ can never be a zero vector. Once ${}^{I}_{P}\mathbf{Q}$ is determined, the orientation matrix $\mathbf{Q}$ can be obtained using Eq. (3.21) while the position vector $\mathbf{p}$ can be obtained using either Eq. (3.18) or Eq. (3.19).

It can be seen that the minimal number of extra encoders that can lead to a unique forward kinematic solution for the KRHPR is two. However, even if the same number of extra encoders is used in the 3-[R(RR-RRR)S] parallel robot to determine the positions of two of the S joints, the Cartesian coordinates still cannot be obtained uniquely because different assembly modes exist for the third leg.

3.2.5 Approach Five: Using Three Extra Encoders

In order to improve the robustness of the forward kinematic solution presented in approach four, a third extra encoder is included to measure the angle of joint R_{34}, In this case, the vector loop equation for the three legs are written as

$$ \mathbf{s}_1 = \mathbf{p} + \mathbf{Q}\mathbf{d}_1 \tag{3.25} $$

$$ \mathbf{s}_2 = \mathbf{p} + \mathbf{Q}\mathbf{d}_2 \tag{3.26} $$

$$ \mathbf{s}_3 = \mathbf{p} + \mathbf{Q}\mathbf{d}_3 \tag{3.27} $$

with $\mathbf{d}_3 = \mathbf{b}_3 - \mathbf{v}_6$. Subtracting Eq. (3.25) from Eqs. (3.26) and (3.27), one can obtain

$$ \mathbf{s}_{12} = \mathbf{Q}\mathbf{d}_{12} \tag{3.28} $$

$$ \mathbf{s}_{13} = \mathbf{Q}\mathbf{d}_{13} \tag{3.29} $$

where $\mathbf{d}_{13} \equiv [d_{13x}\ d_{13y}\ 0]^{T}$. Knowing that vector $\mathbf{q}_z$ in $\mathbf{Q}$ is obtained independently, from the outset (using Eq. (3.2)), the above equations can be rewritten in the following matrix form

$$ \mathbf{A}\mathbf{u} = \mathbf{w} \tag{3.30} $$

where $\mathbf{A}$ is

$$\mathbf{A} = \begin{bmatrix} d_{12x} & 0 & 0 & d_{12y} & 0 & 0 \\ 0 & d_{12x} & 0 & 0 & d_{12y} & 0 \\ 0 & 0 & d_{12x} & 0 & 0 & d_{12y} \\ d_{13x} & 0 & 0 & d_{13y} & 0 & 0 \\ 0 & d_{13x} & 0 & 0 & d_{13y} & 0 \\ 0 & 0 & d_{13x} & 0 & 0 & d_{13y} \end{bmatrix} \tag{3.31}$$

which is of dimension 6×6, and $\mathbf{u} = [\mathbf{q}_x^T \ \mathbf{q}_y^T]^T$ and $\mathbf{w} = [\mathbf{s}_{12}^T \ \mathbf{s}_{13}^T]^T$. Matrix $\mathbf{A}$ is non-singular because vectors $\mathbf{d}_{12}$ and $\mathbf{d}_{13}$ can never be collinear. A unique solution for $\mathbf{u}$ can be obtained using Eq. (3.30) and $\mathbf{p}$ is readily determined using any equation of Eqs. (3.25)-(3.27). It can be seen that compared to the other approaches discussed above, this one is quite straightforward and compact, which reflects the advantages of using three extra encoders.

3.2.6 Approaches Six and Seven: Newton-Gauss Method with Two and Three Extra Encoders

The system of equations used in approach six or seven is obtained by replacing the first two or all the three constraint equations in Eq. (3.4) by the vector loop Eqs. (3.18)-(3.19) or (3.25)-(3.27). Because each vector loop equation can be expanded into three equations by components, the system formed is over-determined, namely: $\mathbf{F}_o(\mathbf{X}) = \mathbf{0}$, and can be solved via the Newton-Gauss method. This is to say, at each iteration $\boldsymbol{\delta}^{(k)}$ in Eq. (3.8) is given as

$$\boldsymbol{\delta}^{(k)} = -\mathbf{J}^{+}\mathbf{F}_o(\mathbf{X}^{(k)}), \quad k = 0, 1, \cdots \tag{3.32}$$

where

$$\mathbf{J}^{+} = (\mathbf{F'}_o(\mathbf{X}^{(k)})^T\mathbf{F'}_o(\mathbf{X}^{(k)}))^{-1}\mathbf{F'}_o(\mathbf{X}^{(k)})^T \tag{3.33}$$

is the Moore-Penrose inverse of $\mathbf{F'}_o(\mathbf{X}^{(k)})$, and where matrix $\mathbf{F'}_o(\mathbf{X})$ is the partial derivative of vector $\mathbf{F}_o(\mathbf{X})$ with respect to vector $\mathbf{X}$. In spite of the computational complexity, the Newton-Gauss method has the potential capability to improve the robustness of approaches four and five.

3.3 Orthonormalization of Matrix Q

In practice, because of inevitable manufacturing and measurement errors, the computed orientation matrix $\mathbf{Q}$ may not be orthonormal. Among the three column vectors in $\mathbf{Q}$, it is clear that only $\mathbf{q}_z$ (given by Eq. (3.2)) is a unit vector, in spite of the errors. Hence we can exploit the Gram-Schmidt process (Strang, 2009) to orthonormalize $\mathbf{Q}$ by taking $\mathbf{q}_z$ as the reference vector. Firstly, three mutually orthogonal vectors $\mathbf{q}_{xo}$, $\mathbf{q}_{yo}$ and $\mathbf{q}_z$ can be constructed by the following formulas

$$\mathbf{q}_{xo} = \mathbf{q}_x - \frac{\mathbf{q}_z^T\mathbf{q}_x}{\mathbf{q}_z^T\mathbf{q}_z}\mathbf{q}_z \tag{3.34}$$

$$\mathbf{q}_{yo} = \mathbf{q}_y - \frac{\mathbf{q}_z^T \mathbf{q}_y}{\mathbf{q}_z^T \mathbf{q}_z}\mathbf{q}_z - \frac{\mathbf{q}_x^T \mathbf{q}_y}{\mathbf{q}_x^T \mathbf{q}_x}\mathbf{q}_x. \tag{3.35}$$

Then, dividing $\mathbf{q}_{xo}$ and $\mathbf{q}_{yo}$ by their norms, i.e., $\mathbf{q}_{xn} = \mathbf{q}_{xo}/||\mathbf{q}_{xo}||$ and $\mathbf{q}_{yn} = \mathbf{q}_{yo}/||\mathbf{q}_{yo}||$. At last, the orthonormalized matrix $\mathbf{Q}_n$ is obtained as

$$\mathbf{Q}_n = [\mathbf{q}_{xn} \quad \mathbf{q}_{yn} \quad \mathbf{q}_z]. \tag{3.36}$$

Note that it is possible to create vector $\mathbf{q}_{yo}$ prior to vector $\mathbf{q}_{xo}$. In this case, the resulting $\mathbf{Q}_n$ may be slightly different from the one obtained by Eqs. (3.34)-(3.36). Moreover, for the forward kinematic approaches in which the position vector $\mathbf{p}$ is computed based on the orientation matrix $\mathbf{Q}$, it is not recommended to apply the Gram-Schmidt process to matrix $\mathbf{Q}$ before the position vector $\mathbf{p}$ is obtained because this may reduce the accuracy of vector $\mathbf{p}$ significantly.

3.4 Example

The dimensional parameters of the 3-RRRSR KRHPR are chosen as follows:

$$R_b = 250 \text{ mm}, \quad R_p = 125 \text{ mm}, \quad l_{i1} = l_{i4} = 50 \text{ mm}$$
$$l_{i2} = 300 \text{ mm}, \quad l_{i3} = 450 \text{ mm}, \quad \alpha = 120^\circ, \quad i = 1, 2, 3$$

where R_b and R_p are respectively the radii of the circumscribed circles of the base and platform.

It was shown in Section 3.2 that a unique forward kinematic solution is obtained only by approaches two, and four to seven and to some extend with approach three. Moreover, approaches one, two, six and seven rely on a numerical method and therefore it cannot be guaranteed that they will converge and if they do that they will converge to the proper solution. Hence, only approaches three, four and five lead to a unique solution that is computed analytically. The drawback of these three methods is that they respectively require one, two or three extra joint sensors. In this section, the feasibility of the different approaches is verified by a simulation trajectory. The desired and real postures of the platform in the presence of measurement errors are compared. In the example, the platform is initially at $\mathbf{p} = [0 \ 0 \ 350]^T$ mm with $\mathbf{Q} = \mathbf{I}$, where $\mathbf{I}$ is the 3×3 identity matrix. Throughout the motion, the angles $\beta_i, i = 1, 2, 3$ between the platform and each redundant link are maintained at 60° by taking advantage of the redundancies. The example trajectory is the same as that provided in Section 1.8, which is described by five sub-trajectories.

In this example, the tilt and translation intervals are respectively set to be 1° and 1 mm. Thus, the trajectory consists of 720 different configurations. With the prescribed configurations, we first calculate the corresponding actuated joint values through the inverse kinematic analysis. Then, we use these actuated joint values as the inputs when implementing the proposed seven approaches. In the approaches which may lead to multiple forward kinematic solutions,

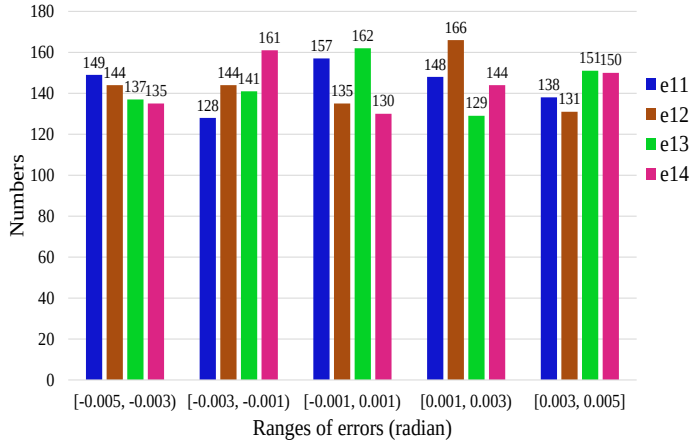

Figure 3.8 – Error distribution of the four encoders in the first leg.

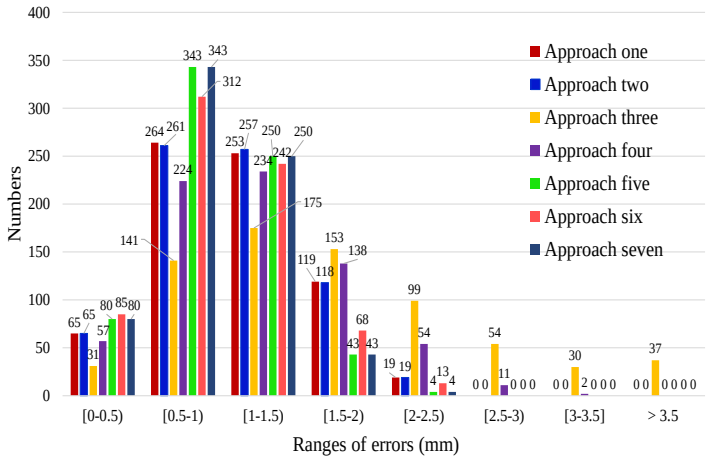

Figure 3.9 – Position errors obtained from the seven approaches.

we choose the actuated joint values that associate with the prescribed robot configurations. The simulation was carried out in MATLAB. It was shown that the simulated position and orientation of the platform are identical to the given trajectory. Nevertheless, in practice, inevitable manufacturing and measurement errors may affect the accuracy of the posture of the robot. To investigate this, random measurement errors in the range of $[-0.005\ 0.005]$ with units in radians are assigned to all (including the extra) encoders. For example, the random errors of the encoders in the first leg are shown in Fig. 3.8, here $e1j, j = 1, 2, 3, 4$ denote the encoder errors of joint R_{1j}. The number at the top of each bar indicates the number of errors that fall within the corresponding error range. The total number for a given joint is 720. The position error is defined as

$$e_p = ||\mathbf{p}_d - \mathbf{p}_r|| \tag{3.37}$$

and the orientation errors are defined as

$$e_{oc} = ||\mathbf{Q}_d - \mathbf{Q}_r||_2 \tag{3.38}$$

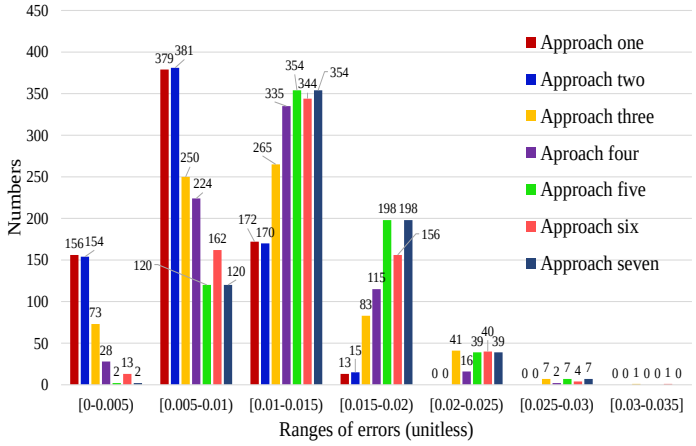

Figure 3.10 – Errors of the orientation matrix $\mathbf{Q}$ obtained from the seven approaches.

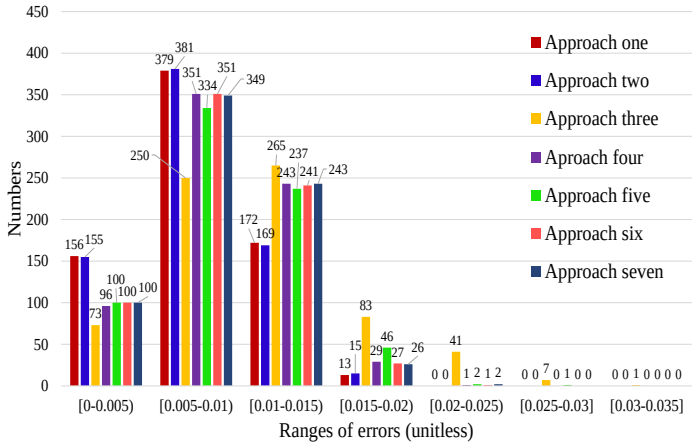

Figure 3.11 – Errors of the orthonormalized orientation matrix $\mathbf{Q_n}$ obtained from the seven approaches.

$$e_{on} = ||\mathbf{Q}_d - \mathbf{Q}_n||_2 \tag{3.39}$$

where $\mathbf{p}_d$ and $\mathbf{Q}_d$, and $\mathbf{p}_r$ and $\mathbf{Q}_r$ are respectively the desired and real position and orientation of the platform, $\mathbf{Q}_n$ is given in Eq. (3.36), and $||\cdot||_2$ stands for the 2-norm of a matrix. The position error e_p is of unit millimeters while the orientation errors e_{oc} and e_{on} are unitless.

The results of e_p are illustrated in Fig. 3.9. It can be observed that approach three is the worst, because it has the least number in the lower error ranges but the most number in the higher ones. Approach four is less robust than the others except approach three. However, the robustness of approach four can be improved considerably by implementing the Newton-Gauss method, as it can be seen from the results of approach six, although such an improvement is at the expense of computational complexity. Approaches one, two, and five to seven produce no errors larger than 2.5 mm. These approaches have the potential for practical applications. Among them, approaches five and seven are the most robust, which clearly shows the advantage

of using three extra encoders. Approaches one and two are comparable. Although they are less robust than approaches five to seven, the structure of the robot remains compact due to no extra encoders.

The results of e_{oc} are shown in Fig. 3.10. Basically, all the approaches are acceptable for solving the forward kinematic problem because of the very small errors. Nevertheless, it can be seen that in the ranges of $[0 - 0.005)$ and $[0.005 - 0.01)$, approaches one and two are definitely dominant. At the same time, it shows that approaches five and seven are the worst in the same ranges. This indicates that the main contribution of using three extra encoders is to improve the position accuracy. Figure 3.11 shows the errors between the desired and orthonormalized orientation matrices. It can be seen that the Gram-Schmidt process imposes less effects on the approaches one to three, which reflects that the obtained orientation matrix $\mathbf{Q}$ is almost orthogonal all the time. However, after orthonormalization, the accuracy of the rotation matrix obtained by approaches four to seven are improved dramatically, thereby reducing the gap between them and the approaches one and two.

This simulation mainly focuses on the accuracy analysis of the proposed approaches. Based on the above analysis, approaches three and four are excluded due to the poor position accuracy. It also shows that with the chosen simulation intervals, the approaches using a numerical method always converge to the desired solution. In addition, since the difference in calculation speed between the numerical and analytical methods is negligible, the uniqueness and reliability of the solution, and the complexity of the design will be the criteria for us to choose the approach for solving the forward kinematic problem. For example, the KRHPRs proposed in Chapter 2 are mainly used for pHRI applications. Thereby, approach two is recommended since the structure of the robot remains compact. On the other hand, in general applications in which the moving platform is less prone to interact with the environment, we recommend approach five though additional wires must be reaching the end-effector.

3.5 Forward Kinematics of the $\underline{\text{R}}(\underline{\text{R}}\text{R-}\underline{\text{R}}\text{RR})$ Sub-Leg

As studied in Chapter 2, a feasible sub-leg that can be used for composing the $(6 + 3)$-dof KRHPR could be serial, parallel, hybrid or redundant, as long as the sub-leg can produce three translational degrees of freedom at the corresponding passive spherical joint. The approaches developed in Section 3.2 are independent of the type of the sub-leg. Thereby, they are easily applied to other KRHPRs with platform assembly arrangement (a), except that in different architectures the position vector of the passive spherical joint of the redundant link should be determined accordingly, which corresponds to solving the forward kinematics of the sub-leg. If the sub-leg is serial, the forward kinematic solution is unique and is readily obtained. Otherwise, multiple forward kinematic solutions may exist and the user should choose the most suitable one. For example, considering the $\underline{\text{R}}(\underline{\text{R}}\text{R-}\underline{\text{R}}\text{RR})$ hybrid sub-leg (actuator one

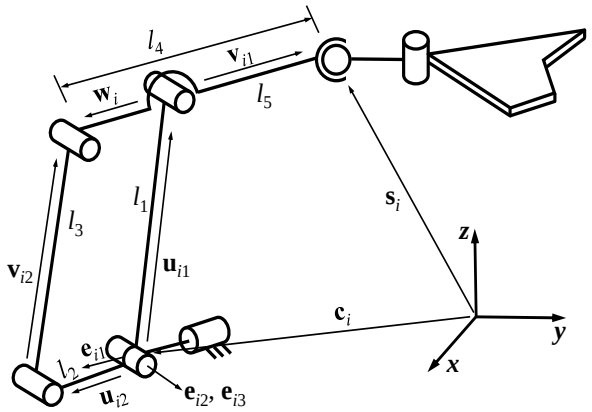

Figure 3.12 – Kinematic modelling of the R(RR-RRR) sub-leg.

is arranged in series, while actuators two and three are arranged in parallel) of the 3-[R(RR-RRR)SR] architecture studied in Chapter 1. The kinematic modelling of this hybrid sub-leg is schematically shown in Fig. 3.12. All vectors are expressed with respect to the base frame and the unit vector $\mathbf{e}_{ij}, i, j = 1, 2, 3$ represents the direction of the jth actuated joint of the ith leg.

Vector $\mathbf{s}_i, i = 1, 2, 3$ is determined using the following procedures. In the sub-leg, vector $\mathbf{w}_i$ can be expressed as

$$\mathbf{w}_i = \mathbf{Q}_i \begin{bmatrix} (l_4 - l_5)\cos\xi_i \\ (l_4 - l_5)\sin\xi_i \\ 0 \end{bmatrix}, \qquad i = 1, 2, 3 \tag{3.40}$$

where $\mathbf{Q}_i$ is the orientation matrix of the local frame at the second and third actuated joints of the ith leg with respect to the base frame, which only depends on the magnitude of the first actuated joint. ξ_i is the angle between vectors $\mathbf{w}_i$ and $(\mathbf{e}_{i1} \times \mathbf{e}_{i2})$. The constraint equation on the length of the link along vector $\mathbf{v}_{i2}$ can be written as

$$(\mathbf{m}_i + \mathbf{w}_i)^T(\mathbf{m}_i + \mathbf{w}_i) = \mathbf{m}_i^T\mathbf{m}_i + 2\mathbf{m}_i^T\mathbf{w}_i + \mathbf{w}_i^T\mathbf{w}_i = l_3^2 \tag{3.41}$$

where

$$\mathbf{m}_i = \mathbf{u}_{i1} - \mathbf{u}_{i2} \tag{3.42}$$

and

$$\mathbf{w}_i^T\mathbf{w}_i = (l_4 - l_5)^2. \tag{3.43}$$

Substituting Eq. (3.40) into Eq. (3.41) and rearranging the terms, we obtain

$$G_i\cos\xi_i + H_i\sin\xi_i + I_i = 0 \tag{3.44}$$

where

$$G_i = 2(l_4 - l_5)\mathbf{m}_i^T\mathbf{Q}_i\mathbf{e}_1 \tag{3.45}$$

(a) (b) (c) (d)

Figure 3.13 – Example of a translational motion.

$$H_i = 2(l_4 - l_5)\mathbf{m}_i^T \mathbf{Q}_i \mathbf{e}_2 \tag{3.46}$$

$$I_i = \mathbf{m}_i^T \mathbf{m}_i + (l_4 - l_5)^2 - l_3^2 \tag{3.47}$$

with

$$\mathbf{e}_1 = \begin{bmatrix} 1 \\ 0 \\ 0 \end{bmatrix}, \quad \mathbf{e}_2 = \begin{bmatrix} 0 \\ 1 \\ 0 \end{bmatrix}. \tag{3.48}$$

Equation (3.44) can be converted to a quadratic equation using the tangent half-angle formula. Angle ξ_i as well as vector $\mathbf{w}_i$ are then readily obtained. The position of the spherical joint can then be expressed as

$$\mathbf{s}_i = \mathbf{c}_i + \mathbf{u}_{i1} + \mathbf{v}_{i1} \tag{3.49}$$

in which $\mathbf{c}_i$ is a constant vector and

$$\mathbf{v}_{i1} = \frac{l_5}{l_5 - l_4}\mathbf{w}_i. \tag{3.50}$$

A maximum of two different solutions are obtained. This is in agreement with what we can observe on a physical model of the sub-leg. Indeed, for given values of the actuated joints, it is easily observed that the sub-leg can be assembled in two different configurations. It is also easy to select the proper solution by considering the assembly mode of the $\underline{\text{R}}\text{R}$-$\underline{\text{R}}\text{RR}$ linkage.

Approach two of the forward kinematic algorithms presented in this chapter was implemented in the real-time controller of the 3-[$\underline{\text{R}}$($\underline{\text{R}}$R-$\underline{\text{R}}$RR)SR] prototype. Since the prototype is used for pHRI, the Cartesian coordinates of the platform have not been determined using external measurements (e.g. a vision system), which would have allowed a comparison of the actual pose of the platform with the computed one. However, the results obtained are continuous and yield a smooth and correct motion of the platform. This is illustrated in Figs 3.13 and 3.14, where a few pictures of the experiments are shown, for a translational trajectory and for a rotational trajectory.

3.6 Conclusion

Seven different approaches for the solution of the forward kinematic problem of KRHPRs with platform assembly arrangement (a) are developed. Three of them result in an analytical

(a) (b) (c) (d)

Figure 3.14 – Example of a tilt motion.

solution while a numerical procedure is utilized in the other approaches. It is shown that with the same number of encoders, the forward kinematics of the proposed KRHPRs can be solved much more easily than that of their non-redundant counterparts by implementing approaches one, three and four. The feasibility of these approaches is validated through a simulation based on the 3-RRRSR architecture. It is shown that approach five (and approach seven) is the most robust and can therefore be implemented in general applications. In particular applications such as pHRI, approach two — without extra encoders — is recommended since the implementation of approach five requires extra sensors on the platform, thereby requiring wired connections to the platform, which is a drawback. Approach two can satisfy the real-time control requirements, which is realized by the 3-[R(RR-RRR)SR] prototype. Because kinematic redundancy is used to avoid singularities, the numerical approach is reliable and robust since the robot is never close to a singular configuration. Moreover, it can be observed that, although the detailed expressions should be modified, all of the seven approaches are readily applied to solve the forward kinematic problem of the planar KRHPRs with platform assembly arrangement (a), while the forward kinematic problem of the planar and spatial KRHPRs with platform assembly arrangements (b) and (c) proposed in Chapter 2 could be solved using approaches two, and four to seven.

Chapter 4

Workspace Enlargement and Joint Trajectory Optimisation of KRHPRs with Spherical-Revolute Redundant Links

4.1 Introduction

It has been shown in Chapters 1 and 2 that because the inverse kinematic problem of the proposed KRHPRs is solved analytically, we are able to actively control the redundant degrees of freedom. In the examples studied in the previous chapters, the redundant parameters of the KRHPRs are chosen somewhat arbitrary and based on the consideration that as long as the type II singularities can be avoided. However, the size of the workspace and the dexterity of the robot may be affected due to different parameters of redundancy. In this chapter, we investigate the possibilities to enlarge the workspace and optimise the joint trajectory (e.g., minimise the performance indices) of the KRHPRs by determining the optimal redundant parameters.

For the sake of simplicity, the approaches for workspace enlargement and joint trajectory optimisation that will be discussed in the following sections are implemented in the 3-RRRSR $(6+3)$-dof KRHPR (see Figs. 3.1, 3.2 and 2.6). Nevertheless, these approaches are readily applied to other KRHPRs with platform assembly arrangement (a) proposed in Chapter 2.

In the next section, an approach of enlarging the translational and rotational workspaces of the KRHPR is proposed and the results are compared with those obtained in Chapter 1. A local optimisation on the redundant parameters is also pursued. Then, an approximate optimal joint trajectory planning strategy is developed, and its rationality is verified by example trajectories.

Finally, conclusions are presented.

4.2 Workspace Enlargement

4.2.1 Possibilities to Enlarge the Workspace

The geometric parameters of the 3-RRRSR KRHPR are the same as those shown in Section 3.4. In this subsection, we consider three cases that may affect the size of the workspace, namely varying: 1) the three angles β_i (see Fig. 2.6); 2) the length of the three redundant links l_{i4}; and 3) the set of (R_p, l_{i4}) in which the length of l_{i4} is given in 2) and $R_p = \frac{5}{2} l_{i4}$. In each case, the remaining geometric parameters of the KRHPR are unchanged.

For the sake of brevity, the translational and orientational workspaces (see Figs. 1.6 to 1.9) are reassessed only for the layers of $z = 350$ mm and $\psi = 0°$, respectively. In each case, four different magnitudes of β_i, l_{i4}, and (R_p, l_{i4}) are chosen. The results are presented in Fig. 4.1. It can be observed that as the value of β_i or l_{i4} increases, the translational workspace is enlarged in all directions, but the enlargement is quite limited (see Figs. 4.1a and 4.1b). However, the orientational workspace could be enlarged significantly in certain directions (see Figs. 4.1d and 4.1e), which is desired for such a KRHPR. On the other hand, as it can be observed in Figs. 4.1c and 4.1f, a larger magnitude of (R_p, l_{i4}) reduces the workspaces considerably, because the robot in this case is much more prone to reach the joint limits or mechanical interferences than in the other two cases.

4.2.2 A Locally Optimal Design

The velocity equations and the Jacobians $\mathbf{J}$ and $\mathbf{K}$ of the 3-RRRSR KRHPR have been studied in Section 2.3.1. In this subsection, we provide a method based on computing a performance index to determine the optimal value of the redundant coordinates for each case studied in the previous subsection. Three indices are suggested, which are the same as those proposed in Section 1.8, namely:

η_1 : the 2-norm of the position part of matrix $\mathbf{U}$, where $\mathbf{U} = \mathbf{J}^{-1}\mathbf{K}$;

η_2 : the 2-norm of the rotation part of matrix $\mathbf{U}$;

η_3 : the condition number of a novel Jacobian $\mathbf{J}_1$ with the form as that shown in (1.52), in which the the Jacobians of the ith, $(i = 1, 2, 3)$ RRR linkage are defined in (2.15).

The calculation for an optimisation over the whole workspace is time-consuming, because this requires to compute the performance indices for each evaluation node of the workspace, and there exists a tremendous number of evaluation nodes due to the discretisation method (Merlet, 2006b). Thus, only small portions, e.g., the translational workspace along the x-axis

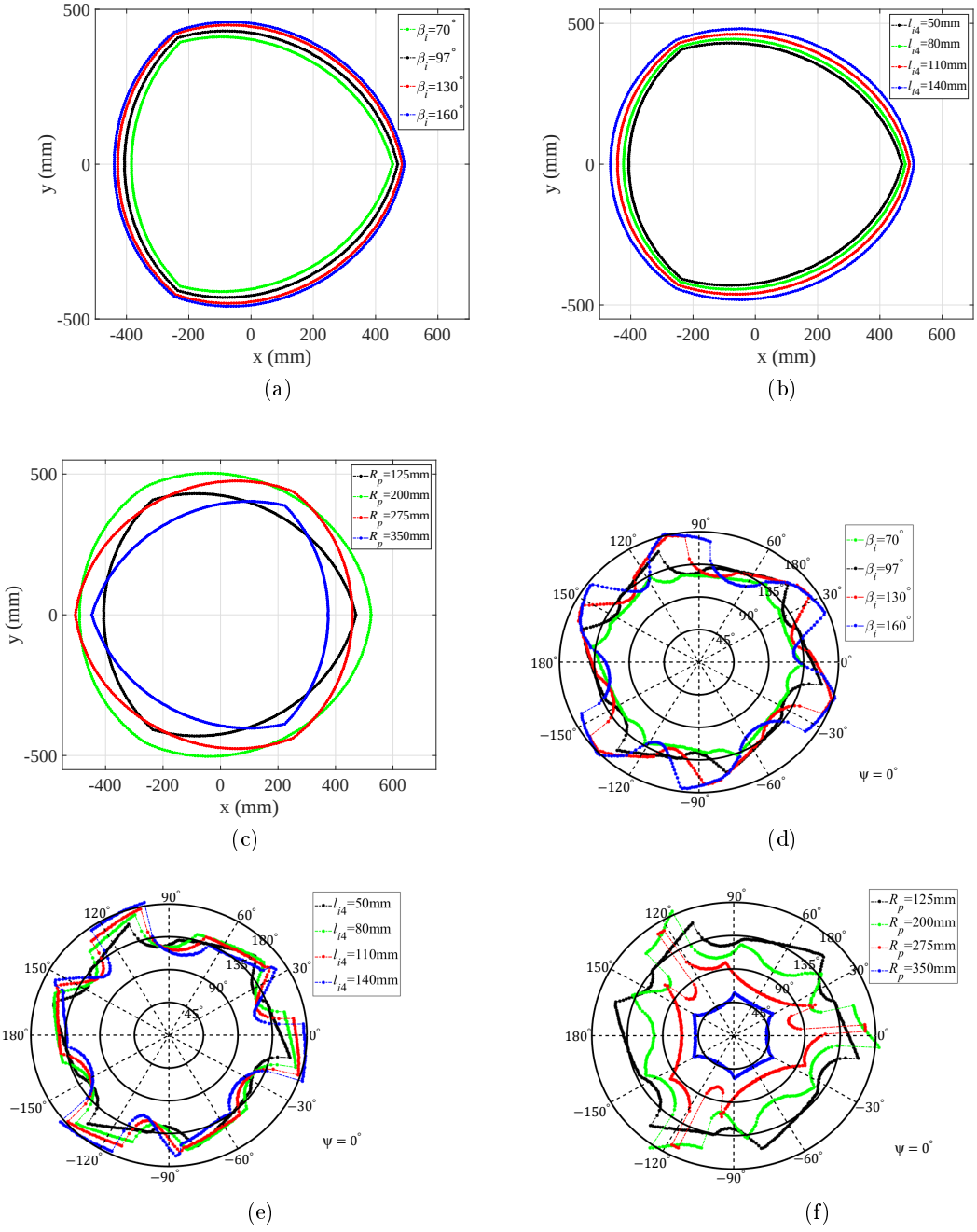

Figure 4.1 – Translational workspace ((a)-(c)) for $z = 350$mm and orientational workspace ((d)-(f)) for $\psi = 0°$, evaluated with respect to different magnitudes of β_i, l_{i4}, and (R_p, l_{i4}).

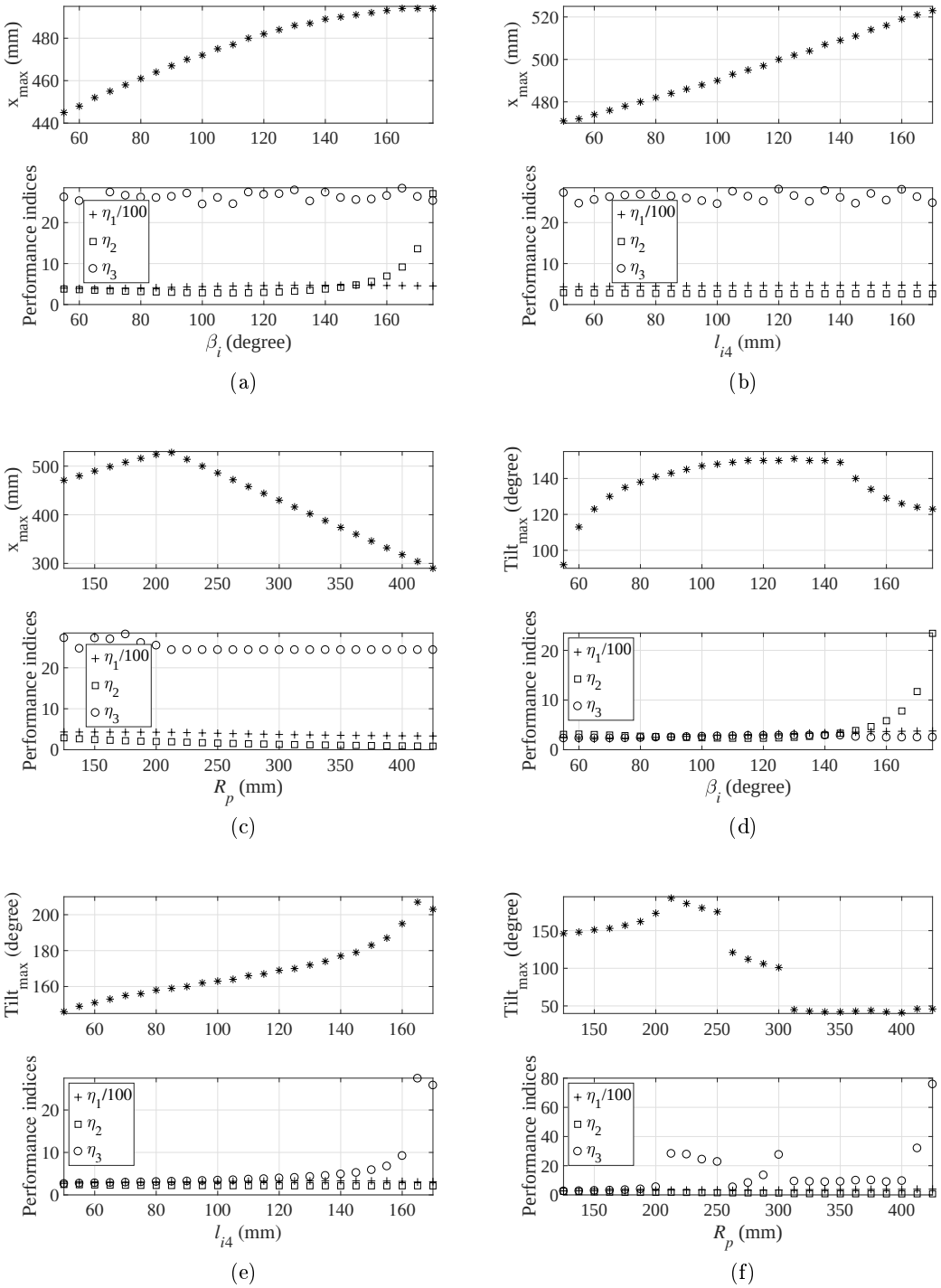

Figure 4.2 – The maximum translational distance along the x-axis ((a)-(c)) and tilt angles ((d)-(f)) of specified portions of the workspace and the corresponding performance indices, evaluated with respect to different magnitudes of β_i, l_{i4}, and (R_p, l_{i4}).

of layer $z = 350$ mm and the tilt motion with respect to the y'-axis of layer $\psi = 0°$ of the rotational workspace, are considered. Therefore, this is only a locally optimal design.

The minimum value of the angles $\beta_i, i = 1, 2, 3$ in case 1) is assumed to be 55° in order to prevent the platform from interfering with vicinal links, while the minimum length of the redundant links $l_{i4}, i = 1, 2, 3$ in cases 2) and 3) is assumed to be 50 mm. The angles increase by 5° at a time, while the incremental interval of the redundant links are set to be 5 mm. In each evaluation the performance indices are computed when the robot reaches the workspace boundary. The simulation results are presented in Fig. 4.2. In order to fit the scale of the vertical axis, the numerical values of η_1 are divided by 100. It can be observed that:

1) The values of $\eta_1/100$ in every sub-figure, as well as the values of η_2 in Figs. 4.2b, 4.2c, 4.2e and 4.2f are stable. Nevertheless, this is not sufficient to guarantee that the robot stays away from singularities. The values of η_3 should also be taken into consideration. It can be seen from Figs. 4.2e and 4.2f that the robot is close to type I singularities when the values of η_3 are much higher than 1;

2) In Figs. 4.2a and 4.2d, the value of η_2 increases abruptly as the magnitude of β_i becomes larger. In fact, the value of η_2 reaches infinity when $\beta_i = 180°$. In this configuration the three lines along the redundant links intersect at one common point (a type II singularity), and an instantaneously uncontrollable rotational dof with respect to the z'-axis is generated;

3) The values of η_3 shown in Figs. 4.2(a-c) indicate that the robot is close to the type I singularities in the corresponding configurations. This is because at the boundary of the translational workspace one or more legs of the robot are almost fully extended;

4) Based on the values of the performance indices shown in Fig. 4.2, it can be seen that a relatively large range of the specified portion of the workspace can be obtained if β_i, l_{i4} and (R_p, l_{i4}) for the cases 1), 2) and 3) are selected to be $\beta_i = 140°$, $l_{i4} = 160$ mm and $(R_p, l_{i4}) = (200, 80)$ mm, respectively.

Depending on the applications, various geometric parameters of the redundant links and the moving platform of the proposed KRHPR may be selected. The above method provides a preliminary optimisation scheme for these parameters.

4.3 Joint Trajectory Optimisation

Infinitely many joint trajectories exist for a given Cartesian trajectory of the moving platform of a kinematically redundant robot. In general, a joint trajectory is selected based on the minimisation of a performance index. The inverse kinematic problem of such a robot is

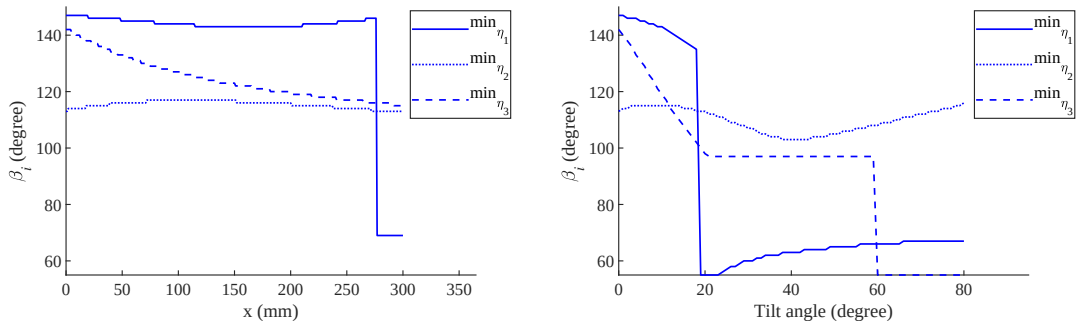

Figure 4.3 – Optimal β_i corresponding to the minimum of different indices for the translation (a) and rotation (b) trajectories.

commonly solved using a numerical method relying on the velocity equations (Siciliano, 1990), in which the actuated joint variables of the robot always approach the optimal configuration to minimize a performance index (Chang, 1987). However, sometimes it is inconvenient to implement such a solution due to several reasons. For instance: the initial configuration should be prescribed; it must be guaranteed that the solution converges; and the robot may suffer from the repeatability problem. In comparison, the proposed KRHPR will not suffer from these drawbacks if the analytical inverse kinematic solution is exploited. On the other hand, the actuated joint variables may not be in an optimal configuration, since the selected value of each angle β_i (see Fig. 2.6) is somewhat arbitrary.

One possible way to overcome this problem is to calculate the values of a performance index for all feasible combinations of $(\beta_1, \beta_2, \beta_3)$ for each given pose of the moving platform, and identify the angles that minimise the index. However, the computation is not efficient since there exists in fact infinitely many combinations of $(\beta_1, \beta_2, \beta_3)$. To simplify this, we assume that the three angles are equal to each other at all times and limited to be an integer in the range of $[55°175°]$. This range is chosen in order to prevent the interferences between the spherical-revolute redundant links and the moving platform and to avoid the type II singularities.

Example trajectories of a translation along the x-axis with $z = 350$ mm, and a rotation with $\psi = 0°$, $0° \leq \phi \leq 80°$ and $\theta_c = 0°$ (where θ_c is defined in (1.38)) are simulated. The minima of the indices $\eta_i, i = 1, 2, 3$ provided in Subsection 4.2.2 for each pose of the platform during the trajectories are detected (see Fig. 4.3). The vertical axis in Fig. 4.3 denotes the value of β_i where η_i reaches its minimum, $\min_{\eta_i}$. It can be seen that the results of η_1 and η_3 are unacceptable since at some trajectory points the magnitude of β_i should decrease rapidly, which may result in an unstable motion of the robot. The numerical values of $\eta_1/100$ for particular trajectory points near the rapid decrease of β_i shown in Fig. 4.3a are illustrated in Fig. 4.4a, which clearly shows that the rapid change is caused by the shifting of the global

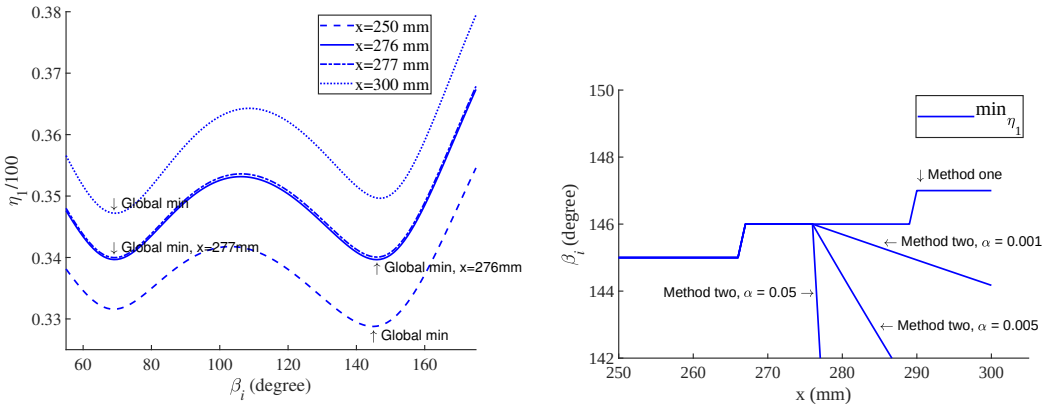

(a) (b)

Figure 4.4 – The global minimum of η_1 for certain magnitudes of x in the translation trajectory (a) and the filtered β_i according to η_1 (b).

minimum of $\eta_1/100$ (or η_1). This drawback is readily avoided using one of two methods. The first method is to scale down the range of β_i that is used in computing the minimum of an index to ensure that there exists only one minimum for η_1. For instance, if β_i is limited to be in the range of [140°160°], the $\min_{\eta_1}$ after the rapid decrease in Fig. 4.3a will be that labelled as "Method one" shown in Fig. 4.4b. The second method is to filter the data of β_i using exponential smoothing. The formulas are given as

$$\beta_{i,0} = a_0 \tag{4.1}$$

$$\beta_{i,t} = \alpha a_t + (1-\alpha)a_{t-1}, \quad t > 0 \text{ and } 0 < \alpha < 1 \tag{4.2}$$

where $\beta_{i,0}$ could be 146°, the value of β_i just before the rapid decrease (see Fig. 4.4b). The results of $\min_{\eta_1}$ after smoothing are shown in Fig. 4.4b labelled "Method two" with specified different values for the smoothing factor α. Referring to the graph of Fig. 4.4a, we can see that method one will try to follow the second local minimum (on the right) because it cannot reach the one on the left and therefore β_i will increase. However, method two will try to reach the global minimum (on the left) and therefore it will make β_i decrease, until it progressively reaches the global minimum on the left. The difference between these two methods is reduced if a smaller value of α is chosen. In addition, the index η_3 shown in Fig. 4.3b can also be corrected using the same methods.

4.4 Conclusion

It was shown that, by adjusting the redundant parameters of the 3-RRRSR (6 + 3)-dof KRHPR, although the enlargement on the translational workspace is limited, the orientational workspace can be improved considerably in certain tilt directions. An approach for determining the optimal configuration of the actuated joint variables is developed, in which

a performance index can be minimised approximately without using the numerical inverse kinematic solution. The methods provided in this chapter can be applied directly to other KRHPRs with platform assembly arrangement (a) proposed in Chapter 2. Furthermore, because only the coordinates of redundancy are taken into consideration in this investigation, the concepts presented in this chapter can also be implemented in the KRHPRs with platform assembly arrangements (b) and (c) proposed in Chapter 2.

Chapter 5

Static Model Based Grasping Force Control of Parallel Grasping Robots with Partial Cartesian Force Measurement

5.1 Introduction

In some of recently proposed kinematically redundant parallel robots (Gosselin et al., 2015) and KRHPRs studied in the previous chapters, the redundancy is further utilised to operate a remote gripper on the moving platform. An example of a planar $(3+1)$-dof kinematically redundant parallel robot with R$\underline{\text{P}}$R legs proposed in (Gosselin et al., 2015) is schematically presented in Fig. 5.1. This robot is the kinematically redundant counterpart of the planar parallel 3-R$\underline{\text{P}}$R architecture (see, for instance (Gosselin and Angeles, 1988; Daniali et al., 1995; Laliberté et al., 1999; Arsenault and Boudreau, 2006)), and has three Cartesian degrees of freedom, i.e., the position of point P and the orientation of link PB (angle ϕ), and one additional local dof, i.e., the orientation of link SB (angle β). Different from many other kinematically redundant parallel robots whose inverse kinematic problem is solved using a numerical method at the velocity level (see, for instance (Gosselin and Schreiber, 2016)), the inverse kinematic problem of the robots proposed in (Gosselin et al., 2015) and of the KRHPRs can be solved analytically at the displacement level. Therefore, we are able to actively control the redundant coordinates (the open and close of each jaw of the gripper), as demonstrated in this video: `https://www.youtube.com/watch?v=_vp1ELEtDN4`.

In this chapter, we are particularly interested in the grasping force control of the above mentioned parallel grasping robots. In this study, we assume that the grasped object is rigid, lightweight, and the geometry is known. In a conventional grasping system which consists

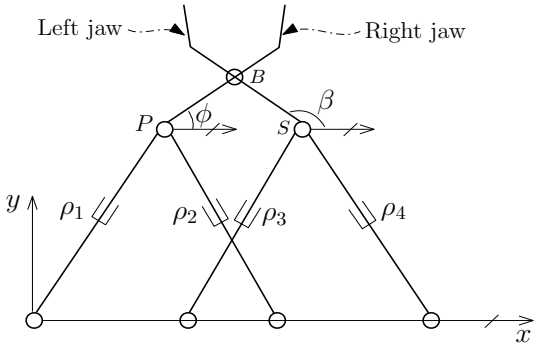

Figure 5.1 – Kinematically redundant planar 4-dof parallel robot with RPR legs and remotely operated gripper.

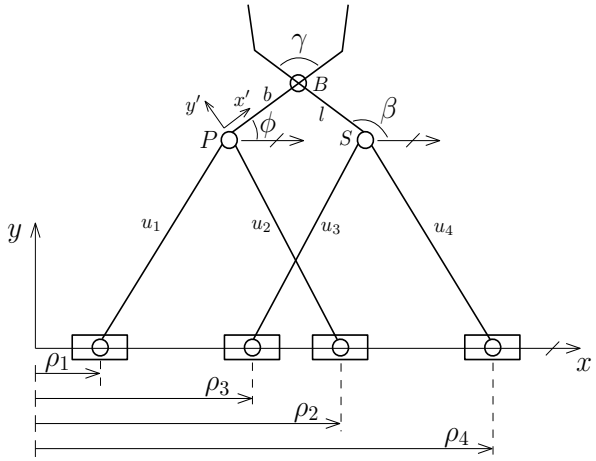

Figure 5.2 – Kinematically redundant planar 4-dof parallel robot with PRR legs.

of a robot arm and a gripper, the robot arm is mainly used to deliver the gripper to the appropriate grasping configuration (Babin and Gosselin, 2018; Babin et al., 2019). The grasp control is somewhat independent from the motion control of the robot arm because the former can be conducted using the gripper's own actuator (Romano et al., 2011). The grasping force is usually not considered as the interaction force between the robot arm and the environment. Nevertheless, in our case, the gripper is operated by the robot's actuators (see, Fig. 5.1), the movement of the robot could be affected by the external force applied to the robot by the environment (the grasped object). Hence, a model of the robot that describes the relationship between the external force and the actuated joint forces/torques should be included in the grasping force control loop.

Rather than developing the dynamic model, which is computationally complex, we prefer, and it is feasible, to use the static model for performing grasping force control of the kinematically redundant parallel/hybrid parallel robots. As it is investigated in (Gosselin et al., 2015) and Chapter 2, the type of the joints used in the legs of the robots is not limited and the geometric design is less restrictive. For example, the RPR legs (see, Fig. 5.1) can be replaced by PRR

legs (see, Fig. 5.2) without changing the mobility of the robot. This allows the use of legs in which the actuators are located on or close to the base. Moreover, no gripper actuators are required. Therefore, the inertia of the moving parts could be very small, and hence the inertia force is not that critical when the acceleration of the robot is limited. By contrast, in a conventional grasping system with a lightweight robot arm, the inertia of the hand/gripper would still be a concern due to the actuators, though an underactuated hand/gripper (see, for instance (Gosselin et al., 2008; Massa et al., 2002; Kragten et al., 2011; Grioli et al., 2012; Catalano et al., 2014; Lévesque et al., 2018)) is utilised.

Different from non-redundant and redundantly actuated parallel robots whose type of redundancy is uniquely clarified, the above mentioned kinematically redundant parallel/hybrid parallel robots can also be considered to be redundantly actuated, or non-redundant (Schreiber and Gosselin, 2019). For example, if the local dof of the planar robot shown in Fig. 5.1 is blocked (when a rigid object is grasped), the robot is redundantly actuated since the number of actuators is higher than the number of Cartesian degrees of freedom. On the other hand, if it is taken as an additional Cartesian dof, the robot can be considered non-redundant since it has the same number of actuators and Cartesian degrees of freedom. Thus, we propose three different static models corresponding to the types of redundancy of the parallel robot. Two case studies based on a planar and a spatial parallel robot are provided. The effectiveness of each of the static models for pursuing grasping force control will be investigated in the following sections.

Finally, in this chapter, we propose a partial Cartesian force measurement approach for implementing the grasping force control, i.e., not all components of the Cartesian force and moment are measured. Typically, in the case that the desired force applied to the environment by a robot manipulator is controlled, a multi-degrees-of-freedom force/torque sensor is utilised to measure the interacting force and moment acting at the robot's end-effector. However, we will show that in our case we only need to measure the grasping force (the force component orthogonal to the plane of each jaw of the gripper), which is just a component of the external force. The external moment and the remaining components of the external force are calculated through the static equilibrium analysis of the grasped object. This approach allows the use of low-cost 1-dof load cells for the measurement, which is a significant advantage.

The rest of this chapter is organised as follows. Three different means of static modelling for a planar and a spatial parallel grasping robots are presented respectively in Section 5.2 and Section 5.3. The feasibility of these static models for grasping force control is analysed in Section 5.4. Experiments of indirect and direct grasping force control of the planar parallel robot based on one of the static models are conducted in Section 5.5. Finally, conclusions are drawn in Section 5.7.

5.2 Static Modelling of a Planar Parallel Robot

The static modelling of the planar parallel robot shown in Fig. 5.2 is studied in this section. The two jaws (links PB and SB) are connected by a pivot at point B. The axes of all prismatic joints are aligned with the x-axis of the base frame. The position vector of the centre of each prismatic joint is written as

$$\mathbf{a}_i = \rho_i \mathbf{e}_1, \quad i = 1, 2, 3, 4 \tag{5.1}$$

where $\mathbf{e}_1$ is the constant unit vector oriented along the x-axis, namely

$$\mathbf{e}_1 = \begin{bmatrix} 1 & 0 \end{bmatrix}^T. \tag{5.2}$$

The detailed derivation of the static models associated with different types of redundancy are given in the following subsections.

5.2.1 Kinematically Redundant

In (Gosselin et al., 2015), the three Cartesian coordinates of the planar parallel robot are denoted by $[\mathbf{p}^T \ \phi]^T$, where $\mathbf{p}$ is the position vector of point P and ϕ is the orientation of the link PB with respect to the base frame. The left jaw is considered to be a link connecting to the end-effector (the right jaw). If a rigid object is grasped, the force applied to the left jaw by the grasped object will appear as an external force acting at this link.

The velocity Jacobian matrices of the kinematically redundant planar parallel robot are firstly provided in (Gosselin et al., 2015), and are briefly recalled here. A moving frame $Px'y'$ is attached to the right jaw whose origin is at point P and the x'-axis is pointing from point P to point B. The velocity equations of the robot can be written as

$$\mathbf{J}_k \mathbf{t} = \mathbf{K}_k \dot{\boldsymbol{\rho}} \tag{5.3}$$

where $\mathbf{t} = [\dot{\mathbf{p}}^T \ \dot{\phi}]^T$ and $\dot{\boldsymbol{\rho}} = [\dot{\rho}_1 \ \dot{\rho}_2 \ \dot{\rho}_3 \ \dot{\rho}_4]^T$, and where Jacobians $\mathbf{J}_k$ and $\mathbf{K}_k$ are defined as

$$\mathbf{J}_k = \begin{bmatrix} (\mathbf{p} - \mathbf{a}_1)^T & 0 \\ (\mathbf{p} - \mathbf{a}_2)^T & 0 \\ (\mathbf{s} - \mathbf{b})^T & (\mathbf{s} - \mathbf{b})^T \mathbf{E} \mathbf{Q}_\phi \mathbf{v}_1 \end{bmatrix} \tag{5.4}$$

and

$$\mathbf{K}_k = \begin{bmatrix} (\mathbf{p} - \mathbf{a}_1)^T \mathbf{e}_1 & 0 & 0 & 0 \\ 0 & (\mathbf{p} - \mathbf{a}_2)^T \mathbf{e}_1 & 0 & 0 \\ 0 & 0 & k_{33} & k_{34} \end{bmatrix} \tag{5.5}$$

in which $\mathbf{s}$ and $\mathbf{b}$ are respectively the position vectors of points S and B, matrix $\mathbf{E}$ is defined as

$$\mathbf{E} = \begin{bmatrix} 0 & -1 \\ 1 & 0 \end{bmatrix}, \tag{5.6}$$

$\mathbf{Q}_\phi$ is the orientation matrix of the moving frame $Px'y'$ with respect to the fixed base frame and is written as

$$\mathbf{Q}_\phi = \begin{bmatrix} \cos\phi & -\sin\phi \\ \sin\phi & \cos\phi \end{bmatrix}, \tag{5.7}$$

and $\mathbf{v}_1$ is a vector connecting point P to point B, expressed in the local frame $Px'y'$, namely

$$\mathbf{v}_1 = \begin{bmatrix} b & 0 \end{bmatrix}^T, \tag{5.8}$$

and the detailed expressions of the components k_{33} and k_{34} in matrix $\mathbf{K}_k$ are described in (Gosselin et al., 2015), thereby they are not shown here for brevity. The Jacobian $\mathbf{J}_k$ is of dimension 3×3 while the Jacobian $\mathbf{K}_k$ is of dimension 3×4. The kinematic redundancy is apparent from matrix $\mathbf{K}_k$.

According to the principle of virtual work, one has

$$\mathbf{F}^T \delta\mathbf{D} = \mathbf{f}^T \delta\boldsymbol{\rho} \tag{5.9}$$

where $\mathbf{F}$ is a 3×1 Cartesian force and moment vector acting at the right jaw, $\delta\mathbf{D}$ is a 3×1 vector of infinitesimal Cartesian displacement of the right jaw, $\mathbf{f}$ is a 4×1 vector of the actuator forces, and $\delta\boldsymbol{\rho}$ is 4×1 vector of infinitesimal actuated joint displacements. Based on the definition of the Jacobian, one has

$$\mathbf{J}_k \delta\mathbf{D} = \mathbf{K}_k \delta\boldsymbol{\rho}, \tag{5.10}$$

where the infinitesimal Cartesian displacement $\delta\mathbf{D}$ can be obtained as

$$\delta\mathbf{D} = \mathbf{J}_k^{-1} \mathbf{K}_k \delta\boldsymbol{\rho} \tag{5.11}$$

in which Jacobian $\mathbf{J}_k$ is invertible as long as the robot is not in a type II (parallel) singular configuration (Gosselin and Angeles, 1990). Substituting (5.11) into (5.9) and using the principle of virtual work — namely that the equation obtained must be verified for any value of vector $\delta\boldsymbol{\rho}$ — and rearranging the terms yields the inverse static equations

$$\mathbf{f} = (\mathbf{J}_k^{-1} \mathbf{K}_k)^T \mathbf{F}. \tag{5.12}$$

5.2.2 Redundantly Actuated

When a rigid object is grasped by the gripper, the angle γ — which is the angle between the two jaws (see Fig. 5.2) — cannot be further reduced. The robot becomes over-constrained and is no longer $(3+1)$-dof but has only three Cartesian degrees of freedom, which are $[\mathbf{p}^T \ \phi]^T$. The grasping force appears as an internal antagonistic force.

Jacobian matrices that are different from (5.4) and (5.5) can be established. The (constant) length of the RR link in each $\underline{\text{P}}$RR linkage can be written as

$$(\mathbf{p} - \mathbf{a}_i)^T (\mathbf{p} - \mathbf{a}_i) = u_i^2, \quad i = 1, 2 \tag{5.13}$$

$$(\mathbf{p}+\mathbf{Q}_\phi\mathbf{c}-\mathbf{a}_i)^T(\mathbf{p}+\mathbf{Q}_\phi\mathbf{c}-\mathbf{a}_i)=u_i^2,\quad i=3,4 \tag{5.14}$$

where $\mathbf{c}$ is a position vector pointing from point P to point S, expressed in the moving frame $Px'y'$ and is constant (since angle γ is constant).

Differentiating (5.13) and (5.14) with respect to time yields

$$\mathbf{u}_i^T(\dot{\mathbf{p}}-\dot{\rho}_i\mathbf{e}_1)=0,\quad i=1,2 \tag{5.15}$$

$$\mathbf{u}_i^T(\dot{\mathbf{p}}+\dot{\phi}\mathbf{E}\mathbf{Q}_\phi\mathbf{c}-\dot{\rho}_i\mathbf{e}_1)=0,\quad i=3,4 \tag{5.16}$$

where

$$\mathbf{u}_i=\mathbf{p}-\mathbf{a}_i,\quad i=1,2 \tag{5.17}$$

$$\mathbf{u}_i=\mathbf{p}+\mathbf{Q}_\phi\mathbf{c}-\mathbf{a}_i,\quad i=3,4 \tag{5.18}$$

and where

$$\dot{\mathbf{Q}}_\phi=\dot{\phi}\mathbf{E}\mathbf{Q}_\phi \tag{5.19}$$

in which matrix $\mathbf{E}$ is defined in (5.6).

The velocity equations are obtained by combining (5.15) and (5.16), which can be written as

$$\mathbf{J}_r\mathbf{t}=\mathbf{K}_r\dot{\boldsymbol{\rho}}. \tag{5.20}$$

The first two rows of Jacobians $\mathbf{J}_r$ and $\mathbf{K}_r$ are constructed by (5.15), while the last two rows are constructed by (5.16), leading to

$$\mathbf{J}_r=\begin{bmatrix}\mathbf{u}_1^T & 0\\ \mathbf{u}_2^T & 0\\ \mathbf{u}_3^T & \mathbf{u}_3^T\mathbf{E}\mathbf{Q}_\phi\mathbf{c}\\ \mathbf{u}_4^T & \mathbf{u}_4^T\mathbf{E}\mathbf{Q}_\phi\mathbf{c}\end{bmatrix} \tag{5.21}$$

and

$$\mathbf{K}_r=\begin{bmatrix}\mathbf{u}_1^T\mathbf{e}_1 & 0 & 0 & 0\\ 0 & \mathbf{u}_2^T\mathbf{e}_1 & 0 & 0\\ 0 & 0 & \mathbf{u}_3^T\mathbf{e}_1 & 0\\ 0 & 0 & 0 & \mathbf{u}_4^T\mathbf{e}_1\end{bmatrix}. \tag{5.22}$$

Matrix $\mathbf{J}_r$ is of dimension 4×3, while matrix $\mathbf{K}_r$ is of dimension 4×4. The actuation redundancy is apparent from matrix $\mathbf{J}_r$. Similarly to (5.11), the infinitesimal actuated joint displacements of the redundantly actuated robot can be obtained as

$$\delta\boldsymbol{\rho}=\mathbf{U}^T\delta\mathbf{D} \tag{5.23}$$

where $\mathbf{U}^T=\mathbf{K}_r^{-1}\mathbf{J}_r$ is of dimension 4×3 and in which matrix $\mathbf{K}_r$ is invertible as long as the robot is not in a type I (serial) singular configuration (Gosselin and Angeles, 1990). The

forward static equations are then obtained by substituting (5.23) into (5.9) and using the principle of virtual work to eliminate $\delta\mathbf{D}$ and rearranging the terms, leading to

$$\mathbf{F} = \mathbf{U}\mathbf{f} \tag{5.24}$$

where $\mathbf{F}$ is defined in (5.9). Therefore, the general solution for the actuator forces is obtained as

$$\mathbf{f} = \mathbf{U}^I\mathbf{F} - \zeta(\mathbf{I} - \mathbf{U}^I\mathbf{U})\frac{\partial\eta}{\partial\mathbf{f}}, \tag{5.25}$$

which consists of a minimum norm solution (which is $\mathbf{U}^I\mathbf{F}$) in addition with a term (which is $\zeta(\mathbf{I} - \mathbf{U}^I\mathbf{U})\frac{\partial\eta}{\partial\mathbf{f}}$) that belongs to the null space of matrix $\mathbf{J}_r^T$, and in which $\mathbf{U}^I$ is the Moore-Penrose inverse of $\mathbf{U}$, ζ is a scaling factor used to adjust the magnitude of the null space term, $\mathbf{I}$ is the identity matrix, and η is a performance index to be minimized. Equation (5.25) can be considered as an analogue of the general solution of the velocity equations of kinematically redundant robots (see, for instance (Gosselin and Schreiber, 2016)) in the static force domain.

The second term in (5.25) can be used to adjust the internal forces, e.g., the force applied to the right jaw by the grasped object (including the grasping force and the friction which are orthogonal and parallel to the plane of the right jaw, respectively), the force applied to the right jaw at point B by the left jaw, and the forces applied to the right jaw at point P by the associated two $\underline{\text{P}}$RR legs. Nevertheless, an explicit expression of the grasping force and actuator forces is not obtained from (5.25).

5.2.3 Non-redundant

Differently from the Cartesian coordinates defined in the previous subsections, the robot is now considered to be non-redundant and the generalized Cartesian coordinates are defined as a 4×1 vector, which is noted $\begin{bmatrix}\mathbf{b}^T & \phi & \beta\end{bmatrix}^T$. The whole gripper (including the left jaw) is regarded as the end-effector and the grasping force appears as an external force acting at the end-effector.

In addition to the local frame $Px'y'$ on the right jaw, another local frame is attached to the left jaw, denoted by $Sx''y''$, whose origin is at point S and the x''-axis is pointing from point S to point B. Four constraint equations, which are similar to (5.13) and (5.14) can be established as follows

$$(\mathbf{b} - \mathbf{Q}_\phi\mathbf{v}_1 - \mathbf{a}_i)^T(\mathbf{b} - \mathbf{Q}_\phi\mathbf{v}_1 - \mathbf{a}_i) = u_i^2, \quad i = 1, 2 \tag{5.26}$$

$$(\mathbf{b} - \mathbf{Q}_\beta\mathbf{v}_2 - \mathbf{a}_i)^T(\mathbf{b} - \mathbf{Q}_\beta\mathbf{v}_2 - \mathbf{a}_i) = u_i^2, \quad i = 3, 4 \tag{5.27}$$

where

$$\mathbf{Q}_\beta = \begin{bmatrix}\cos\beta & -\sin\beta \\ \sin\beta & \cos\beta\end{bmatrix} \tag{5.28}$$

is the orientation matrix of the local frame $Sx''y''$ with respect to the base frame, and $\mathbf{v}_2$ is written as

$$\mathbf{v}_2 = \begin{bmatrix} l & 0 \end{bmatrix}^T \tag{5.29}$$

which is a vector connecting point S to point B, expressed in the local frame $Sx''y''$.

The time derivatives of (5.26) and (5.27) can be written as

$$\mathbf{u}_i^T(\dot{\mathbf{b}} - \dot{\phi}\mathbf{E}\mathbf{Q}_\phi\mathbf{v}_1 - \dot{\rho}_i\mathbf{e}_1) = 0, \quad i = 1, 2 \tag{5.30}$$

$$\mathbf{u}_i^T(\dot{\mathbf{b}} - \dot{\beta}\mathbf{E}\mathbf{Q}_\beta\mathbf{v}_2 - \dot{\rho}_i\mathbf{e}_1) = 0, \quad i = 3, 4 \tag{5.31}$$

where matrix $\mathbf{E}$ is defined in (5.6) and where

$$\mathbf{u}_i = \mathbf{b} - \mathbf{Q}_\phi\mathbf{v}_1 - \mathbf{a}_i, \quad i = 1, 2 \tag{5.32}$$

$$\mathbf{u}_i = \mathbf{b} - \mathbf{Q}_\beta\mathbf{v}_2 - \mathbf{a}_i, \quad i = 3, 4. \tag{5.33}$$

The velocity equations are constructed by combining (5.30) and (5.31) and can be written as

$$\mathbf{J}_n\mathbf{t}_n = \mathbf{K}_n\dot{\boldsymbol{\rho}} \tag{5.34}$$

where $\mathbf{t}_n = [\dot{\mathbf{b}}\ \dot{\phi}\ \dot{\beta}]^T$, the Jacobian $\mathbf{J}_n$ is

$$\mathbf{J}_n = \begin{bmatrix} \mathbf{u}_1^T & -\mathbf{u}_1^T\mathbf{E}\mathbf{Q}_\phi\mathbf{v}_1 & 0 \\ \mathbf{u}_2^T & -\mathbf{u}_2^T\mathbf{E}\mathbf{Q}_\phi\mathbf{v}_1 & 0 \\ \mathbf{u}_3^T & 0 & -\mathbf{u}_3^T\mathbf{E}\mathbf{Q}_\beta\mathbf{v}_2 \\ \mathbf{u}_4^T & 0 & -\mathbf{u}_4^T\mathbf{E}\mathbf{Q}_\beta\mathbf{v}_2 \end{bmatrix} \tag{5.35}$$

and the Jacobian $\mathbf{K}_n$ is the same as Jacobian $\mathbf{K}_r$ defined in (5.22). These Jacobians are of dimension 4×4.

According to the duality of kinematics and statics, the forward static equations of the robot can be written in a similar form as (5.24), namely

$$\mathbf{F}_n = (\mathbf{K}_n^{-1}\mathbf{J}_n)^T\mathbf{f} \tag{5.36}$$

where vector $\mathbf{f}$ is defined in (5.9), and where

$$\mathbf{F}_n = \begin{bmatrix} \mathbf{f}_b^T & m_r & m_l \end{bmatrix}^T \tag{5.37}$$

is the generalized 4×1 vector of Cartesian force ($\mathbf{f}_b$) and moments (m_r and m_l). The Cartesian force $\mathbf{f}_b$ is applied to the environment by the robot at point B, while the Cartesian moments m_r and m_l are applied to the environment by the right and left jaws, respectively. As mentioned before, in this study it is not necessary to measure these terms directly. An approach for determining them is given as follows.

Consider the free-body diagram of the grasped object, which is represented schematically in Fig. 5.3. For this planar robot, the gravity is in the direction of the $-y$-axis. Each jaw exerts a

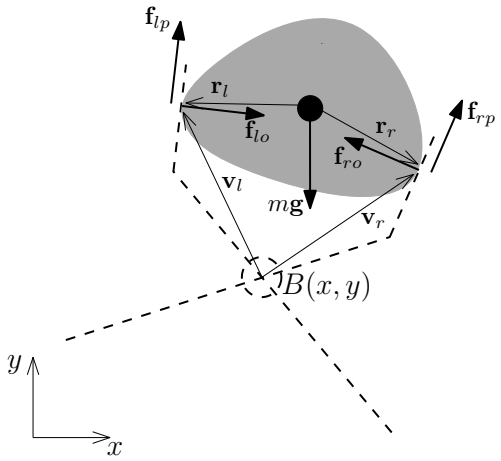

Figure 5.3 – Free-body diagram of the grasped object. The gripper is indicated by dashed lines.

force on the object, which can be decomposed into a component whose direction is orthogonal to the jaw ($\mathbf{f}_{lo}$ or $\mathbf{f}_{ro}$) and another component whose direction is parallel to the same jaw ($\mathbf{f}_{lp}$ or $\mathbf{f}_{rp}$), as illustrated in Fig. 5.3. The latter components are due to the friction between the jaws and the object, and we assume that they are large enough to prevent the object from sliding. Since the geometry of the object is assumed to be known a priori, the directions of these forces can be readily determined. Thus, only their magnitude will appear as unknowns, which can be measured using four load cells. However, this will lead to a complicated design of the gripper. In fact, if one of the four forces is measured by a load cell, the others can be computed from the three static equilibrium equations of the object, which contains two force equilibrium equations in the directions of the x- and y-axes of the base frame and one moment equilibrium equation with respect to the centre of mass of the object.

The force equilibrium equations can be combined into a vector form equation

$$\mathbf{f}_{ro} + \mathbf{f}_{rp} + \mathbf{f}_{lo} + \mathbf{f}_{lp} + m\mathbf{g} = \mathbf{0} \tag{5.38}$$

where m is the mass of the object, $\mathbf{g}$ is the gravitational acceleration vector, and $\mathbf{0}$ is a 2×1 zero vector. In addition, the moment equilibrium equation is written as

$$(\mathbf{E}\mathbf{r}_r)^T(\mathbf{f}_{ro} + \mathbf{f}_{rp}) + (\mathbf{E}\mathbf{r}_l)^T(\mathbf{f}_{lo} + \mathbf{f}_{lp}) = 0 \tag{5.39}$$

where matrix $\mathbf{E}$ is defined in (5.6), and $\mathbf{r}_r$ and $\mathbf{r}_l$ are the position vectors pointing from the centre of mass of the object to the contact point between this object and the right and left jaws, respectively (see Fig. 5.3). In practice, we measure the magnitude of $\mathbf{f}_{lo}$ or $\mathbf{f}_{ro}$, which will be explained in Section 5.5.

Once these forces are obtained, they can be converted to a corresponding force exerted by the robot at point B, which is $\mathbf{f}_b$; and two corresponding moments, which are m_r and m_l. The

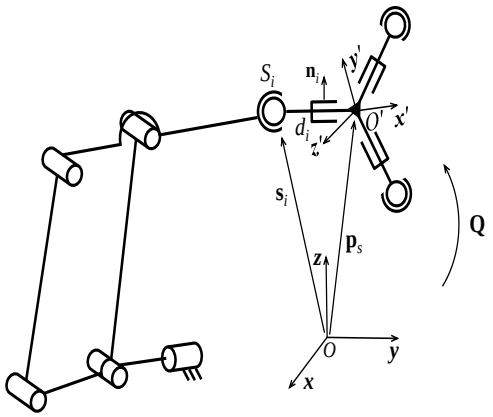

Figure 5.4 – Kinematic modelling of one leg of the 3-[R(RR-RRR)SP] robot.

converting equation is written as

$$\mathbf{F}_n = \mathbf{T}\mathbf{f}_{obj} \tag{5.40}$$

where

$$\mathbf{f}_{obj} = \begin{bmatrix} \mathbf{f}_{ro}^T & \mathbf{f}_{rp}^T & \mathbf{f}_{lo}^T & \mathbf{f}_{lp}^T \end{bmatrix}^T \tag{5.41}$$

which is of dimension 8×1, and $\mathbf{T}$ is the transformation matrix which is given by

$$\mathbf{T} = \begin{bmatrix} \mathbf{e}_1^T & \mathbf{e}_1^T & \mathbf{e}_1^T & \mathbf{e}_1^T \\ \mathbf{e}_2^T & \mathbf{e}_2^T & \mathbf{e}_2^T & \mathbf{e}_2^T \\ (\mathbf{E}\mathbf{v}_r)^T & (\mathbf{E}\mathbf{v}_r)^T & \mathbf{0}^T & \mathbf{0}^T \\ \mathbf{0}^T & \mathbf{0}^T & (\mathbf{E}\mathbf{v}_l)^T & (\mathbf{E}\mathbf{v}_l)^T \end{bmatrix} \tag{5.42}$$

which is of dimension 4×8, and in which $\mathbf{e}_1$ is defined in (5.2) while

$$\mathbf{e}_2 = \begin{bmatrix} 0 & 1 \end{bmatrix}^T, \tag{5.43}$$

$\mathbf{v}_r$ and $\mathbf{v}_l$ denote respectively the position vectors pointing from point B to the points of contact between the object with the right and left jaws (see Fig. 5.3), matrix $\mathbf{E}$ is defined in (5.6), and $\mathbf{0}$ is a 2×1 zero vector. Finally, the inverse static equations can be obtained as

$$\mathbf{f} = (\mathbf{J}_n^{-1}\mathbf{K}_n)^T\mathbf{F}_n. \tag{5.44}$$

5.3 Static Modelling of a Spatial Hybrid Parallel Robot

The static modelling of the spatial 3-[R(RR-RRR)SP] hybrid parallel robot shown in Fig. 2.9 is studied in this section. Here S and P respectively stand for a passive spherical joint and a passive prismatic joint. The kinematic modelling of one leg of the robot is schematically presented in Fig. 5.4, where $Oxyz$ is the fixed base frame while a moving frame $O'x'y'z'$ is attached to the platform in which the z'-axis is orthogonal to the plane formed by the prismatic joints, $\mathbf{n}_i$ (with $i = 1, 2, 3$) is a unit vector in the direction orthogonal to the ith

prismatic joint, $\mathbf{s}_i$ (with $i = 1, 2, 3$) is the position vector of point S_i, vector $\mathbf{p}_s$ and matrix $\mathbf{Q}$ represent the position vector and orientation matrix of the moving platform frame with respect to the base frame. Because the robot is driven by nine revolute actuators, the actuated joint variables of the inverse static equations (for instance, which is noted $\mathbf{f}$ in (5.12), (5.25), or (5.44)) of this spatial robot will be the motor torques.

5.3.1 Kinematically Redundant

In Chapter 2, the spatial hybrid parallel robot is considered to be kinematically redundant and is $(6+3)$-dof, where the six Cartesian degrees of freedom are the position of point O' and the orientation of the moving frame, while the additional three local degrees of freedom are the lengths of links S_iO', noted d_i, $i = 1, 2, 3$ (Wen and Gosselin, 2019). The velocity equations are similar to those of the architecture shown in Fig. 2.8 and can be written as

$$\mathbf{J}_{sk}\mathbf{t}_s = \mathbf{K}_{sk}\dot{\boldsymbol{\theta}}, \tag{5.45}$$

where the vectors of Cartesian and joint velocities are respectively written as

$$\mathbf{t}_s = [\dot{\mathbf{p}}_s^T \ \boldsymbol{\omega}^T]^T \tag{5.46}$$

and

$$\dot{\boldsymbol{\theta}} = [\dot{\boldsymbol{\theta}}_1^T \ \dot{\boldsymbol{\theta}}_2^T \ \dot{\boldsymbol{\theta}}_3^T]^T \tag{5.47}$$

with $\dot{\boldsymbol{\theta}}_i = [\dot{\theta}_{i1} \ \dot{\theta}_{i2} \ \dot{\theta}_{i3}]^T, i = 1, 2, 3$, and where the Jacobian matrices $\mathbf{J}_{sk}$ and $\mathbf{K}_{sk}$ are given as

$$\mathbf{J}_{sk} = \begin{bmatrix} \mathbf{n}_1^T\mathbf{Q}^T & [(\mathbf{s}_1 - \mathbf{p}_s) \times (\mathbf{Q}\mathbf{n}_1)]^T \\ \mathbf{q}_z^T & [(\mathbf{s}_1 - \mathbf{p}_s) \times \mathbf{q}_z]^T \\ \mathbf{n}_2^T\mathbf{Q}^T & [(\mathbf{s}_2 - \mathbf{p}_s) \times (\mathbf{Q}\mathbf{n}_2)]^T \\ \mathbf{q}_z^T & [(\mathbf{s}_2 - \mathbf{p}_s) \times \mathbf{q}_z]^T \\ \mathbf{n}_3^T\mathbf{Q}^T & [(\mathbf{s}_3 - \mathbf{p}_s) \times (\mathbf{Q}\mathbf{n}_3)]^T \\ \mathbf{q}_z^T & [(\mathbf{s}_3 - \mathbf{p}_s) \times \mathbf{q}_z]^T \end{bmatrix} \tag{5.48}$$

which is of dimension 6×6 and

$$\mathbf{K}_{sk} = \begin{bmatrix} \mathbf{n}_1^T\mathbf{Q}^T\mathbf{M}_1 & \mathbf{0}^T & \mathbf{0}^T \\ \mathbf{q}_z^T\mathbf{M}_1 & \mathbf{0}^T & \mathbf{0}^T \\ \mathbf{0}^T & \mathbf{n}_2^T\mathbf{Q}^T\mathbf{M}_2 & \mathbf{0}^T \\ \mathbf{0}^T & \mathbf{q}_z^T\mathbf{M}_2 & \mathbf{0}^T \\ \mathbf{0}^T & \mathbf{0}^T & \mathbf{n}_3^T\mathbf{Q}^T\mathbf{M}_3 \\ \mathbf{0}^T & \mathbf{0}^T & \mathbf{q}_z^T\mathbf{M}_3 \end{bmatrix} \tag{5.49}$$

which is of dimension 6×9 and where $\mathbf{0}$ is a 3×1 zero vector, $\mathbf{q}_z$ is a constant unit vector along the z'-axis, and $\mathbf{M}_i$ is a 3×3 Jacobian matrix of the ith $\underline{\mathrm{R}}(\underline{\mathrm{R}}\mathrm{R}\text{-}\underline{\mathrm{R}}\mathrm{RR})$ robot leg which is defined in (1.16). The kinematic redundancy is reflected in matrix $\mathbf{K}_{sk}$. The inverse static equations can be written in a form similar to that of (5.12).

5.3.2 Redundantly Actuated

The local degrees of freedom disappear because the moving platform and the prismatic joints are considered to be rigidly connected due to the grasped object, and the robot is over-constrained. Nine constraint equations can be established for the robot. Firstly, it can be observed that in the ith leg vector $\mathbf{s}_i - \mathbf{p}_s$ is always perpendicular to vectors $\mathbf{n}_i$ and $\mathbf{q}_z$, one can then write

$$(\mathbf{s}_i - \mathbf{p}_s)^T(\mathbf{Q}\mathbf{n}_i) = 0 \tag{5.50}$$

$$(\mathbf{s}_i - \mathbf{p}_s)^T\mathbf{q}_z = 0, \quad i = 1, 2, 3 \tag{5.51}$$

which are the same constraint equations used to develop the Jacobians given in (5.48) and (5.49). Secondly, the (constant) distance between points S_i and point O' can be written as

$$(\mathbf{s}_i - \mathbf{p}_s)^T(\mathbf{s}_i - \mathbf{p}_s) = d_i^2, \quad i = 1, 2, 3. \tag{5.52}$$

Differentiating (5.52) with respect to time yields

$$(\mathbf{s}_i - \mathbf{p}_s)^T\dot{\mathbf{p}}_s = (\mathbf{s}_i - \mathbf{p}_s)^T\dot{\mathbf{s}}_i, \quad i = 1, 2, 3 \tag{5.53}$$

where

$$\dot{\mathbf{s}}_i = \mathbf{M}_i\dot{\boldsymbol{\theta}}_i, \quad i = 1, 2, 3 \tag{5.54}$$

and where $\mathbf{M}_i$ is defined in (5.49). The velocity equations are constructed by rearranging the items in the equations of the time derivative of (5.50) and (5.51) and in (5.53)

$$\mathbf{J}_{sr}\mathbf{t}_s = \mathbf{K}_{sr}\dot{\boldsymbol{\theta}} \tag{5.55}$$

The Jacobians are given as

$$\mathbf{J}_{sr} = \begin{bmatrix} \mathbf{n}_1^T\mathbf{Q}^T & [(\mathbf{s}_1 - \mathbf{p}_s) \times (\mathbf{Q}\mathbf{n}_1)]^T \\ \mathbf{q}_z^T & [(\mathbf{s}_1 - \mathbf{p}_s) \times \mathbf{q}_z]^T \\ \mathbf{n}_2^T\mathbf{Q}^T & [(\mathbf{s}_2 - \mathbf{p}_s) \times (\mathbf{Q}\mathbf{n}_2)]^T \\ \mathbf{q}_z^T & [(\mathbf{s}_2 - \mathbf{p}_s) \times \mathbf{q}_z]^T \\ \mathbf{n}_3^T\mathbf{Q}^T & [(\mathbf{s}_3 - \mathbf{p}_s) \times (\mathbf{Q}\mathbf{n}_3)]^T \\ \mathbf{q}_z^T & [(\mathbf{s}_3 - \mathbf{p}_s) \times \mathbf{q}_z]^T \\ (\mathbf{s}_1 - \mathbf{p}_s)^T & \mathbf{0}^T \\ (\mathbf{s}_2 - \mathbf{p}_s)^T & \mathbf{0}^T \\ (\mathbf{s}_3 - \mathbf{p}_s)^T & \mathbf{0}^T \end{bmatrix} \tag{5.56}$$

which is of dimension 9×6 and

$$\mathbf{K}_{sr} = \begin{bmatrix} \mathbf{n}_1^T\mathbf{Q}^T\mathbf{M}_1 & \mathbf{0}^T & \mathbf{0}^T \\ \mathbf{q}_z^T\mathbf{M}_1 & \mathbf{0}^T & \mathbf{0}^T \\ \mathbf{0}^T & \mathbf{n}_2^T\mathbf{Q}^T\mathbf{M}_2 & \mathbf{0}^T \\ \mathbf{0}^T & \mathbf{q}_z^T\mathbf{M}_2 & \mathbf{0}^T \\ \mathbf{0}^T & \mathbf{0}^T & \mathbf{n}_3^T\mathbf{Q}^T\mathbf{M}_3 \\ \mathbf{0}^T & \mathbf{0}^T & \mathbf{q}_z^T\mathbf{M}_3 \\ (\mathbf{s}_1 - \mathbf{p}_s)^T\mathbf{M}_1 & \mathbf{0}^T & \mathbf{0}^T \\ \mathbf{0}^T & (\mathbf{s}_2 - \mathbf{p}_s)^T\mathbf{M}_2 & \mathbf{0}^T \\ \mathbf{0}^T & \mathbf{0}^T & (\mathbf{s}_3 - \mathbf{p}_s)^T\mathbf{M}_3 \end{bmatrix} \tag{5.57}$$

which is of dimension 9×9. The actuation redundancy is reflected in matrix $\mathbf{J}_{sr}$. The resolution of the actuator torques can be obtained in a manner similar to (5.25).

5.3.3 Non-redundant

If the robot is considered to be non-redundant, a 9×1 vector of generalized Cartesian degrees of freedom can be defined which comprises the position of point O', the orientation of the platform frame, and the three local degrees of freedom (the length of the prismatic joints). The generalized Cartesian velocities can then be defined as a 9×1 vector, namely, $\mathbf{t}_{sn} = [\dot{\mathbf{p}}_s{}^T\ \boldsymbol{\omega}^T\ \dot{d}_1\ \dot{d}_2\ \dot{d}_3]^T$. Nine constraint equations which are the same as (5.50), (5.51) and (5.52) can be established. Since this time $d_i, i = 1, 2, 3$ will appear as variables, the time derivative of (5.52) becomes

$$(\mathbf{s}_i - \mathbf{p}_s)^T\dot{\mathbf{p}}_s + d_i\dot{d}_i = (\mathbf{s}_i - \mathbf{p}_s)^T\dot{\mathbf{s}}_i, \quad i = 1, 2, 3. \tag{5.58}$$

Rearranging the items in the equations of the time derivative of (5.50) and (5.51) and in (5.58), one can obtain

$$\mathbf{J}_{sn}\mathbf{t}_{sn} = \mathbf{K}_{sn}\dot{\boldsymbol{\theta}} \tag{5.59}$$

where the Jacobian $\mathbf{J}_{sn}$ is constructed as

$$\mathbf{J}_{sn} = \begin{bmatrix} \mathbf{n}_1^T\mathbf{Q}^T & [(\mathbf{s}_1 - \mathbf{p}_s) \times (\mathbf{Q}\mathbf{n}_1)]^T & \mathbf{0}^T \\ \mathbf{q}_z^T & [(\mathbf{s}_1 - \mathbf{p}_s) \times \mathbf{q}_z]^T & \mathbf{0}^T \\ \mathbf{n}_2^T\mathbf{Q}^T & [(\mathbf{s}_2 - \mathbf{p}_s) \times (\mathbf{Q}\mathbf{n}_2)]^T & \mathbf{0}^T \\ \mathbf{q}_z^T & [(\mathbf{s}_2 - \mathbf{p}_s) \times \mathbf{q}_z]^T & \mathbf{0}^T \\ \mathbf{n}_3^T\mathbf{Q}^T & [(\mathbf{s}_3 - \mathbf{p}_s) \times (\mathbf{Q}\mathbf{n}_3)]^T & \mathbf{0}^T \\ \mathbf{q}_z^T & [(\mathbf{s}_3 - \mathbf{p}_s) \times \mathbf{q}_z]^T & \mathbf{0}^T \\ (\mathbf{s}_1 - \mathbf{p}_s)^T & \mathbf{0}^T & d_1\mathbf{e}_{s1}^T \\ (\mathbf{s}_2 - \mathbf{p}_s)^T & \mathbf{0}^T & d_2\mathbf{e}_{s2}^T \\ (\mathbf{s}_3 - \mathbf{p}_s)^T & \mathbf{0}^T & d_3\mathbf{e}_{s3}^T \end{bmatrix} \tag{5.60}$$

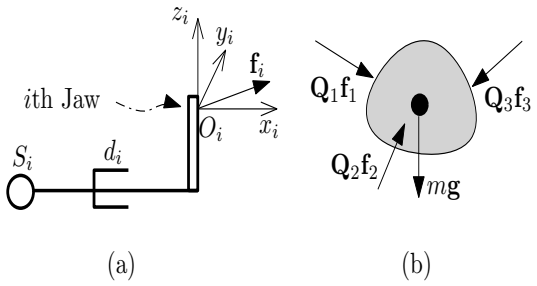

Figure 5.5 – (a) The force applied to the object by the ith jaw, expressed in the jaw frame. (b) Free-body diagram of the object.

which is of dimension 9×9 and in which $\mathbf{e}_{si}, i = 1, 2, 3$ are respectively

$$\mathbf{e}_{s1} = \begin{bmatrix} 1 \\ 0 \\ 0 \end{bmatrix}, \quad \mathbf{e}_{s2} = \begin{bmatrix} 0 \\ 1 \\ 0 \end{bmatrix}, \quad \mathbf{e}_{s3} = \begin{bmatrix} 0 \\ 0 \\ 1 \end{bmatrix}, \tag{5.61}$$

and Jacobian $\mathbf{K}_{sn}$ is the same as the Jacobian $\mathbf{K}_{sr}$ defined in (5.57). The inverse static equations can be written in a manner similar to (5.44).

However, in order to implement the inverse static equations, the 9×1 vector of generalized Cartesian force and moment, noted $\mathbf{F}_{sn}$, should be determined first. Similarly to the planar robot studied in the preceding section, a procedure for calculating $\mathbf{F}_{sn}$ based on the forces applied to the object by the jaws is developed, as detailed below.

As it can be seen in Fig. 5.5a, a local jaw frame $O_i x_i y_i z_i, i = 1, 2, 3$ is attached to the ith jaw, in which the x_i-axis is along the ith prismatic joint and is pointing from point S_i to point O', and the z_i-axis is in the same direction of the z'-axis. The force applied to the object by the ith jaw is noted $\mathbf{f}_i = f_{x_i}\mathbf{e}_{s1} + f_{y_i}\mathbf{e}_{s2} + f_{z_i}\mathbf{e}_{s3}$, expressed in the ith jaw frame. The free-body diagram of the grasped object is shown in Fig. 5.5b. The rotation matrix $\mathbf{Q}_i$ (with $i = 1, 2, 3$) — the orientation matrix of the ith jaw frame with respect to the base frame — maps the force $\mathbf{f}_i$ to the base frame. Because the orientation of the ith local jaw frame $O_i x_i y_i z_i$ with respect to the moving frame $O' x' y' z'$ is constant, it is quite straightforward to determine matrix $\mathbf{Q}_i$. This is to say, the directions of the forces acting at the object are readily obtained. Thus, only the magnitude of f_{x_i}, f_{y_i} and $f_{z_i}, i = 1, 2, 3$ is unknown. In fact, the components $f_{x_i}, i = 1, 2, 3$ are the grasping forces to be controlled, and will be measured directly. This is easily achieved in the final design by having a load cell in each jaw and aligning the measurement direction with the x_i-axis.

Consider now the six remaining unknown components f_{y_i} and $f_{z_i}, i = 1, 2, 3$. A system of six equilibrium equations can be established for the object, which contains three force equilibrium equations in each of the axes of the base frame, in addition with three moment equilibrium equations (expressed in the base frame) with respect to the centre of mass of the object.

Thereby, these six unknowns are readily obtained from these equilibrium equations. The detailed derivations are not shown here since the calculation is quite straightforward.

It can be observed, from the vector of the generalized Cartesian velocities, $\mathbf{t}_{sn}$, that the vector of the generalized Cartesian forces and moments, $\mathbf{F}_{sn}$, should be in the following form

$$\mathbf{F}_{sn} = \begin{bmatrix} \mathbf{f}_{O'}^T & \mathbf{m}^T & f_{x_1} & f_{x_2} & f_{x_3} \end{bmatrix}^T \tag{5.62}$$

where $\mathbf{f}_{O'}$ a 3×1 vector of Cartesian force acting at the point O', $\mathbf{m}$ is a 3×1 vector of Cartesian moment acting at the moving platform, and the scalar f_{xi} (with $i = 1, 2, 3$) is the magnitude of the first component of $\mathbf{f}_i$. The term $\mathbf{f}_{O'}$ is composed by the last two components of $\mathbf{f}_i, i = 1, 2, 3$, namely

$$\mathbf{f}_{O'} = \sum_{i=1}^{3} \mathbf{Q}_i (f_{y_i} \mathbf{e}_{s2} + f_{z_i} \mathbf{e}_{s3}), \quad i = 1, 2, 3. \tag{5.63}$$

And the term $\mathbf{m}$ is written as

$$\mathbf{m} = \sum_{i=1}^{3} (\mathbf{w}_i \times (\mathbf{Q}_i \mathbf{f}_i)), \quad i = 1, 2, 3 \tag{5.64}$$

which is contributed by forces $\mathbf{f}_1$, $\mathbf{f}_2$ and $\mathbf{f}_3$, and vector $\mathbf{w}_i$ is pointing from point O' to point O_i, expressed in the base frame and can be readily predetermined since the geometry of the object is known.

A matrix form equation similar to (5.40) can be obtained by combining and rearranging the terms in (5.63) and (5.64)

$$\begin{bmatrix} \mathbf{f}_{O'} \\ \mathbf{m} \end{bmatrix} = \mathbf{T}_s \mathbf{f}_{s,obj} \tag{5.65}$$

where

$$\mathbf{f}_{s,obj} = \begin{bmatrix} \mathbf{f}_1^T & \mathbf{f}_2^T & \mathbf{f}_3^T \end{bmatrix}^T, \tag{5.66}$$

and where the transformation matrix $\mathbf{T}_s$ is written as

$$\mathbf{T}_s = \begin{bmatrix} \mathbf{Q}_1 \mathbf{E}_s & \mathbf{Q}_2 \mathbf{E}_s & \mathbf{Q}_3 \mathbf{E}_s \\ \mathbf{W}_1 \mathbf{Q}_1 & \mathbf{W}_2 \mathbf{Q}_2 & \mathbf{W}_3 \mathbf{Q}_3 \end{bmatrix} \tag{5.67}$$

which is of dimension 6×9, and in which matrix $\mathbf{E}_s$ is defined as

$$\mathbf{E}_s = \begin{bmatrix} \mathbf{0} & \mathbf{e}_{s2} & \mathbf{e}_{s3} \end{bmatrix}, \tag{5.68}$$

where $\mathbf{0}$ is a 3×1 zero vector, and $\mathbf{W}_i$ (with $i = 1, 2, 3$) is the skew-symmetric matrix composed by the components of the vector $\mathbf{w}_i$, namely $\mathbf{W}_i \equiv \mathbf{w}_i \times$. The procedure for determining the transformation matrix $\mathbf{T}_s$ described above is readily applied to the planar and other spatial kinematically redundant hybrid parallel robots proposed in Chapter 2.

Once $\mathbf{F}_{sn}$ is determined, the vector of actuator torques is obtained utilising the inverse static equations, thereby completing the static modelling.

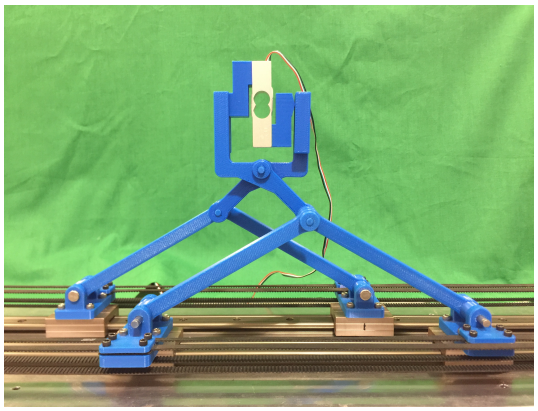

Figure 5.6 – A setup of the prototype of the proposed planar robot with a load cell.

5.4 Summary of the Static Modelling

As it can be observed, from the kinematically redundant inverse static equations (see, for instance (5.12)) of the planar or spatial robot, a vector of actuated joint forces or torques can be determined in order to balance the Cartesian force and moment. However, since the left jaw of the gripper of the planar robot, or each of the jaws of the gripper of the spatial robot, is considered to be a link of the corresponding leg rather than a part of the end-effector, the inverse static equations hold only when no external force or moment acting at the left jaw of the planar robot, or at any of the jaws of the spatial robot. However, this situation is unrealistic in practice, as it can be observed from Figs. 5.3 and 5.5. The situation is the same for the redundantly actuated counterpart because the Cartesian degrees of freedom of these two types of redundancies are identical. Therefore, the static equations (5.12) and (5.25) are insufficient to pursue the grasping force control.

It can be observed that only the non-redundant static model is well suited for grasping force control. In the following section, experiments are carried out based on a prototype of the planar robot shown in Fig. 5.2 to verify the effectiveness of this static model.

5.5 Experiments

A set up of the planar parallel grasping robot is shown in Fig. 5.6. Instead of a prismatic actuator, a motor coupled with a timing belt is used to actuate each of the prismatic joints. Each actuator consists of a RE-max 24, graphite brushes, 11 Watt motor, a MR type M, $128-512$ CPT, 2/3 channels encoder, and a planetary gearhead GP 22C, $0.5-2.0$ Nm, all from Maxon. The force sensor is a 3133 - micro load cell $(0-5\text{kg})$ - CZL635.

The vector of actuator torques can be obtained as

$$\boldsymbol{\tau} = \frac{r}{N}\mathbf{f} \tag{5.69}$$

where $r = 4.5$ mm is the radius of the output shaft (connecting to the timing belt) of each of the actuator transmissions, $N = 29$ is the reduction of each of the gearheads, and $\mathbf{f}$ is a vector of the tensions of all of the timing belts which is defined in (5.44).

The grasped object consists of a load cell and two brackets (between the load cell and the two jaws, see Fig. 5.6). The dimensions of the brackets are designed so that the two jaws are always parallel to each other and the forces $\mathbf{f}_{lo}$ and $\mathbf{f}_{ro}$ (see Fig. 5.3) that are applied to the grasped object by the jaws pass through the geometric centre of the load cell but in opposite directions.

The geometric parameters of the prototype are given as

$$\begin{aligned} u_i &= 120 \text{ mm}, \quad i = 1, \ldots, 4, \\ b &= l = 42.4 \text{ mm}, \\ d &= 42.7 \text{ mm}, \quad h = 42.5 \text{ mm}. \end{aligned}$$

where d is the distance between the two parallel jaws, and h is the distance between the geometric centre of the load cell and the centre of the pivot connecting the two jaws. With the given length of b and l, the corresponding two links (which are respectively along vectors $\mathbf{v}_1$ and $\mathbf{v}_2$) will always be orthogonal to each other when the object is grasped.

The rotational capability of the robot is unlimited (Gosselin et al., 2015), which indicates that the motion range of angle ϕ (and angle β) is $[0,\ 2\pi]$. As the robot rotates, the magnitude of forces $\mathbf{f}_{lo}$ and $\mathbf{f}_{ro}$, which are respectively noted f_{lo} and f_{ro}, might be different due to the weight of the grasped object, $m\mathbf{g}$ (see Fig. 5.3). It can be observed from Fig. 5.6 and the geometric parameters of the robot that if $\phi = \frac{\pi}{4}$ or $-\frac{3\pi}{4}$, the direction of $m\mathbf{g}$ is parallel to both jaws. In these configurations, the magnitude of the measured grasping force, which is noted $f_{g,m}$, is equal to both f_{lo} and f_{ro}. Otherwise, there will always be a component of $m\mathbf{g}$ acting on one of the jaws, in which case $f_{g,m}$ is equal to the magnitude of the force of the corresponding jaw, which is not affected by $m\mathbf{g}$. These relationships can be expressed as

$$\begin{cases} f_{g,m} = f_{lo} = f_{ro}, & \text{if } \ \phi = \frac{\pi}{4} \text{ or } -\frac{3\pi}{4} \\ f_{g,m} = f_{lo}, & \text{if } \ -\frac{3\pi}{4} < \phi < \frac{\pi}{4} \\ f_{g,m} = f_{ro}, & \text{otherwise} \end{cases} \tag{5.70}$$

which is used to specify the measured force when solving the static equilibrium equations (5.38) and (5.39).

Experiments are conducted with respect to a given initial configuration of the robot, which is defined as

$$\begin{aligned} \rho_2 - \rho_1 = \rho_4 - \rho_3 &= 207.8 \text{ mm}, \\ \phi = \frac{\pi}{4}, \quad \beta &= \phi + \frac{\pi}{2}. \end{aligned} \tag{5.71}$$

In this configuration, the height of the pivot connecting the two jaws is 90 mm. The desired grasping force, noted as $f_{g,d}$, is set to 2 N, which is large enough to prevent the grasped object from sliding.

Three control schemes of the grasping force are proposed and will be validated, namely, *i*): gripper position control; *ii*): grasping force control without force feedback; and *iii*): combined position and grasping force control with force feedback. The first two schemes are indirect force control schemes, in which the measured grasping force is not included in the control loop. The last two schemes are established based on the non-redundant static model of the robot. It is expected that the third scheme will be the most robust and that it can guarantee that a desired grasping force is always achieved.

5.5.1 Scheme *i*): Gripper Position Control

In this experiment, a grasping force is generated by specifying a value of angle γ smaller than the grasped object. Because in practice, angle γ can never reach the specified magnitude due to the large stiffness of the grasped object, position errors in actuators are generated. Then, a closed-loop proportional-derivative (PD) joint position controller is exploited in order to produce a torque in each of the actuators to result in the grasping force. An integral controller is not recommended because the actuated joint errors will be continuously accumulated, which may eventually make the robot unstable (wind-up phenomenon).

The inverse kinematic analysis provided in (Gosselin et al., 2015) indicates that each of the jaws can be reoriented through the $\underline{\text{P}}$RR legs connecting to the jaw, without changing the position of point B and the orientation of the other jaw. This is to say, angle γ can be adjusted by reorienting the left, or right, or both jaws. For the sake of brevity, in this experiment, we only consider that angle γ is virtually reduced by trying to reorient the right jaw (increasing angle ϕ). In fact, it has been verified that similar grasping force responses can be obtained in spite of the ways of achieving a specified γ.

Results of the grasping forces for different input values of ϕ for the given initial configuration of the robot are shown in Fig. 5.7. It can be observed that the relationship between the input values of ϕ and the measured grasping forces is almost linear. In fact, this relationship can be fitted as a linear function by taking sufficiently many samples, e.g.,

$$f_{g,m} = ke_{\phi} \tag{5.72}$$

where e_{ϕ} is the angle error between the real and specified values of ϕ, and k is a constant. Equation (5.72) shows that the grasping system under this control scheme is similar to a torsion spring with constant stiffness. Using (5.72), a grasping force of 2 N can be produced approximately by properly choosing the error of angle ϕ. However, the relationship between $f_{g,m}$ and e_{ϕ} is configuration and controller gains dependent, and it is not guaranteed that a linear function is obtained throughout the workspace of the robot, which makes it difficult

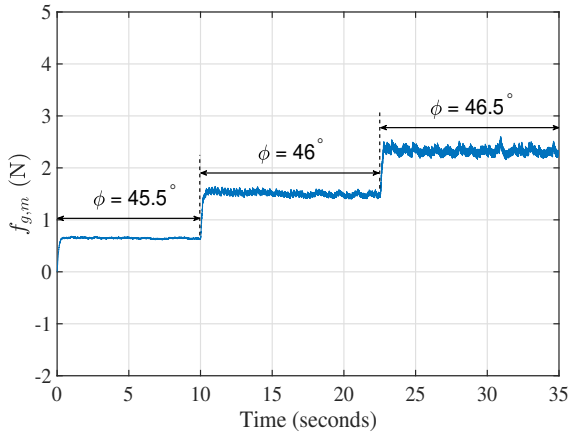

Figure 5.7 – Grasping forces of the control scheme i) for different values of ϕ.

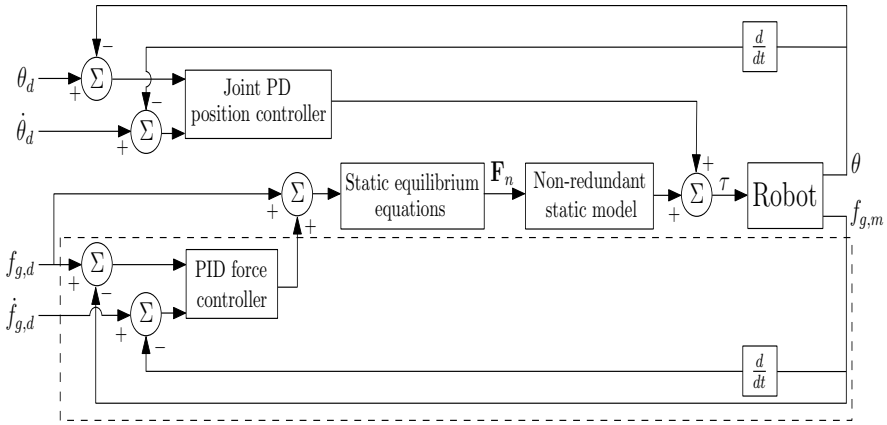

Figure 5.8 – Block diagram of the combined position and grasping force controller. In control scheme ii), the force feedback loops shown in the dotted box are excluded.

to predict the desired e_ϕ. Thereby, this control scheme is less effective for the control of the grasping force.

5.5.2 Scheme ii): Grasping Force Control without Force Feedback

If the non-redundant static model precisely describes the planar robot, a desired grasping force can be reached by simply applying an open-loop controller with the vector of actuator torques, $\boldsymbol{\tau}$, specified using (5.44) and (5.69), without causing any motions of the robot. However, in practice, there will always be a modelling error mainly due to the unknown friction in the actuator's gearing. Therefore, directly applying (5.44) and (5.69) may result in actuator torques that are different from the desired ones and make the robot unstable. Hence, we suggest an additional closed-loop PD joint position controller to ensure that the robot is always in the desired configuration. The block diagram of this control scheme is shown in Fig. 5.8 without the force feedback loops inside the dotted box.

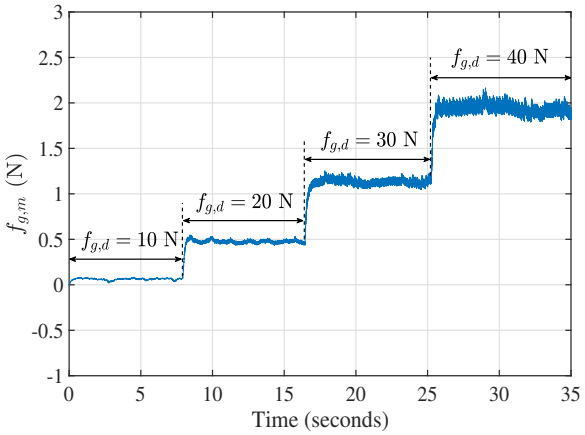

Figure 5.9 – Grasping forces of the control scheme *ii*) for different input values of $f_{g,d}$.

The measured grasping forces with respect to several different desired grasping forces for the given initial configuration of the robot are shown in Fig. 5.9. Although the inertial force due to the moving links and the gravity effect can be neglected (the total mass of the robot is quite small), because of the significant friction in the gear transmission of the motors, the output torques of the actuators are generally not identical to — which are, in fact, much lower than — the desired ones computed from the non-redundant static model. As a consequence, the measured grasping force is much lower than the corresponding input reference (see Fig. 5.9). Similarly to the case studied in the preceding subsection, a mapping between $f_{g,m}$ and $f_{g,d}$ can be determined which allows to approximately control the desired grasping force. Nevertheless, this control scheme is still inefficient due to the same limitations of control scheme *i*), namely the mapping depends on the configuration and controller gains. A possible approach to improve the effectiveness of this control scheme is to use direct drive motors (no gear friction), which is part of our future work.

5.5.3 Scheme *iii*): Combined Position and Grasping Force Control

In order to overcome the drawback of the control scheme *ii*), an additional closed-loop proportional-integral-derivative (PID) force controller is introduced to compose a combined position and grasping force control system (see, Fig. 5.8). The input term $\dot{f}_{g,d}$ is set to zero because a constant controlled grasping force is expected. The step response when the robot is in the initial configuration is shown in Fig. 5.10 with properly chosen PID gains. It clearly demonstrates that the force response is fast and stable, and the noise is effectively suppressed compared with the results given in Figs. 5.7 and 5.9.

The capability of this control scheme during motions of the robot (with initial configuration defined in (5.71)) is verified using the following three trajectories

$$x = 20\sin(t),\ y = 90,\ \phi = \frac{\pi}{4},\ \beta = \frac{3\pi}{4} \tag{5.73}$$

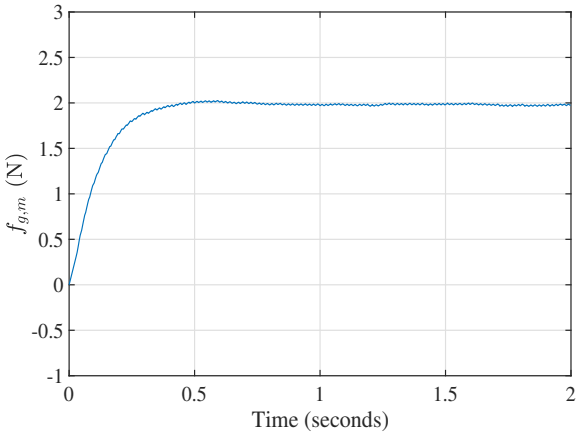

Figure 5.10 – Step response of the grasping force of the control scheme *iii*).

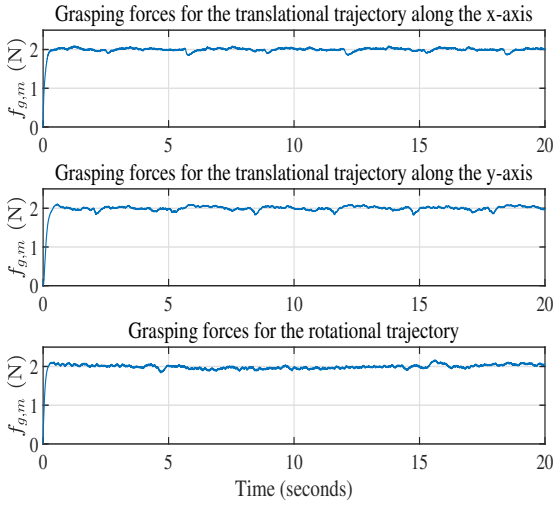

Figure 5.11 – Grasping forces for the given trajectories.

$$y = 20\sin(t) + 90,\ x = 0,\ \phi = \frac{\pi}{4},\ \beta = \frac{3\pi}{4} \tag{5.74}$$

$$\phi = \frac{\pi}{18}\sin(0.3t) + \frac{\pi}{4},\ \beta = \phi + \frac{\pi}{2},\ x = 0,\ y = 90 \tag{5.75}$$

with

$$0\text{ s} \leq t \leq 20\text{ s} \tag{5.76}$$

which are, respectively, translations along the x-axis and along the y-axis, and a rotation around the axis of the pivot connecting the two jaws. The units of x and y are millimeter and of ϕ and β are radian. The results are shown in Fig. 5.11, where the signals are noisier than that shown in Fig. 5.10, which is due to the inertial effect of the load cell (whose weight is much larger than each of the links of the robot) during motions. Also, we found that the grasping force is more likely to be affected by the inertia of the load cell during the rotational trajectory. Thus, we choose a smaller angular frequency (here 0.3 rad/s) in order to reduce

the magnitude of the Cartesian angular acceleration $\ddot{\phi}$ (and $\ddot{\beta}$) for the rotational trajectory. Nevertheless, the values of $f_{g,m}$ shown in Fig. 5.11 indicate that the combined position and grasping force controller is quite effective.

5.6 Multimedia Material

In addition to the results given in subsection 5.5.3, a video on the experiment provided in the same subsection accompanies this chapter. In the video, the effectiveness of the proposed non-redundant static model as well as the combined position and grasping force controller is demonstrated. The video can be found from: https://www.youtube.com/watch?v=TmsC61CAr4g&feature=youtu.be.

5.7 Conclusion

In this chapter, we showed that the type of redundancy of a class of kinematically redundant parallel and hybrid parallel robots with remotely operated gripper can also be actuation redundant or non-redundant. Three different static models corresponding to each of the types of redundancy were developed for two architectures. It was analysed that only the non-redundant static model is feasible for preforming grasping force control. Experimental results for a planar parallel grasping robot based on a combined position and grasping force controller are obtained and compared with those obtained from two other indirect control schemes. It was shown that the combined position and grasping force control scheme is more effective and stable. This study indicated that the kinematically redundant parallel grasping robots are capable for a variety of tasks, e.g., pick-and-place or assembly, where the grasped object is sensitive to the grasping force. Future work includes applying the grasping force controlled parallel grasping robots studied in this chapter to industry and implementing the proposed grasping force control approach in other novel kinematically redundant parallel robots with remotely operated gripper.

Conclusion

This thesis has presented a methodology for synthesizing kinematically redundant hybrid parallel robots (KRHPRs), and provided several results on kinematic analysis and grasping force control of the proposed architectures.

The synthesis methodology is quite simple, which is based on three different redundant links and moving platform assembly arrangements, but yields many advantages of the synthesized KRHPRs over several other non-redundant and redundant parallel robots:

(i) The type II singularities are easily determined and avoidable, thereby the KRHPRs can produce a very large orientational workspace;

(ii) An analytical, consistent and conservative inverse kinematic solution is obtained, which is a desirable property for redundant parallel robots whose inverse kinematic problem is solved in general using numerical methods that may encounter the repeatability problem;

(iii) The forward kinematic problem of the KRHPRs can be solved much more easily than that of their non-redundant counterparts or many other redundant parallel robots using several of the proposed approaches for forward kinematic analysis;

(iv) The redundant coordinates can be controlled actively, which is utilised to optimise the workspace and joint trajectory;

(v) In most cases, the actuators can be placed on or close to the base to achieve very low inertia of the moving parts;

(vi) Large numbers of architectures can be obtained using the synthesis methodology;

(vii) Additional actuators are not required to operate the gripper on the moving platform, preserving the lightweight of the KRHPR, which allows the control of the grasping force using the static model without gravity compensation;

(viii) Most of the proposed KRHPRs are well suited for physical human-robot interaction applications due to the large orientational workspace, lightweight, and low-impedance.

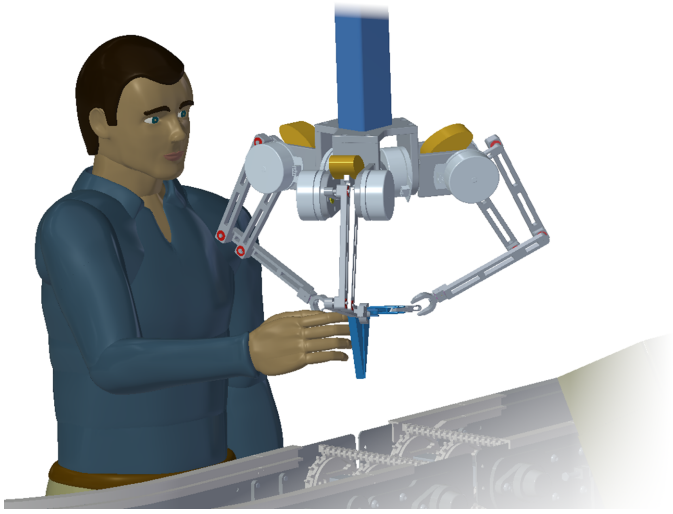

Figure 5.12 – Illustration of the intended use of the 3-[R(RR-RRR)SR] KRHPR in an upside down configuration (Wen et al., 2020).

Future work on kinematically redundant parallel and hybrid parallel robots includes:

(i) Development of new methodologies for synthesizing novel architectures that have simple structure, lightweight, and low-inertia (low-impedance);

(ii) Mount the proposed KRHPRs in an upside down configuration on a gantry robot (see, for example, Fig. 5.12) for the performance of typical industrial tasks requiring high dexterity and high-bandwidth.

The robots studied in this thesis belong to a subset of parallel robots. In addition to the future work mentioned above, several directions of research on parallel robots (non-redundant and redundant) that can be pursued in the near future include:

- **Implement the parallel robots in quadruped and humanoid robots.** For example, the R(RR-RRR) robot leg which contains a planar five-bar parallel mechanism of the 3-[R(RR-RRR)SR] KRHPR shown in Figure 5.12 is quite standard and widely used as the legs of quadruped robots. Although the second and third actuators are very close to the first one fixed on the body of the quadruped robot, the dynamic properties could be improved if the R(RR-RRR) linkage is replaced by an equivalent parallel robot that has the same mobility but with all actuators fixed on the base. The arms or legs of a humanoid robot could also be constructed using parallel mechanisms. For example, such an arm or leg could be assembled by mounting a three-degree-of-freedom rotational parallel mechanism — which is used as the wrist or ankle — on the distal link of the R(RR-RRR) linkage.

- **Intrinsically safe parallel robots with compliant links.** A possible approach that is reliable to keep the human user safe from unexpected collisions is to use compliant links in the parallel robots. A threshold of the deformation of each of the compliant links can be defined. The robot stops if the threshold is exceeded due to an unexpected collision. The design, modelling, and deformation measurement of the compliant links would be the key issues for implementing intrinsically safe parallel robots.

- **Micro parallel robots with conventional joints and actuators.** Different from many serial manipulators which contain several moving actuators, a large number of parallel robots have the potential to be built at the centimetre- or millimetre-scale because all of the actuators can be mounted on the base. At these scales, conventional joints and actuators can be used, which are widely used in the common size parallel robots (for example, the robots proposed in this thesis). It is anticipated that such parallel robots will exhibit many interesting features different from their macro counterparts and be suitable for micro pick-and-place and assembly tasks.

Appendix A

Velocity Equations of the R(RR-RRR) Robot Leg

Three constraint conditions can be determined for the R(RR-RRR) linkage contained in each leg. Firstly, $\mathbf{e}_{i2}$ (or $\mathbf{e}_{i3}$), the direction vector of the actuated joint $i2$ (or $i3$), is perpendicular to the vector $(\mathbf{s}_i - \mathbf{c}_i)$ (see Fig. 1.3). Thus, we have

$$\mathbf{e}_{i2}^T(\mathbf{s}_i - \mathbf{c}_i) = 0. \tag{A.1}$$

Differentiating (A.1) with respect to time yields

$$\dot{\mathbf{e}}_{i2}^T(\mathbf{s}_i - \mathbf{c}_i) + \mathbf{e}_{i2}^T\dot{\mathbf{s}}_i = 0 \tag{A.2}$$

where it is noted that $\mathbf{c}_i$ is a constant vector in the proposed mechanism. Since

$$\dot{\mathbf{e}}_{i2} = \boldsymbol{\omega}_{i2} \times \mathbf{e}_{i2} = \dot{\theta}_{i1}(\mathbf{e}_{i1} \times \mathbf{e}_{i2}), \tag{A.3}$$

then (A.2) can be rewritten as

$$\mathbf{e}_{i2}^T\dot{\mathbf{s}}_i = \dot{\theta}_{i1}(\mathbf{s}_i - \mathbf{c}_i)^T(\mathbf{e}_{i2} \times \mathbf{e}_{i1}). \tag{A.4}$$

The second constraint equation can be written as

$$\mathbf{v}_{i1}^T\mathbf{v}_{i1} = (\mathbf{s}_i - \mathbf{c}_i - \mathbf{u}_{i1})^T(\mathbf{s}_i - \mathbf{c}_i - \mathbf{u}_{i1}) = l_{i6}^2 \tag{A.5}$$

which can be rewritten as

$$(\mathbf{s}_i - \mathbf{c}_i)^T(\mathbf{s}_i - \mathbf{c}_i) - 2(\mathbf{s}_i - \mathbf{c}_i)^T\mathbf{u}_{i1} = l_{i6}^2 - l_{i4}^2 \tag{A.6}$$

in which

$$l_{i4}^2 = \mathbf{u}_{i1}^T\mathbf{u}_{i1}. \tag{A.7}$$

Differentiating (A.6) with respect to time yields

$$(\mathbf{s}_i - \mathbf{c}_i)^T \dot{\mathbf{s}}_i - \mathbf{u}_{i1}^T \dot{\mathbf{s}}_i - (\mathbf{s}_i - \mathbf{c}_i)^T \dot{\mathbf{u}}_{i1} = 0 \tag{A.8}$$

which can be rewritten as

$$(\mathbf{s}_i - \mathbf{c}_i - \mathbf{u}_{i1})^T \dot{\mathbf{s}}_i = (\mathbf{s}_i - \mathbf{c}_i)^T \dot{\mathbf{u}}_{i1}. \tag{A.9}$$

The time derivative of $\mathbf{u}_{i1}$ can be written as

$$\dot{\mathbf{u}}_{i1} = \boldsymbol{\omega}_{ui1} \times \mathbf{u}_{i1} = (\dot{\theta}_{i1}\mathbf{e}_{i1} + \dot{\theta}_{i2}\mathbf{e}_{i2}) \times \mathbf{u}_{i1}. \tag{A.10}$$

Substituting (A.10) into (A.9) yields

$$\mathbf{v}_{i1}^T \dot{\mathbf{s}}_i = (\mathbf{s}_i - \mathbf{c}_i)^T [\dot{\theta}_{i1}(\mathbf{e}_{i1} \times \mathbf{u}_{i1}) + \dot{\theta}_{i2}(\mathbf{e}_{i2} \times \mathbf{u}_{i1})]. \tag{A.11}$$

Since $\mathbf{s}_i - \mathbf{c}_i$, $\mathbf{e}_{i1}$ and $\mathbf{u}_{i1}$ are coplanar, one can write

$$(\mathbf{s}_i - \mathbf{c}_i)^T (\mathbf{e}_{i1} \times \mathbf{u}_{i1}) = 0. \tag{A.12}$$

Also

$$\begin{aligned} (\mathbf{s}_i - \mathbf{c}_i)^T (\mathbf{e}_{i2} \times \mathbf{u}_{i1}) &= (\mathbf{v}_{i1} + \mathbf{u}_{i1})^T (\mathbf{e}_{i2} \times \mathbf{u}_{i1}) \\ &= \mathbf{v}_{i1}^T (\mathbf{e}_{i2} \times \mathbf{u}_{i1}). \end{aligned} \tag{A.13}$$

Hence, (A.11) can be rewritten as

$$\mathbf{v}_{i1}^T \dot{\mathbf{s}}_i = \dot{\theta}_{i2} \mathbf{v}_{i1}^T (\mathbf{e}_{i2} \times \mathbf{u}_{i1}). \tag{A.14}$$

The third constraint equation can be written as

$$\mathbf{v}_{i2}^T \mathbf{v}_{i2} = (\mathbf{u}_{i1} + \mathbf{w}_i - \mathbf{u}_{i2})^T (\mathbf{u}_{i1} + \mathbf{w}_i - \mathbf{u}_{i2}) = l_{i3}^2. \tag{A.15}$$

where

$$\mathbf{w}_i = (1 - \frac{l_{i5}}{l_{i6}})\mathbf{v}_{i1} = (1 - \frac{l_{i5}}{l_{i6}})(\mathbf{s}_i - \mathbf{c}_i - \mathbf{u}_{i1}). \tag{A.16}$$

Differentiating (A.15) with respect to time yields

$$(\mathbf{u}_{i1} + \mathbf{w}_i - \mathbf{u}_{i2})^T (\dot{\mathbf{u}}_{i1} + \dot{\mathbf{w}}_i - \dot{\mathbf{u}}_{i2}) = 0 \tag{A.17}$$

which can be rewritten as

$$\mathbf{v}_{i2}^T (\dot{\mathbf{u}}_{i1} + \dot{\mathbf{w}}_i) = \mathbf{v}_{i2}^T \dot{\mathbf{u}}_{i2} \tag{A.18}$$

where

$$\dot{\mathbf{u}}_{i1} + \dot{\mathbf{w}}_i = \dot{\mathbf{u}}_{i1} + (1 - \frac{l_{i5}}{l_{i6}})(\dot{\mathbf{s}}_i - \dot{\mathbf{u}}_{i1}) = \frac{l_{i5}}{l_{i6}} \dot{\mathbf{u}}_{i1} + (1 - \frac{l_{i5}}{l_{i6}}) \dot{\mathbf{s}}_i \tag{A.19}$$

and similar to (A.10), $\dot{\mathbf{u}}_{i2}$ can be given as

$$\dot{\mathbf{u}}_{i2} = \boldsymbol{\omega}_{ui2} \times \mathbf{u}_{i2} = (\dot{\theta}_{i1}\mathbf{e}_{i1} + \dot{\theta}_{i3}\mathbf{e}_{i3}) \times \mathbf{u}_{i2}. \tag{A.20}$$

Substituting (A.19) and (A.20) into (A.18) then yields

$$\begin{aligned}&\mathbf{v}_{i2}^T[\frac{l_{i5}}{l_{i6}}(\dot{\theta}_{i1}(\mathbf{e}_{i1}\times\mathbf{u}_{i1})+\dot{\theta}_{i2}(\mathbf{e}_{i2}\times\mathbf{u}_{i1}))+(1-\frac{l_{i5}}{l_{i6}})\dot{\mathbf{s}}_i]\\&=\mathbf{v}_{i2}^T[\dot{\theta}_{i1}(\mathbf{e}_{i1}\times\mathbf{u}_{i2})+\dot{\theta}_{i3}(\mathbf{e}_{i3}\times\mathbf{u}_{i2})].\end{aligned}\tag{A.21}$$

The above equation can be simplified to

$$(1-\frac{l_{i5}}{l_{i6}})\mathbf{v}_{i2}^T\dot{\mathbf{s}}_i=\dot{\theta}_{i2}\frac{l_{i5}}{l_{i6}}\mathbf{v}_{i2}^T(\mathbf{u}_{i1}\times\mathbf{e}_{i2})+\dot{\theta}_{i3}\mathbf{v}_{i2}^T(\mathbf{e}_{i3}\times\mathbf{u}_{i2})\tag{A.22}$$

since $\mathbf{v}_{i2}$ is always perpendicular to $(\mathbf{e}_{i1}\times\mathbf{u}_{i1})$ and $(\mathbf{e}_{i1}\times\mathbf{u}_{i2})$.

Finally, the combination of (A.4), (A.14) and (A.22) gives

$$\mathbf{A}_i\dot{\mathbf{s}}_i=\mathbf{B}_i\dot{\boldsymbol{\theta}}_i\tag{A.23}$$

where matrices $\mathbf{A}_i$ and $\mathbf{B}_i$ are respectively shown in (1.10) and (1.11). Finally, the Jacobian matrix of the $\underline{\text{R}}(\underline{\text{RR}}\text{-}\underline{\text{RR}}\text{R})$ robot leg can be written as

$$\mathbf{M}_i=\mathbf{A}_i^{-1}\mathbf{B}_i\tag{A.1}$$

where one has

$$\mathbf{A}_i^{-1}=\alpha_i\begin{bmatrix}(\mathbf{v}_{i1}\times\mathbf{v}_{i2}) & -(\mathbf{e}_{i2}\times\mathbf{v}_{i2}) & \frac{l_{i6}}{l_{i6}-l_{i5}}(\mathbf{e}_{i2}\times\mathbf{v}_{i1})\end{bmatrix}\tag{A.2}$$

with

$$\alpha_i=\frac{1}{\mathbf{e}_{i2}^T(\mathbf{v}_{i1}\times\mathbf{v}_{i2})}.\tag{A.3}$$

Appendix B

Inverse Kinematics of the R(RR-RRR) Robot Leg

The inverse kinematic problem of the ith R(RR-RRR) robot leg is solved in two steps. Firstly, solve the inverse kinematics of the serial part of the leg, which contains the first link (link $i1$) and the links along vectors $\mathbf{u}_{i1}$ and $\mathbf{v}_{i1}$. This is straightforward and yields at most four different sets of solutions for θ_{i1} and θ_{i2}. Secondly, angle θ_{i3} is obtained. The vector loop equation of the 5-bar linkage included in the leg is written as

$$\mathbf{u}_{i1} + \mathbf{w}_i = \mathbf{u}_{i2} + \mathbf{v}_{i2} \tag{B.1}$$

where $\mathbf{w}_i$ is given in (A.16). One then obtains

$$\mathbf{v}_{i2} = \mathbf{r}_i - \mathbf{u}_{i2} \tag{B.2}$$

where $\mathbf{r}_i = \mathbf{u}_{i1} + \mathbf{w}_i$. The squared length of $\mathbf{v}_{i2}$ can be written as

$$\mathbf{v}_{i2}^T \mathbf{v}_{i2} = l_{i3}^2 = (\mathbf{r}_i - \mathbf{u}_{i2})^T (\mathbf{r}_i - \mathbf{u}_{i2}), \tag{B.3}$$

this is to say

$$2\mathbf{r}_i^T \mathbf{u}_{i2} + (l_{i3}^2 - l_{i2}^2 - \mathbf{r}_i^T \mathbf{r}_i) = 0 \tag{B.4}$$

where

$$l_{i2}^2 = \mathbf{u}_{i2}^T \mathbf{u}_{i2}. \tag{B.5}$$

Vector $\mathbf{u}_{i2}$ can be obtained as

$$\mathbf{u}_{i2} = \mathbf{Q}_i \mathbf{u}_{i2,l} \tag{B.6}$$

where $\mathbf{Q}_i$ is the rotation matrix corresponding to the orientation of the local frame located at the two revolute joints with coaxial axes — whose y-axis is in the opposite direction of the unit vectors $\mathbf{e}_{i2}$ and $\mathbf{e}_{i3}$ and whose z-axis is along the unit vector $\mathbf{e}_{i1}$ — with respect to the

base frame, $Oxyz$. It can be observed that matrix $\mathbf{Q}_i$ is a function of just the variable θ_{i1}. Also,

$$\mathbf{u}_{i2,l} = \begin{bmatrix} l_{i2}\cos\theta_{i3} \\ l_{i2}\sin\theta_{i3} \\ 0 \end{bmatrix} \tag{B.7}$$

is the vector, $\mathbf{u}_{i2}$, expressed in the above mentioned local frame. Substituting (B.6) and (B.7) into (B.4) leads to

$$2\mathbf{r}_i^T\mathbf{Q}_i\mathbf{e}_1 l_{i2}\cos\theta_{i3} + 2\mathbf{r}_i^T\mathbf{Q}_i\mathbf{e}_2 l_{i2}\sin\theta_{i3} + (l_{i3}^2 - l_{i2}^2 - \mathbf{r}_i^T\mathbf{r}_i) = 0 \tag{B.8}$$

in which

$$\mathbf{e}_1 = \begin{bmatrix} 1 \\ 0 \\ 0 \end{bmatrix}, \quad \mathbf{e}_2 = \begin{bmatrix} 0 \\ 1 \\ 0 \end{bmatrix}. \tag{B.9}$$

Equation (B.8) can be rewritten as

$$G_i\cos\theta_{i3} + H_i\sin\theta_{i3} + I_i = 0 \tag{B.10}$$

with

$$G_i = 2\mathbf{r}_i^T\mathbf{Q}_i\mathbf{e}_1 l_{i2} \tag{B.11}$$

$$H_i = 2\mathbf{r}_i^T\mathbf{Q}_i\mathbf{e}_2 l_{i2} \tag{B.12}$$

$$I_i = l_{i3}^2 - l_{i2}^2 - \mathbf{r}_i^T\mathbf{r}_i. \tag{B.13}$$

Applying the tangent half-angle formula to $\cos\theta_{i3}$ and $\sin\theta_{i3}$, one can then obtain

$$(I_i - G_i)T_i^2 + 2H_iT_i^2 + (I_i + G_i) = 0 \tag{B.14}$$

where

$$T_i = \tan\frac{\theta_{i3}}{2}. \tag{B.15}$$

Two different solutions can be obtained for θ_{i3} from (B.14) and at last a maximum number of eight different inverse kinematic solutions can be obtained for the $\underline{\text{R}}(\underline{\text{R}}\text{R-}\underline{\text{R}}\text{RR})$ robot leg.

Bibliography

A. Ajoudani, A. M. Zanchettin, S. Ivaldi, A. Albu-Schäffer, K. Kosuge, and O. Khatib. Progress and prospects of the human–robot collaboration. *Autonomous Robots*, 42(5):957–975, 2018.

S. Amine, M. T. Masouleh, S. Caro, P. Wenger, and C. Gosselin. Singularity analysis of 3T2R parallel mechanisms using Grassmann–Cayley algebra and Grassmann geometry. *Mechanism and Machine Theory*, 52:326–340, 2012.

J. Angeles, G. Yang, and I.-M. Chen. Singularity analysis of three-legged, six-DOF platform manipulators with URS legs. *IEEE/ASME transactions on mechatronics*, 8(4):469–475, 2003.

M. Arsenault and R. Boudreau. Synthesis of planar parallel mechanisms while considering workspace, dexterity, stiffness and singularity avoidance. *ASME Journal of Mechanical Design*, 128(1):69–78, 2006.

V. Babin and C. Gosselin. Picking, grasping, or scooping small objects lying on flat surfaces: A design approach. *The International Journal of Robotics Research*, 37(12):1484–1499, 2018.

V. Babin, D. St-Onge, and C. Gosselin. Stable and repeatable grasping of flat objects on hard surfaces using passive and epicyclic mechanisms. *Robotics and Computer-Integrated Manufacturing*, 55:1–10, 2019.

N. Badeau, C. Gosselin, S. Foucault, T. Laliberté, and M. E. Abdallah. Intuitive physical human–robot interaction: Using a passive parallel mechanism. *IEEE Robotics and Automation Magazine*, 25(2):28–38, 2018.

P. Ben-Horin and M. Shoham. Singularity condition of six-degree-of-freedom three-legged parallel robots based on Grassmann-Cayley algebra. *IEEE transactions on robotics*, 22(4): 577–590, 2006a.

P. Ben-Horin and M. Shoham. Singularity analysis of a class of parallel robots based on Grassmann–Cayley algebra. *Mechanism and Machine Theory*, 41(8):958–970, 2006b.

P. Ben-Horin and M. Shoham. Application of Grassmann–Cayley algebra to geometrical interpretation of parallel robot singularities. *The International Journal of Robotics Research*, 28(1):127–141, 2009.

I. Bonev. Delta parallel robot — the story of success. *Newsletter*, 2001. Available at `http://www.parallelmic.org`.

I. Bonev and C. M. Gosselin. Singularity loci of planar parallel manipulators with revolute joints. *2nd Workshop on Computational Kinematics*, pages 291–299, 2001.

I. A. Bonev, J. Ryu, S.-G. Kim, and S.-K. Lee. A closed-form solution to the direct kinematics of nearly general parallel manipulators with optimally located three linear extra sensors. *IEEE Transactions on Robotics and Automation*, 17(2):148–156, 2001.

I. A. Bonev, D. Zlatanov, and C. M. Gosselin. Advantages of the modified Euler angles in the design and control of PKMs. In *Parallel Kinematic Machines International Conference*, pages 199–215, 2002.

I. A. Bonev, D. Zlatanov, and C. M. Gosselin. Singularity analysis of 3-DOF planar parallel mechanisms via screw theory. *ASME Journal of Mechanical Design*, 125(3):573–581, 2003.

P. Cardou, S. Bouchard, and C. Gosselin. Kinematic-sensitivity indices for dimensionally nonhomogeneous Jacobian matrices. *IEEE Transactions on Robotics*, 26(1):166–173, 2010.

S. Caro, G. Moroz, T. Gayral, D. Chablat, and C. Chen. Singularity analysis of a six-dof parallel manipulator using Grassmann-Cayley algebra and Groebner bases. In *Brain, Body and Machine*, pages 341–352. Springer, 2010.

M. G. Catalano, G. Grioli, E. Farnioli, A. Serio, C. Piazza, and A. Bicchi. Adaptive synergies for the design and control of the Pisa/IIT softhand. *The International Journal of Robotics Research*, 33(5):768–782, 2014.

P. H. Chang. Analysis and control of robot manipulators with kinematic redundancy. 1987.

H. Cheng, Y.-K. Yiu, and Z. Li. Dynamics and control of redundantly actuated parallel manipulators. *IEEE/ASME Transactions on mechatronics*, 8(4):483–491, 2003.

Y.-J. Chiu and M.-H. Perng. Forward kinematics of a general fully parallel manipulator with auxiliary sensors. *The International Journal of Robotics Research*, 20(5):401–414, 2001.

R. Clavel. Device for the movement and positioning of an element in space, Dec. 11 1990. US Patent No. 4,976,582.

M. Conconi and M. Carricato. A new assessment of singularities of parallel kinematic chains. *IEEE Transactions on Robotics*, 25(4):757–770, 2009.

H. M. Daniali, P. Zsombor-Murray, and J. Angeles. Singularity analysis of planar parallel manipulators. *Mechanism and Machine Theory*, 30(5):665–678, 1995.

V. Duchaine and C. Gosselin. Safe, stable and intuitive control for physical human-robot interaction. In *2009 IEEE International Conference on Robotics and Automation*, pages 3383–3388. IEEE, 2009.

V. Duchaine and C. M. Gosselin. Investigation of human-robot interaction stability using Lyapunov theory. In *IEEE International Conference on Robotics and Automation*, pages 2189–2194. IEEE, 2008.

I. Ebert-Uphoff, J. Lee, and H. Lipkin. Characteristic tetrahedron of wrench singularities for parallel manipulators with three legs. *Proceedings of the Institution of Mechanical Engineers, Part C: Journal of Mechanical Engineering Science*, 216(1):81–93, 2002.

I. Ebrahimi, J. A. Carretero, and R. Boudreau. 3-PRRR redundant planar parallel manipulator: Inverse displacement, workspace and singularity analyses. *Mechanism and Machine Theory*, 42(8):1007–1016, 2007.

C. Gosselin and J. Angeles. The optimum kinematic design of a planar three-degree-of-freedom parallel manipulator. *ASME Journal of Mechanical Design*, 110(1):35–41, 1988.

C. Gosselin and J. Angeles. Singularity analysis of closed-loop kinematic chains. *IEEE Transactions on Robotics and Automation*, 6(3):281–290, 1990.

C. Gosselin and L.-T. Schreiber. Kinematically redundant spatial parallel mechanisms for singularity avoidance and large orientational workspace. *IEEE Transactions on Robotics*, 32(2):286–300, 2016.

C. Gosselin and L.-T. Schreiber. Redundancy in parallel mechanisms: A review. *Applied Mechanics Reviews*, 70(1):010802, 2018.

C. Gosselin, X. Kong, S. Foucault, and I. Bonev. A fully decoupled 3-dof translational parallel mechanism. In *Parallel Kinematic Machines in Research and Practice, 4th Chemnitz Parallel Kinematics Seminar*, pages 595–610, 2004.

C. Gosselin, F. Pelletier, and T. Laliberte. An anthropomorphic underactuated robotic hand with 15 dofs and a single actuator. In *2008 IEEE International Conference on Robotics and Automation*, pages 749–754. IEEE, 2008.

C. Gosselin, T. Laliberté, and A. Veillette. Singularity-free kinematically redundant planar parallel mechanisms with unlimited rotational capability. *IEEE Transactions on Robotics*, 31(2):457–467, 2015.

C. Gosselin, M. Isaksson, K. Marlow, and T. Laliberté. Workspace and sensitivity analysis of a novel nonredundant parallel scara robot featuring infinite tool rotation. *IEEE Robotics and Automation Letters*, 1(2):776–783, 2016.

C. M. Gosselin. The optimum design of robotic manipulators using dexterity indices. *Robotics and Autonomous systems*, 9(4):213–226, 1990.

C. M. Gosselin, J. Sefrioui, and M. J. Richard. Solutions polynomiales au problème de la cinématique directe des manipulateurs parallèles plans à trois degrés de liberté. *Mechanism and Machine Theory*, 27(2):107–119, 1992.

G. Grioli, M. Catalano, E. Silvestro, S. Tono, and A. Bicchi. Adaptive synergies: an approach to the design of under-actuated robotic hands. In *2012 IEEE/RSJ International Conference on Intelligent Robots and Systems*, pages 1251–1256. IEEE, 2012.

K. Han, W. Chung, and Y. Youm. New resolution scheme of the forward kinematics of parallel manipulators using extra sensors. *ASME Journal of Mechanical Design*, 118(2): 214–219, 1996.

J. Hesselbach and H. Kerle. Structurally adapted kinematic algorithms for parallel robots up to six degrees of freedom. *Proceedings of the IFToMM "Theory of Machines and Mechanisms*, pages 1930–1935, 1995.

J. M. Hollerbach. Optimum kinematic design for a seven degree of freedom manipulator. In *Robotics research: The second international symposium*, pages 215–222. Cambridge, MIT Press, 1985.

Z. Huang and Q. Li. Construction and kinematic properties of 3-UPU parallel mechanisms. In *ASME 2002 International Design Engineering Technical Conferences and Computers and Information in Engineering Conference*, pages 1027–1033, 2002.

Z. Huang, Y. Zhao, T. Zhao, et al. Advanced spatial mechanism. *China Higher Education Press, Beijing (in Chinese)*, 2006.

M. Husty. An algorithm for solving the direct kinematics of Stewart-Gough-type platforms. *McGill Centre Intell. Mach., McGill Univ., Montreal, QC, Canada, Res. Rep. TR-CIM-94-7*, 1994.

J. il Jeong, D. Kang, Y. M. Cho, and J. Kim. Kinematic calibration for redundantly actuated parallel mechanisms. *Journal of Mechanical Design*, 126(2):307–318, 2004.

C. Innocenti. Forward kinematics in polynomial form of the general Stewart platform. *J. Mech. Des.*, 123(2):254–260, 2001.

D. Kanaan, P. Wenger, S. Caro, and D. Chablat. Singularity analysis of lower mobility parallel manipulators using Grassmann–Cayley algebra. *IEEE Transactions on Robotics*, 25(5):995–1004, 2009.

X. Kong and C. M. Gosselin. Uncertainty singularity analysis of parallel manipulators based on the instability analysis of structures. *The International Journal of Robotics Research*, 20 (11):847–856, 2001.

X. Kong and C. M. Gosselin. Kinematics and singularity analysis of a novel type of 3-CRR 3-DOF translational parallel manipulator. *The International Journal of Robotics Research*, 21(9):791–798, 2002.

X. Kong and C. M. Gosselin. Type synthesis of 3T1R 4-DOF parallel manipulators based on screw theory. *IEEE Transactions on Robotics and Automation*, 20(2):181–190, 2004a.

X. Kong and C. M. Gosselin. Type synthesis of 3-DOF translational parallel manipulators based on screw theory. *ASME Journal of Mechanical Design*, 126(1):83–92, 2004b.

X. Kong and C. M. Gosselin. Type synthesis of 3-DOF spherical parallel manipulators based on screw theory. *ASME Journal of Mechanical Design*, 126(1):101–108, 2004c.

X. Kong and C. M. Gosselin. Type synthesis of three-degree-of-freedom spherical parallel manipulators. *The International Journal of Robotics Research*, 23(3):237–245, 2004d.

X. Kong and C. M. Gosselin. *Type synthesis of parallel mechanisms*, volume 33. Springer Tracts in Advanced Robotics, 2007.

X. Kong, C. M. Gosselin, and P.-L. Richard. Type synthesis of parallel mechanisms with multiple operation modes. *ASME Journal of Mechanical Design*, 129(6):595–601, 2006.

X. Kong, D. Chablat, S. Caro, J. Yu, and C. Gosselin. Type synthesis of kinematically redundant 3T1R parallel manipulators. In *International Design Engineering Technical Conferences and Computers and Information in Engineering Conference*, volume 55935, page V06AT07A047. American Society of Mechanical Engineers, 2013.

J. Kotlarski, B. Heimann, and T. Ortmaier. Experimental validation of the influence of kinematic redundancy on the pose accuracy of parallel kinematic machines. In *Robotics and Automation (ICRA), 2011 IEEE International Conference on*, pages 1923–1929. IEEE, 2011.

G. A. Kragten, M. Baril, C. Gosselin, and J. L. Herder. Stable precision grasps by underactuated grippers. *IEEE Transactions on Robotics*, 27(6):1056–1066, 2011.

T. Laliberté, C. M. Gosselin, and M. Jean. Static balancing of 3-DOF planar parallel mechanisms. *IEEE/ASME Transactions on Mechatronics*, 4(4):363–377, 1999.

D. Lazard. On the representation of rigid-body motions and its application to generalized platform manipulators. In *Computational kinematics*, pages 175–181. Springer, 1993.

T.-Y. Lee and J.-K. Shim. Forward kinematics of the general 6–6 Stewart platform using algebraic elimination. *Mechanism and Machine Theory*, 36(9):1073–1085, 2001.

F. Lévesque, B. Sauvet, P. Cardou, and C. Gosselin. A model-based scooping grasp for the autonomous picking of unknown objects with a two-fingered gripper. *Robotics and Autonomous Systems*, 106:14–25, 2018.

C. Loughlin, A. Albu-Schäffer, S. Haddadin, C. Ott, A. Stemmer, T. Wimböck, and G. Hirzinger. The DLR lightweight robot: design and control concepts for robots in human environments. *Industrial Robot: an international journal*, 2007.

M. Luces, J. K. Mills, and B. Benhabib. A review of redundant parallel kinematic mechanisms. *Journal of Intelligent & Robotic Systems*, 86(2):175–198, 2017.

F. Marquet, O. Company, S. Krut, and F. Pierrot. Enhancing parallel robots accuracy with redundant sensors. In *Robotics and Automation, 2002. Proceedings. ICRA'02. IEEE International Conference on*, volume 4, pages 4114–4119. IEEE, 2002.

B. Massa, S. Roccella, M. C. Carrozza, and P. Dario. Design and development of an underactuated prosthetic hand. In *Proceedings 2002 IEEE International Conference on Robotics and Automation (Cat. No. 02CH37292)*, volume 4, pages 3374–3379. IEEE, 2002.

J.-P. Merlet. Singular configurations of parallel manipulators and Grassmann geometry. *The International Journal of Robotics Research*, 8(5):45–56, 1989.

J.-P. Merlet. Solving the forward kinematics of a Gough-type parallel manipulator with interval analysis. *The International Journal of robotics research*, 23(3):221–235, 2004.

J.-P. Merlet. Jacobian, manipulability, condition number, and accuracy of parallel robots. *ASME Journal of Mechanical Design*, 128(1):199–206, 2006a.

J.-P. Merlet. *Parallel robots*, volume 128. Springer Science & Business Media, 2006b.

B. Monsarrat and C. M. Gosselin. Singularity analysis of a three-leg six-degree-of-freedom parallel platform mechanism based on Grassmann line geometry. *The International Journal of Robotics Research*, 20(4):312–328, April 2001.

B. Monsarrat and C. M. Gosselin. Workspace analysis and optimal design of a 3-leg 6-DOF parallel platform mechanism. *IEEE Transactions on Robotics and Automation*, 19(6):954–966, December 2003.

V. Parenti-Castelli and R. Di Gregorio. Determination of the actual configuration of the general Stewart platform using only one additional sensor. 1999.

F. Pierrot. Parallel Mechanism and Redundancy. In *1st International Colloquium of the Collaborative Research Centre 562 – "Robotic Systems for Handling and Assembly"*, pages 261–277, France, May 2002.

M. Raghavan. The Stewart platform of general geometry has 40 configurations. 1993.

C. Reboulet. Hybrid control of a manipulator with an active compliant wrist. *3rd Int. Sympo. Robotics Research*, pages 237–241, 1985.

J. M. Romano, K. Hsiao, G. Niemeyer, S. Chitta, and K. J. Kuchenbecker. Human-inspired robotic grasp control with tactile sensing. *IEEE Transactions on Robotics*, 27(6):1067–1079, 2011.

B. Rooks. The harmonious robot. *Industrial Robot: An International Journal*, 33(2):125–130, 2006.

H. Saafi, M. A. Laribi, and S. Zeghloul. Redundantly actuated 3-RRR spherical parallel manipulator used as a haptic device: improving dexterity and eliminating singularity. *Robotica*, 33(5):1113–1130, 2015.

L.-T. Schreiber and C. Gosselin. Passively driven redundant spherical joint with very large range of motion. *Journal of Mechanisms and Robotics*, 9(3):031014, 2017.

L.-T. Schreiber and C. Gosselin. Kinematically redundant planar parallel mechanisms: Kinematics, workspace and trajectory planning. *Mechanism and Machine Theory*, 119:91–105, 2018.

L.-T. Schreiber and C. Gosselin. Exploiting the kinematic redundancy of a (6+3) degrees-of-freedom parallel mechanism. *Journal of Mechanisms and Robotics*, 11(2), 2019.

B. Siciliano. Kinematic control of redundant robot manipulators: A tutorial. *Journal of Intelligent and Robotic Systems*, 3(3):201–212, 1990.

B. M. St-Onge and C. M. Gosselin. Singularity analysis and representation of the general Gough-Stewart platform. *The International Journal of Robotics Research*, 19(3):271–288, 2000.

G. Strang. *Introduction to Linear Algebra*. Wellesley-Cambridge Press, Wellesley, MA, fourth edition, 2009.

M. Tale Masouleh and C. m. Gosselin. Singularity analysis of 5-RP RRR parallel mechanisms via Grassmann line geometry. In *International Design Engineering Technical Conferences and Computers and Information in Engineering Conference*, volume 49040, pages 969–978, 2009.

L. Tancredi, M. Teillaud, and J. Merlet. Forward kinematics of a parallel manipulator with additional rotary sensors measuring the position of platform joints. In *Computational Kinematics' 95*, pages 261–270. Springer, 1995.

A. Tobergte, P. Helmer, U. Hagn, P. Rouiller, S. Thielmann, S. Grange, A. Albu-Schäffer, F. Conti, and G. Hirzinger. The sigma. 7 haptic interface for mirosurge: A new bi-manual surgical console. In *2011 IEEE/RSJ International Conference on Intelligent Robots and Systems*, pages 3023–3030. IEEE, 2011.

C. W. Wampler. Forward displacement analysis of general six-in-parallel SPS (Stewart) platform manipulators using soma coordinates. *Mechanism and Machine Theory*, 31(3):331–337, 1996.

J. Wang and C. m. M. Gosselin. Kinematic analysis and design of kinematically redundant parallel mechanisms. *ASME Journal of Mechanical Design*, 126(1):109–118, 2004.

K. Wen and C. Gosselin. Kinematically redundant hybrid robots with simple singularity conditions and analytical inverse kinematic solutions. *IEEE Robotics and Automation Letters*, 4(4):3828–3835, 2019.

K. Wen, T. Seo, and J. W. Lee. A geometric approach for singularity analysis of 3-DOF planar parallel manipulators using Grassmann–Cayley algebra. *Robotica*, 35(3):511–520, 2017.

K. Wen, D. Harton, T. Laliberté, and C. Gosselin. Kinematically redundant (6+3)-dof hybrid parallel robot with large orientational workspace and remotely operated gripper. In *IEEE International Conference on Robotics and Automation (ICRA)*, pages 1672–1678, 2019.

K. Wen, T. S. Nguyen, D. Harton, T. Laliberté, and C. Gosselin. A backdrivable kinematically redundant (6+3)-dof hybrid parallel robot for intuitive sensorless physical human-robot interaction. *IEEE Transactions on Robotics*, 2020. Accepted.

J. Yu, X. Dong, X. Pei, and X. Kong. Mobility and singularity analysis of a class of two degrees of freedom rotational parallel mechanisms using a visual graphic approach. *ASME Journal of Mechanisms and Robotics*, 4(4), 2012.

T. S. Zhao, J. S. Dai, and Z. Huang. Geometric analysis of overconstrained parallel manipulators with three and four degrees of freedom. *JSME International Journal Series C Mechanical Systems, Machine Elements and Manufacturing*, 45(3):730–740, 2002.

Y. Zhao and F. Gao. Dynamic performance comparison of the 8-PSS redundant parallel manipulator and its non-redundant counterpart—the 6-PSS parallel manipulator. *Mechanism and Machine Theory*, 44(5):991–1008, 2009.

D. Zlatanov, R. Fenton, and B. Benhabib. A unifying framework for classification and interpretation of mechanism singularities. *ASME Journal of Mechanical Design*, 117(4):566–572, 1995.

D. Zlatanov, I. A. Bonev, and C. M. Gosselin. Constraint singularities of parallel mechanisms. In *Robotics and Automation, 2002. Proceedings. ICRA'02. IEEE International Conference on*, volume 1, pages 496–502. IEEE, 2002.